IntechOpen

Neutron Scattering

Edited by Waldemar Alfredo Monteiro

NEUTRON SCATTERING

Edited by **Waldemar Alfredo Monteiro**

Neutron Scattering
http://dx.doi.org/10.5772/60694
Edited by Waldemar Alfredo Monteiro

Contributors

Alessandro Cunsolo, bao yang, Jiajun Xu, Paulo De Tarso Freire, José Pereira, Heloisa Bordallo, Cristian Angelo Dragolici, Hsin-Hui Shen, Chun In Yeung, Tsung-Wu Lin, Xiaowei Zhang, Nian Ji, Valeria Lauter, Hailemariam Ambaye, Jian-Ping Wang

Notice

Statements and opinions expressed in the chapters are these of the individual contributors and not necessarily those of the editors or publisher. No responsibility is accepted for the accuracy of information contained in the published chapters. The publisher assumes no responsibility for any damage or injury to persons or property arising out of the use of any materials, instructions, methods or ideas contained in the book.

We are IntechOpen,
the world's leading publisher of
Open Access books
Built by scientists, for scientists

3,800+
Open access books available

116,000+
International authors and editors

120M+
Downloads

151
Countries delivered to

Our authors are among the
Top 1%
most cited scientists

12.2%
Contributors from top 500 universities

Selection of our books indexed in the Book Citation Index
in Web of Science™ Core Collection (BKCI)

Interested in publishing with us?
Contact book.department@intechopen.com

Numbers displayed above are based on latest data collected.
For more information visit www.intechopen.com

Meet the editor

Waldemar Alfredo Monterio, MSc (Solid State Physics), DSc (Nuclear Technology), is a physicist, at the University of São Paulo, São Paulo, Brazil. His expertise areas are Physical Metallurgy, Powder Metallurgy, and Materials Characterization (Optical and Electron Microscopy; Microanalysis Techniques). He is senior researcher in metallic materials at the Nuclear and Energetic Researches Institute, São Paulo, Brazil. He is professor (graduate course) on Materials Characterization (Electron Microscopy Techniques and Microanalysis) and researcher and lecturer (undergraduate and graduate courses) at the Presbyterian Mackenzie University, São Paulo, Brazil. He has published almost 3 books, 5 book chapters, and 156 articles (scientific journal or congress proceedings). His academic advisories include 45 scientific initiation (undergraduate students), 27 MSc, and 15 DSc students.

Contents

Preface

This book brings suitable data concerning theory and experiments of neutron interactions with different materials. Since the neutron discovery by Chadwick in 1932 (Proc Roy Soc A136 692), researchers of the entire world begin to make studies about it. It is well-known that neutron have no charge, and their electric dipole moment is either zero or too small to measure, but theories show that neutron has spin (presence of magnetic moment), and polarization neutron scattering is plausible.

It is known that neutron scattering is a "non-destructive microscope" for seeing inside matter. The theories and experiments show us that solid matter is not very dense since the size of a scattering center (i.e., a nucleus) is typically 100,000 times smaller than the distance between centers.

Furthermore, neutrons interact with atoms via nuclear rather than electrical forces, and nuclear forces are very short range — on the order of scarce femtometers. As a consequence, neutrons can move large distances through most materials without being scattered or absorbed. For these reasons, neutron can penetrate matter far better than charged particles even if it first has to pass through a container, such as would be required for a liquid or powder sample, for example, or if the sample had to be maintained at low temperature or high pressure.

In this book, it is acquired information concerning inelastic scattering cross-sections for neutron; polarized neutron reflectivity; scattering methods; neutron reflectometry tool to probe the chemical structures; neutron scattering for amino acid crystals; and small-angle neutron scattering nanoemulsion heat transfer fluids.

Prof. Dr. Waldemar Alfredo Monteiro
Materials Science and Technology Center
Nuclear and Energetic Researches Institute
University of São Paulo

Engineering School
Presbyterian Mackenzie University
São Paulo, SP
Brazil

Using X-ray as a Probe of the Terahertz Dynamics of Disordered Systems – Complementarity with Inelastic Neutron Scattering and Future Perspectives

Alessandro Cunsolo

Additional information is available at the end of the chapter

http://dx.doi.org/10.5772/62844

Abstract

This Chapter is devoted to a general introduction of the high resolution (meV) inelastic x-ray scattering (IXS) technique. This starts from a theoretical derivation of the IXS cross section and the demostration of its link with the spectrum of density fluctuations. The complementarity of this technique with the other mesocopic spectrocopy method, inelastic neutron scattering (INS) is discussed in detail by emphasizing differences and similarities both from the practical and the teorethical points of view. Along with this general discussion, examples are given of both an existing IXS spectrometer and a new-concept one to be soon in operation. Finally, the result of a recent joint INS and IXS experiment on water, taking advantage of the complementarity of these two techniques, are described in the last paragraphs.

Keywords: Inelastic neutron and X-ray scattering, dynamics of disorder materials, THz spectrocopy

1. Introduction

The study of the collective dynamics of disordered systems has been a vibrant field of research since the dawn of modern science, and yet, despite an intensive theoretical, experimental, and computational scrutiny, it still presents many unsettled aspects. The main reasons are the lack of a translational invariance in the microscopic structure of these systems and the often exceptionally complex movements of their microscopic constituents.

For instance, the interplay between collective modes and inter- and intramolecular degrees of freedom, as rotations, internal vibrations, or structural relaxation processes, is a fundamental property of the fluid, which still eludes a comprehensive understanding.

The spectrum of the density fluctuations, $S(Q,\omega)$, is a well-suited variable to test various theoretical models of the liquids' dynamics because it can be directly accessed by both conventional spectroscopic methods and molecular dynamics (MD) computer simulations.

Although the shape of $S(Q,\omega)$ is reasonably understood at macroscopic or quasi-macroscopic scales, over which the fluid appears as a continuum, its evolution beyond the continuous limit still represents a theoretical challenge. In particular, this applies to the so-called "mesoscopic" regime, corresponding to distances and timescales matching with first neighboring molecules' separations and cage oscillation periods, respectively.

From the experimental side, the study of $S(Q,\omega)$ in liquids at mesoscopic scales has been an exclusive duty of inelastic neutron scattering (INS) until almost the end of the last millennium. Nowadays, INS is a rather mature technique, which first saw the light in the mid-1950s [1]. Conversely, the other mesoscopic inelastic spectroscopy, inelastic X-ray scattering (IXS), is relatively young, having been developed only a couple of decades ago, thanks to the advent of synchrotron sources with unprecedented brilliance and parallel advances in crystal optic fabrication. This time lag mainly owes to the exceptionally small energy resolution, $\Delta E/E$, required by IXS studies of the mesoscopic [nm, millielectron volt (meV)] dynamics of fluids. Specifically, being current IXS spectrometers operated at incident energies larger than ≈ 20 keV, their ability to resolve meV energies imposes a relative energy resolution, $\Delta E/E$, at least as small as 10^{-7}.

Conversely, neutrons at low-to-moderate temperatures have 1 to 10 meV energies; therefore, even moderate $\Delta E/E$ values ($10^{-2} - 10^{-1}$) are sufficient to resolve meV collective excitations in the $S(Q,\omega)$ of liquids.

Furthermore, the IX Sintensity of materials with atomic number $Z < 4$ is dominated by photoelectric absorption, which makes this technique rather inefficient when dealing with systems with high Z.

Finally, the rapid decay of the IXS cross-section upon increasing the exchanged wave vector (Q) imposes severe intensity penalties even at intermediate Q values.

Nonetheless, the superior photon fluxes delivered by new-generation undulator sources, coupled with substantial advances in the design/fabrication of IXS spectrometers' optics, can nowadays overcompensate for the mentioned intensity limitations. Consequently, the statistical accuracy currently achieved in routine IXS measurements is unmatched by other complementary terahertz (THz) methods.

A general discussion of theoretical and practical aspects of IXS technique and in particular its applications to the study of the THz dynamics of liquids is the main purpose of this chapter, the rest of which is organized as follows. Section 2 describes brief derivation of the IXS cross-section. Section 3 discusses complementary aspects of IXS and INS methods. Section 4 proposes an example of current and future IXS spectrometers to illustrate how the latter hold the promise of a superior energy resolution. Finally, Section 5 concludes this chapter with an example of a joint INS and IXS experiment taking advantage of the complementarity of the two techniques.

2. The theory of IXS spectroscopy

Spectroscopy experiments are among the most powerful tools to investigate the properties of matter and have a very straightforward working principle, schematically outlined below.

A beam of particles–waves (e.g. neutron or X-rays) having narrow energy spread and angular divergence and a well-defined polarization impinges on a sample and is scattered in all directions.

A detector is used to count the particles deviated by an angle 2θ within a small solid angle $d\Omega$. Before the whole flight to the detector is accomplished, the particles may pass through some elements filtering their energy (monochromators and analyzers), angular divergence (collimators), and, in some cases, polarization (polarizers).

The whole instrument used to perform a scattering measurement is referred to as spectrometer, and its degree of complexity strongly depends, of course, on the physical problem the instrument is meant to investigate and the related requirement in collimation/monochromatization. Indeed, some optical elements cannot be included in the layout as irrelevant to the purpose of the measurement; for instance, when probing static, or structural, properties of the sample, as in diffraction experiments, there is no energy filter for the scattered beam (energy analyzer) because energy-integrated intensity is to be measured.

Regardless on the complexity of the specific experiment, the ultimate aim is to investigate the properties of the target sample through the counting of the probe particles having experienced an interaction with it through the scattering event. By virtue of this interaction event, the energy of the probe's particles may either be exchanged or remain constant, which, respectively, corresponds to the case of elastic or inelastic scattering measurements. Here the main focus is on the latter class of experiments and, in particular, on those involving X-rays as a probe and liquids as samples.

In general, it can be safely assumed that the interaction time between probe and target system is much shorter than any other timescale relevant to the experiment. In other terms, the scattering event can be schematized as an instantaneous collision between the X-ray beam and the scatterers, for example, electrons belonging to atoms or molecules of the sample.

If the scatterer is assumed fixed at the origin, infinitely massive, and at rest, the scattered electrical field at a distance $r = |\vec{r}|$ from the origin can be derived as the solution of the inhomogeneous Helmholtz equation [2]:

$$\left(\nabla^2 + k^2\right)\psi\left(\vec{r}\right) = -\delta\left(\vec{r}\right), \tag{1}$$

where " ∇^2 " is the Laplacian operator, whereas k is the wave number of the incident electromagnetic wave. At large distances from the origin, the outgoing wave is the sum of a plane

(transmitted) and a spherical wave. At finite scattering angles, the state of the scattered photons can be described by a spherical wave:

$$\psi_{sc} \propto \frac{e^{ikr}}{r}. \tag{2}$$

In summary, one can see that by virtue of the scattering event, photons are partly removed from the plane wave and re-radiated in a spherical wave, which can be thought as a simple manifestation of the Huygens' principle [3]. The photon scattered at an angle 2θ within a solid angle $d\Omega$ passes though the energy filter (analyzer) and is ultimately counted by the detector after impinging on its sensitive area $dA = r^2 d\Omega$, which is here intended to be small enough to safely approximate the scattered wave impinging on it as a plane wave (see Figure 1). The intensity scattered within a solid angle $d\Omega$ and an energy spread dE_F has the following general form:

$$I = K I_0 \frac{\partial^2 \sigma}{\partial \Omega\, \partial E_F} d\Omega\, dE_F, \tag{3}$$

where I_0 is the intensity of the beam impinging on the sample and K is a coefficient taking into account detector efficiency, sample self-absorption, and all geometrical and/or spurious intensity effects. In the above formula, the double differential scattering cross-section was introduced:

$$\frac{\partial^2 \sigma}{\partial \Omega\, \partial E'} = \frac{\text{Rate of photons scattered into } d\Omega \text{ with final energy between } E' \text{ and } E' + dE'}{I_0 \partial \Omega\, \partial E'}. \tag{4}$$

To derive an explicit expression for the double the variable above, it is useful to start from the Hamiltonian describing the interaction between the electrons of the target system and the time dependent electromagnetic field impinging on them. In the non-relativistic case, such an Hamiltonian reads as follows [4]:

$$H = \frac{1}{2m_e} \sum_i \left[\vec{P}_i - \frac{e}{c} \vec{A}(r_i)\delta(\vec{r} - \vec{r}_i) \right] \cdot \left[\vec{P}_i - \frac{e}{c} \vec{A}(r_i)\delta(\vec{r} - \vec{r}_i) \right] + \sum_i V(r_i) + V_{\text{int}}^{\text{e-e}}, \tag{5}$$

where $\vec{P}_i$ and $\vec{r}_i$ represent the momentum and the position of the ith electron, respectively; c, e, and m_e are the speed of light in vacuum, the electron charge, and mass, respectively; $\vec{A}(\vec{r})$ is the vector potential at the position $\vec{r}$ and finally, $V_{\text{int}}^{\text{e-e}}$ is the electron–electron interaction integrated over the electron clouds of target atoms.
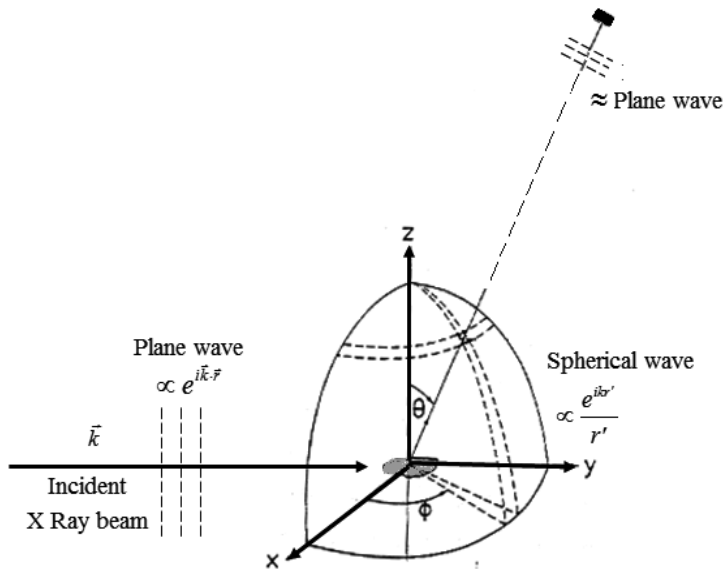
Figure 1. Schematic representation of the scattering geometry.

In Eq. 5, all the spin-dependent contributions are omitted because, in general, those couple very weakly with the incident electromagnetic field. The Hamiltonian in Eq. 5 can be cast as follows:

$$H = H_{el} + H_{int}^{(1)} + H_{int}^{(2)},$$

where

$$H_{el} = \sum_i \left[\frac{P_i^2}{2M} + V(r_i) \right] \qquad (a)$$

$$H_{int}^1 = -\frac{e}{2mc} \sum_i \left[\vec{P}_i \cdot \vec{A}(\vec{r}) \delta(\vec{r} - \vec{r}_i) + \vec{A}\delta(\vec{r} - \vec{r}_i) \cdot \vec{P}_i \right] \qquad (b)$$

$$H_{int}^2 = \frac{e^2}{2mc^2} \sum_i \delta(\vec{r} - \vec{r}_i) \vec{A}(\vec{r}) \cdot \vec{A}(\vec{r}) \qquad (c)$$

(6)

On a general ground, the parts containing the square of the perturbing term, i.e. the vector potential, contribute to two-photon processes such as the scattering event. The two terms entering in H_{int}^1 (Eq. 6b), both being linear in $\vec{A}(\vec{r})$, describe to the leading order one-photon processes, such as absorption and emission, while they account for the scattering process to the second order only. Conversely, the so-called Thomson term, i.e. the term H_{int}^2 in Eq. 6c, being quadratic in the vector potential, accounts to the first order for a two-photon process, such as the scattering event. It can be shown that, away from an energy resonance, the Thomson term dominates over the second-order expansion of Eq. 6b, thus providing the leading

contribution to the scattering process. In the following, an explicit derivation of the double differential IXS cross section is carried out within the assumption that the Thomson term entirely describes the scattering process and further assuming that:

- The center of mass of the electronic cloud follows the nuclear motion as a slow drift, i.e. with no delay (adiabatic approximation). This justifies the expression of the initial and final states of scatterer as the product of two terms containing either only electronic or only nuclear coordinates. This approximation becomes particularly accurate at energies smaller than excitation energies of electrons in bound core states, i.e. for nearly all cases of practical interest for high resolution IXS measurements. In liquid metals, this approximation only excludes electron densities near the Fermi level.

- The electronic part of the total wave function is unaffected by the scattering process, thus the difference between the initial (before scattering) state and the final (after scattering) state is due only to excitations associated with atomic density fluctuations.

The following derivation can be found in various textbooks and is also clearly illustrated in a theoretical work by Sinha [4], whose main results are discussed here.

In principle, one could use the perturbation theory to derive the rate of scattering events associated to an incident plane wave having wave vector $\vec{k}_I$ and to all plane waves having wave vector $\vec{k}_F$, pointing to a given direction 2θ within the solid angle $d\Omega$ intercepted by the detector. However, the normalization of the scattered wave would require its amplitude to decrease at least as r^{-1} at large distances r from the scattering event, and this hardly fits the case of a plane wave. To circumvent this problem, it is useful to define the scattering process within a box of size L with periodic boundary conditions and eventually consider the limit of large L. This expedient enables to easily count the states and properly normalize the wave functions.

Within such a box, the vector potential can be expressed as a linear combination of normalized plane waves of the form $1/L^{3/2}\exp(i\vec{k} \cdot \vec{r})$. Namely:

$$\vec{A}(\vec{r}) = \sum_{k,\varepsilon} \sqrt{\left(\frac{\hbar}{\omega_k L^3}\right)} c\hat{\varepsilon} \left[\vec{a}_{k,\varepsilon}^+ \exp\left(i\vec{k} \cdot \vec{r}\right) + \vec{a}_{k,\varepsilon}^- \exp\left(-i\vec{k} \cdot \vec{r}\right) \right], \tag{7}$$

where the exponential with either the sign "+" or "−" describes downstream and upstream propagating plane waves, respectively. Here $\eta = h/2\pi$, where h is the Planck constant, while the indexes k and ε label, respectively, the wave vector and the polarization states of the wave, as identified by the unit vector $\hat{\varepsilon}$ and the vector $\vec{k}$, respectively. The coefficients $\vec{a}_{k,\varepsilon}^+$ and $\vec{a}_{k,\varepsilon}^-$ in Eq. 7 represent, respectively, the annihilation and the creation operators for the initial photon state $|k, \varepsilon\rangle$, while ω_k is the angular frequency.

The scattering process can be depicted as a simultaneous transition between the $|k_I, \varepsilon_I\rangle$ and $|k_F, \varepsilon_F\rangle$ photon states and between the $|\lambda_I\rangle$ and $|\lambda_F\rangle$ sample states. The rate of such a transition is predicted by Fermi's golden rule [5]:

$$\sum_{k_F}^{\mathrm{d}\Omega} W_{|I\rangle \to |F\rangle} = \frac{2\pi}{\hbar} v_{k_F, \varepsilon_F} \left| \langle F | H_{\mathrm{int}}^{(2)} | I \rangle \right|^2 , \tag{8}$$

where, to ease the notation, it is assumed $|I\rangle = |k_I, \varepsilon_I, \lambda_I\rangle$, $|F\rangle = |k_F, \varepsilon_F, \lambda_F\rangle$. The parameters v_{k_F, ε_F} represent the density of final photon states and can be derived by evaluating the density of k_F points in the reciprocal space. For this purpose, one can consider all plane waves having energies included in between E_F and $E_F + \mathrm{d}E_F$ and pointing toward a direction 2θ within the solid angle $\mathrm{d}\Omega$, the number of such plane waves being $v_{k_F, \varepsilon_F} \mathrm{d}E_F$. In the reciprocal space, the energy spread $\mathrm{d}E_F$ corresponds to the volume $\mathrm{d}V(k_F)$ of the spherical shell (see Figure 2), which is identified by vectors $\vec{k}_F$ having amplitude included in between k_F and $k_F + \mathrm{d}k_F$ and direction included within a solid angle $\mathrm{d}\Omega$. This elemental volume reads as follows:

$$\mathrm{d}V(k_F) = \mathrm{d}\Omega\, k_F^2 \mathrm{d}k_F.$$

The k_F values included within the box defined above are given by $2\pi / L(n_x, n_y, n_z)$, with $n_{s=x,y,z}$ generic integers. This defines a lattice in the k space whose points can be associated with a unit cell of volume $V_{\min} = (2\pi / L)^3$. Assuming a small cell (a large size box L), the total number of lattice points inside the elemental volume $\mathrm{d}V(k_F)$ is given by the ratio between such a volume and $V_{\min}$, and this must be equal to the number of plane waves defined above, that is:

$$v_{k_F, \varepsilon_F} \mathrm{d}E_F = \mathrm{d}\Omega\, k_F^2 \left(\frac{L}{2\pi} \right)^3 \mathrm{d}k_F . \tag{9}$$
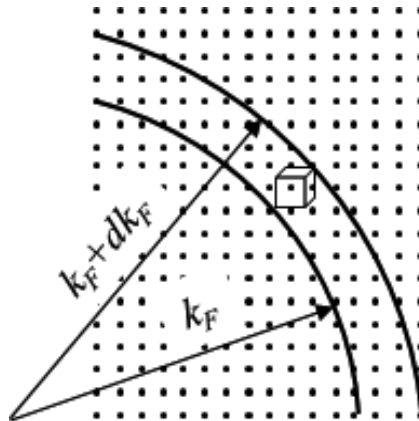
Figure 2. Schematic representation of the elemental volumes in the reciprocal space. The cube enclosing a lattice point represents the unit cell of volume $V_{\min} = (2\pi / L)^3$.

$$\nu_{k_F,\varepsilon_F}\, dE_F = d\Omega\, k_F^2 \left(\frac{L}{2\pi}\right)^3 dk_F \; . \tag{10}$$

Furthermore, being $E_F = \hbar c k_F$, or, equivalently, $dE_F = \hbar c\, dk_F$, one has:

$$\nu_{k_F,\varepsilon_F}\, dE_F = \frac{k_F^2 L^3}{(2\pi)^3 \hbar c}\, d\Omega \; . \tag{11}$$

Also, the incident photon flux, i.e. the number of photons passing through a unit surface in the unit time, is given by:

$$\varphi = \frac{c}{V} \; . \tag{12}$$

Furthermore, the double differential cross section for the scattering process can be related to such a flux through:

$$\left(\frac{d\sigma}{d\Omega dE_F}\right)_{|I\rangle \to |F\rangle} = \frac{1}{\varphi}\frac{1}{d\Omega}\sum_{k_F}^{d\Omega} W_{\lambda_I \to \lambda_F}. \tag{13}$$

Using Eqs. 8–12, the matrix element defining Fermi's golden rule (Eq. 8) can be thus expressed as:

$$\left\langle F\left|H_{int}^{(2)}\right|I\right\rangle = \frac{1}{L^3}\frac{e^2}{mc^2}\frac{\hbar c}{\left[\omega(k_I)\omega(k_I)\right]^{1/2}}(\hat{\varepsilon}_I \cdot \hat{\varepsilon}_F)\left\langle \lambda_F\left|\sum_j \exp\left(-i(\vec{Q}\cdot\vec{r}_j)\right|\lambda_I\right\rangle\delta\left(\hbar\omega - E_I - E_F\right) , \tag{14}$$

Here the conservation laws of momentum and energy in the scattering event have been superimposed by assuming $\hbar\vec{Q} = \hbar(\vec{k}_F - \vec{k}_I)$ and $\hbar\omega = E_F - E_I$, with $\hbar\vec{Q}$ and $\hbar\omega$ being the momentum and energy transferred from the photon to the target sample. In particular, the energy conservation is accounted by the $\delta(\hbar\omega - E_I - E_F)$ term in Eq. 13. Considering that the frequency of the incident (scattered) wave is $\omega(k_I) = ck_I$ ($\omega(k_F) = ck_F$), the double differential cross-section reduces to:

$$\left(\frac{d^2\sigma}{d\Omega dE'}\right)_{|I\rangle \to |F\rangle} = \frac{e^2}{mc^2}\left(\frac{k'}{k}\right)(\hat{\varepsilon}_I \cdot \hat{\varepsilon}_F)\times$$
$$\times\sum_{mj}\left[\left\langle \lambda_I\left|\exp\left(-i\vec{Q}\cdot\vec{r}_m\right)\right|\lambda_F\right\rangle\left\langle \lambda_F\left|\exp\left(i\vec{Q}\cdot\vec{r}_j\right)\right|\lambda_I\right\rangle\right]\delta\left(\hbar\omega + E_I - E_F\right) . \tag{15}$$

It has to be noticed that the sum involves states of the target system only. Here the indexes "*m*" and "*j*" label the coordinates of the scatterers, i.e. the electrons interacting with the electromagnetic field.

In a scattering experiment, the states of the target system $|\lambda_I\rangle$ and $|\lambda_F\rangle$ are generally unknown, because only the final and initial states of the photons are measured. However, it is usually assumed that, before the scattering event, the sample is in its thermodynamic equilibrium and, therefore, a "thermal" average can be performed over its initial state. Furthermore, if the sample can be treated as a many-body classical system, the probability of the $|\lambda_I\rangle$ state is $p_I = \exp(-\beta E_I)\big/\sum_I \exp(-\beta E_I)$, where $\beta = 1/k_B T$ and k_B and T are the Boltzmann constant and the temperature of the sample, respectively. At this stage, the cross section associated to the transition between the photon states $|k_I,\ \varepsilon_I\rangle$ and $|k_F,\ \varepsilon_F\rangle$ can be written as:

$$
\left(\frac{d^2\sigma}{d\Omega dE_F}\right)_{|k_I,\varepsilon_I\rangle \to |k_F,\varepsilon_F\rangle} = \frac{e^2}{mc^2}\left(\frac{k_F}{k_I}\right)\left(\bar{\varepsilon}_I\cdot\hat{\varepsilon}_F\right)\times
$$
$$
\times \sum_{mj}\sum_{\lambda_I\lambda_F}\left[p_\lambda \left\langle \lambda_I \left| \exp\left(-i\vec{Q}\cdot\vec{r}_m\right)\right|\lambda_F\right\rangle \left\langle \lambda_F \left| \exp\left(i\vec{Q}\cdot\vec{r}_j\right)\right|\lambda_I\right\rangle\right] \delta\left(\hbar\omega + E_I - E_F\right).
$$
(16)

This formula can be further simplified by:

- assuming the completeness of the final eigenstates of the system $\sum_{\lambda_F}|\lambda_F\rangle\langle\lambda_F| = I$, with *I* being the identity operator,

- considering that

$$
\delta(\hbar\omega + E_I - E_F) = 1/2\pi\hbar\int_{-\infty}^{\infty}\exp(i\omega t)\exp(E_I - E_F)/\hbar,
$$

- using the Heisenberg representation of the time evolution of a generic operator $A(t) = \exp(iHt/\hbar)A(0)\exp(-iHt/\hbar)$, where *H* is the Hamiltonian of the unperturbed system, and finally

- considering that, since $|I\rangle$ and $|F\rangle$ eigenstates of the Hamiltonian, one has: $\exp(iE_I t/\hbar)|I\rangle = \exp(iHt/\hbar)|I\rangle$ and $\exp(iE_F t/\hbar)|I\rangle = \exp(iHt/\hbar)|F\rangle$.

With the above manipulations, the double differential cross section eventually reduces to:

$$
\left(\frac{d^2\sigma}{d\Omega dE'}\right)_{|k_I,\varepsilon_I\rangle \to |k_F,\varepsilon_F\rangle} = \frac{e^2}{mc^2}\left(\frac{k'}{k}\right)\left(\bar{\varepsilon}_I\cdot\hat{\varepsilon}_F\right)\times
$$
$$
\times\frac{1}{2\pi\hbar}\int_0^{\infty}\sum_{mj}\left\langle\exp\left\{-i\vec{Q}\cdot\left[\vec{r}_j(t) - \vec{r}_m(0)\right]\right\}\right\rangle\exp(i\omega t)dt,
$$
(17)

where the correlation function between two generic variables was introduced as:

$$\langle A\langle 0 \rangle B(t) \rangle = \sum_{\lambda} p_{\lambda} \langle \lambda \mid A\langle 0 \rangle B(t) \mid \lambda \rangle.\text{was introduced.}$$

2.1. Cross section and density correlation function

The double differential cross section can be now simply connected to the Fourier transform of the density–density correlation function, as discussed in [6].

To show this explicitly, it is useful to start from an appropriate definition of the atomic density in the mesoscopic regime probed by IXS. There, the density of a single atom can be approximated by Dirac's δ function of the space coordinate:

$$n_j\left(\vec{r},t\right) = \delta\left[\vec{r} - \vec{R}_j(t)\right]. \tag{18}$$

Clearly, this is a highly discontinuous function diverging at the center of mass position of the jth atom $\vec{R}_j(t)$ and vanishing elsewhere. The normalization condition $\int_V n_j(\vec{r},t)d\vec{r} = 1$ simply means that, if a sufficiently large volume is covered, the particle should be counted one time inside such a volume. A coarse estimate of the density variable is given by the mean value $\langle n_j(\vec{r},t) \rangle = 1 \left/ V \int_V n_j(\vec{r},t)d\vec{r} = 1 \right/ V$ obtained as a statistical average over a certain volume. The density function of a system of N atoms, the density function can be expressed as follows:

$$n(\vec{r},t) = \sum_{i=1}^{N} \delta\left[\vec{r} - \vec{R}_i(t)\right].$$

One can perform the average density by integrating over the volume, eventually obtaining $\langle n(\vec{r},t) \rangle = 1/V \int_V n(\vec{r},t)d\vec{r} = n$, where $n=N/V$ is the number density (number of atoms in the unit volume) of the system. However, in the present context is more useful to deal with the density fluctuation:

$$\delta n(\vec{r},t) = \sum_{i=1}^{N} \delta\left[\vec{r} - \vec{R}_i(t)\right] - n. \tag{19}$$

At this stage, the atomic Van Hove correlation function can be introduced as:

$$G(\vec{r},t) = \frac{1}{N} \sum_{k,j=1}^{N} \left\langle \delta\left[\vec{r} - \vec{R}_k(0)\right]\delta\left[\vec{r} - \vec{R}_j(t)\right] \right\rangle - n = \frac{1}{N} \sum_{k,j=1}^{N} \left\langle \delta\left[\vec{r} - \vec{R}_k(0) - \vec{R}_j(t)\right] \right\rangle - n. \tag{20}$$

Since a scattering experiment probes the reciprocal rather than the real space, it is here convenient to introduce the Fourier transform of the density in Eq. 18:

$$\delta n\left(\vec{Q},t\right) = \sum_j \exp\left[\vec{r} - \vec{R}_j(t)\right] - \left(2\pi\right)^3 n\delta\left(\vec{Q}\right).$$

(21)

and its time-correlation, the intermediate scattering function:

$$\tilde{F}(\vec{Q},t) = \langle \delta n^*(\vec{Q},0)\delta n(\vec{Q},t)\rangle = \frac{1}{N}\sum_{mj}\exp\left\langle i\vec{Q}\cdot\left[\vec{R}_j(t) - \vec{R}_m(0)\right]\right\rangle - \left(2\pi\right)^3 \delta\left(\vec{Q}\right).$$

(22)

Finally, the dynamic structure factor, which is the variable actually measured in a scattering experiment, reads as:

$$\tilde{S}(\vec{Q},\omega) = \frac{1}{2\pi\hbar}\int_{-\infty}^{+\infty} e^{i\omega t}\langle \delta n^*\left(\vec{Q},0\right)\delta n\left(\vec{Q},t\right)\rangle\ \mathrm{d}t =$$
$$\frac{1}{2\pi\hbar}\int_0^t\left[\sum_{mj}\exp\left\langle i\vec{Q}\cdot\left[\vec{R}_j(t) - \vec{R}_m(0)\right]\right\rangle - \left(2\pi\right)^3\delta\left(\vec{Q}\right)\right]\exp\left(i\omega t\right)\mathrm{d}t\ .$$

(23)

One can easily recognize that the second term under integration (having the sign "-" as a pre-factor) is proportional to $\delta(\omega)\delta(\vec{Q})$, thus is not relevant in a real IXS or INS experiment, as it describes the merely elastic (ω=0) scattering in the forward direction ($\vec{Q}$=0). Therefore, one can make the following identification:

$$\tilde{S}(\vec{Q},\omega) \rightarrow S(\vec{Q},\omega) = \frac{1}{2\pi\hbar}\int_0^t\left[\sum_{mj}\exp\left\langle i\vec{Q}\cdot\left[\vec{R}_j(t) - \vec{R}_m(0)\right]\right\rangle\right]\exp\left(i\omega t\right)\mathrm{d}t$$

It is important to recognize that Eqs. 17–23 depend on the center of mass (nuclear) coordinates of the atoms. The integral in Eq. 16 is thus to be identified with the spectrum of the density fluctuation autocorrelation function, provided the electronic coordinates $\vec{r}_j(t)$ are replaced by the nuclear ones $\vec{R}_j(t)$. This identification relies on the validity of the Born–Oppenheimer approximation, which ultimately justifies the factorization between exponential terms containing either merely electronic or merely nuclear coordinates. With such a factorization, the double differential cross section reduces to:

$$\left(\frac{\mathrm{d}^2\sigma}{\mathrm{d}\Omega\mathrm{d}E'}\right) = \frac{e^2}{mc^2}\left(\frac{k'}{k}\right)\left(\hat{\varepsilon}_\mathrm{I}\cdot\hat{\varepsilon}_\mathrm{F}\right)\left|f\left(Q\right)\right|^2 S\left(Q,\omega\right),$$

(24)

where

$$f(Q) = \sum_\alpha \exp(-i\vec{Q} \cdot \vec{\rho}_\alpha) \tag{25}$$

is the atomic structure factor, which depends on the coordinate $\vec{\rho}_\alpha$ of the αth electron in the reference frame with the nucleus at the origin. It is worth stressing that the sum in Eq. 25 runs over all electrons in the atom. Furthermore, in Eq. 24 it was assumed the isotropic character of a liquid system, which implies that physical properties do not depend on the direction of $\vec{Q}$ but only on its amplitude $Q = |\vec{Q}|$.

2.2. The incoherent contribution

The derivation discussed above strictly applies to systems of N identical atoms within the validity of the Born–Oppenheimer approximation. For a system containing different atoms, the derivation of the scattering cross section is only slightly more complex. However, a factorization between a merely electronic and a nuclear term is still possible and leads to the conclusion that the double differential cross section splits into two components: a coherent and an incoherent one. The former is proportional to the average value of the form factor, whereas the latter arises from its mean square fluctuations.

To illustrate this point, it is useful to start from the assumption that atoms in the target system have reasonably symmetric electronic clouds. The double differential cross section can thus be expressed as follows:

$$\left(\frac{\partial \sigma}{\partial \Omega dE'} \right) = r_0^2 \left(\frac{k'}{k} \right) (\hat{\varepsilon}_f \cdot \hat{\varepsilon}_i)^2 \frac{1}{N} \sum_{\alpha\beta} \sum_{mj} \left\langle \exp\left[iQ \cdot \left(\vec{R}_j(t) - \vec{R}_m(0) \right) \right] \right\rangle \overline{\exp\left[i\vec{Q} \cdot \left(\vec{\rho}_\alpha^n - \vec{\rho}_\beta^m \right) \right]}, \tag{26}$$

where the $\vec{\rho}_\alpha^i$ is the position the αth electron of the ith atom in the reference frame of atomic center of atomic mass. Here the bar on the top of the exponential term indicates an average over all atoms of the system. We can thus distinguish two cases in the following:

1. The term under average involves distinct atoms ($n \neq m$), then:

$$\sum_{\alpha,\beta} \overline{\exp\left(i\vec{Q} \cdot \vec{\rho}_\alpha^n \right) \exp\left(i\vec{Q} \cdot \vec{\rho}_\beta^m \right)} = \sum_\alpha \overline{\exp\left(i\vec{Q} \cdot \vec{\rho}_\alpha^n \right)} \sum_\beta \overline{\exp\left(i\vec{Q} \cdot \vec{\rho}_\beta^m \right)} = \overline{f(Q)}^2.$$

2. The term under average involves the same atom ($n = m$), then:

$$\sum_{\alpha,\beta} \overline{\exp\left(i\vec{Q} \cdot \vec{\rho}_\alpha^n \right) \exp\left(i\vec{Q} \cdot \vec{\rho}_\beta^m \right)} = \overline{f(Q)^2}.$$

Thus, in general:

$$\sum_{\alpha,\beta}\overline{\exp\left(i\vec{Q}\cdot\vec{\rho}_{\alpha}^{n}\right)\exp\left(i\vec{Q}\cdot\vec{\rho}_{\beta}^{m}\right)}=\overline{f(Q)}^{2}+\delta_{n,m}\left(\overline{f(Q)^{2}}-\overline{f(Q)}^{2}\right)=\overline{f(Q)}^{2}+\delta_{n,m}\overline{\left(f(Q)-\overline{f(Q)}\right)^{2}},$$

$$\overline{f(Q)}^{2}+\delta_{n,m}\left(\overline{f(Q)^{2}}-\overline{f(Q)}^{2}\right)=\overline{f(Q)}^{2}+\delta_{n,m}\overline{\left(f(Q)-\overline{f(Q)}\right)^{2}}$$

which eventually leads to the following expression for the IXS cross section:

$$\frac{\partial^{2}\sigma}{\partial\Omega\partial E_{F}}=r_{0}^{2}\left(\frac{k_{F}}{k_{I}}\right)\left(\hat{\varepsilon}_{I}\cdot\hat{\varepsilon}_{F}\right)\left\{\overline{f(Q)}^{2}S_{C}(Q,\omega)+\left[\overline{\left(f(Q)-\overline{f(Q)}\right)^{2}}\right]S_{I}(Q,\omega)\right\}. \tag{27}$$

The above formula shows that the scattering of the sample is composed of a coherent and an incoherent part, respectively, labeled by the "C" and "I" suffixes. While the latter results from the independent scattering of isolated atoms, the former also contains *the* interference between photon waves scattered by different atoms. Insight on the collective dynamics of atoms can only be sought for in the coherent scattering, whereas both coherent and incoherent scattering convey information on the single-atom dynamics.

2.3. The absorption coefficient

When actually performing the IXS measurement, it is important to optimize the sample thickness crossed by the beam (d) so as to maximize the scattering intensity. In fact, a simple d increase, albeit increasing the number of scatterers, does not necessarily enhance the scattered intensity because it also increases the sample (self) absorption. Therefore, the optimal choice of d is the result of a trade-off between competing scattering and absorption requirements. To handle the problem on a more quantitative basis, attenuation effects should be included in the general expression of the scattering intensity as prescribed by the following formula [7]:

$$I=I_{0}\frac{\partial^{2}\sigma}{\partial\Omega\ \partial E_{F}}\mathrm{d}\Omega\ \mathrm{d}E_{F}\ n\ d\ \exp\left(-\mu d\right), \tag{28}$$

where I_{0} is the number of incident photons per second and μ is the total absorption coefficient.

The intensity I in Eq. 27 reaches a maximum when $\partial I/\partial d=0$, i.e. for $d=1/\mu$ and, consequently, $I\propto 1/\mu$.

At the energies typical of IXS experiments, attenuation effects are dominated by the photo-electric absorption, for which $\mu\propto Z^{4}$. Consequently, for high-Z elements, μ is very large, and

therefore, the optimal sample thickness is small. Of course, the optimal d value strongly depends on the incident energy and on Z. This makes IXS, in principle, ideal to work with extremely small high Z samples, and it turns out to be a decisive advantage while dealing with samples only available in modest quantities and/or when extreme thermodynamic conditions need to be explored.

3. A closer comparison between IXS and INS techniques

In general, INS and IXS present several analogies:

1. They can be used to investigate bulk properties of materials, as opposite to more strongly interacting probes, such as electrons, which essentially convey insight on materials' surfaces.

2. They probe the dynamic response of density fluctuations through the Fourier transform of their autocorrelation function, i.e. the dynamic structure factor, $S(Q, \omega)$.

3. They are "mesoscopic" probes, i.e. they cover distances and timescales matching, respectively, first neighboring atoms' (molecules') separations and cage oscillation periods.

Other similarities emerge from the comparison of the IXS double differential cross section in Eq. 26 and its INS counterparts as derived, for instance, by [8]:

$$\frac{\mathrm{d}^2\sigma}{\mathrm{d}\Omega\mathrm{d}E_\mathrm{F}}\bigg|_\mathrm{INS} = \frac{k_\mathrm{F}}{k_\mathrm{I}}N\left[\overline{\left|\overline{b}\right|}^2 S_\mathrm{C}(Q,\omega) + \overline{\left|b-\left|b\right|\right|^2} S_\mathrm{I}(Q,\omega)\right]. \qquad (29)$$

It can be readily noticed that:

• For both X-ray and neutron scattering, the cross section depends on the ratio $k_\mathrm{F}/k_\mathrm{I}$. However, as discussed in the following, for IXS, this factor does not depend on frequency (energy) and can be safely approximated by 1.

• The role of the form factor $f(Q)$ in the IXS cross section mirrors the one of the scattering length b in the INS one. The main difference is their physical origin: $f(Q)$ relates to the photon–electron electromagnetic interaction, while b is connected to the neutron–nuclei interaction. As a consequence, $f(Q)$ depends on Z yet not on the atomic mass, i.e. it depends on the chemical rather than isotopic specie of the target sample. As discussed below, another fundamental difference is that $f(Q)$ sharply decreases at high exchanged momenta while b remains essentially constant.

Despite these formal similarities, the two techniques have several complementary aspects, as discussed below in some detail. This makes each of them better suited to some experiments

and less to other. A practical example of the coordinate use of these complementary methods is discussed at the end of this chapter.

3.1. Part A: advantages of IXS

3.1.1. Kinematic limitations

The conservation laws of momentum and energy lead to very different results when dealing with either neutron or X-ray probes. Let us consider the neutron case first. As mentioned, the momentum conservation law reads as:

$$\vec{Q} = \vec{k}_F - \vec{k}_I, \tag{30}$$

which can be rearranged as follows:

$$\left(\frac{Q}{k_I}\right)^2 = \left(\frac{k_F}{k_I}\right)^2 + 1 - 2\frac{k_F}{k_I}\cos 2\theta, \tag{31}$$

whereas the energy conservation law for the scattering event reads as:

$$E_F - E_I = \hbar\omega. \tag{32}$$

Considering that the kinetic energy of the freely flying neutron is:

$$E = \hbar^2 k^2 / 2m_n \tag{33}$$

with m_n being the neutron mass, Eq. 27 can be written as:

$$\left(\frac{k_F}{k_I}\right)^2 = \frac{\hbar\omega}{E_F} + 1. \tag{34}$$

By combining Eqs. 29 and 26 and taking the square root of both members, one eventually obtains:

$$\left(\frac{Q}{k_I}\right) = \sqrt{2 - \left(\frac{\hbar\omega}{E_I}\right) - 2\,\cos\left(2\theta\right)\sqrt{1 - \left(\frac{\hbar\omega}{E_I}\right)}}. \tag{35}$$

It is thus readily noticed that the dynamic domain (Q,ω) explored by an INS measurement is limited by the condition that both the arguments under the two square roots of Eq. 30 are positive. In particular, the argument of the "nested" square root, having pre-factor 2 cos(2θ), is positive whenever $E_I < \hbar\omega$. This reflects the obvious requirement that the energy transferred from the neutron to the sample cannot exceed the energy E_I initially carried by the neutron. Furthermore, the requirement for the argument of the larger square root in Eq. 26 to be positive introduces further restrictions to the explored dynamic range.

An example of these restrictions, customarily referred to as kinematic limitations, is provided by Figure 3, which refers to the specific case of INS experiments on water.

It is worth recalling that, since the pioneering MD work of [9] in the mid-1970s, it is well-known that the THz spectrum of water is dominated by two inelastic peaks, whose Q dispersions are reported in Figure 3 as computed by MD simulations [10]. However, the spectrum of water measured by two successive INS works (also reported in the plot) did not bear any evidence of a double peaked shape. The reason of the apparent discrepancy between computational and experimental results mainly owed to kinematic and resolution limitations affecting the latter. These limitations were substantially different in the two measurements, owing to the different incident energies: 36 meV and 80 meV respectively for [11] and [12]. In the former experiment [11] these limitations prevented the proper coverage of the high energy modes. Conversely, the higher incident energy (barely) permitted the second INS measurement [12] to cover the high energy mode, yet it entailed a coarsening of the energy resolution, which became too broad to properly resolve the low frequency mode. For reference, Figure 3 displays the portion of the dynamic plane covered by Bosi and coworkers' measurement (shadowed area) along with the boundary of the dynamic region explored by Teixeira and coworkers' one.

Briefly, Figure 3 exemplifies a situation in which the dynamic range covered by the experiment resembles a "blanket too short" preventing the simultaneous access to both high and low ω or Q values. A similar problem is commonly encountered in INS measurements,

The development of high energy resolution (meV) IXS in the mid-1990s offered the opportunity of performing THz spectroscopy measurements virtually free from kinematic limitations, apart from the obvious ones related to the finite energy and momentum resolutions.

Such a virtual absence of kinematic constraints follows from these two circumstances:

1. the energy–momentum relationship for photons is linear:

$$E_j = ck_j \tag{36}$$

instead of quadratic, as for INS (see Eq. 28) and

2. for IXS $\hbar\omega << E_I$ (typically $E_I \approx 20$ keV, while $|\hbar\omega| \leq \approx 80$ meV), or, equivalently $E_F = E_I$, which, through Eq. 31, implies $k_F = k_I$.
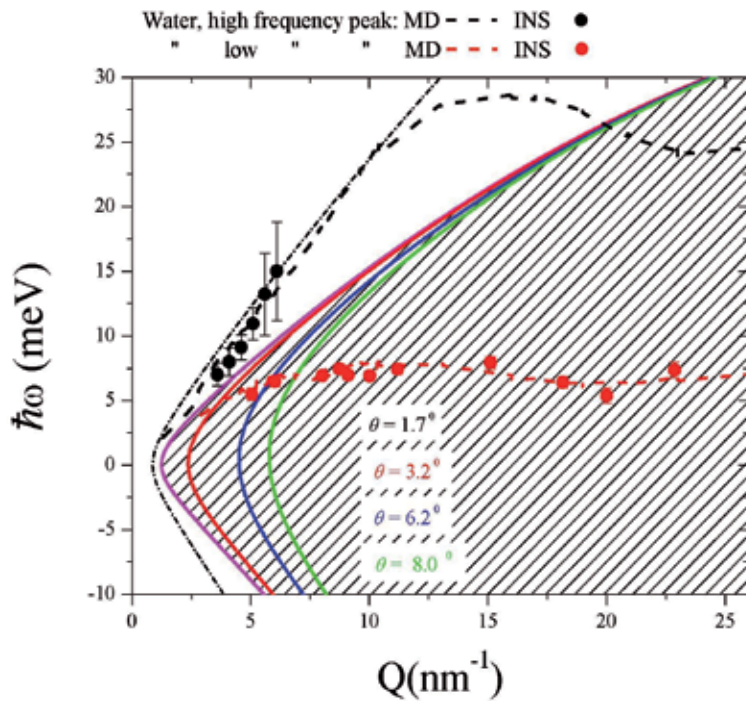
Figure 3. INS results in heavy water by [11] and [12] are reported as red and black dots, respectively, along with the MD simulation results of the two modes in the spectrum of water (dashed lines of corresponding color). The boundary of the explored dynamic region for the indicated scattering angle is reported with reference to the INS measurement by Bosi and coworkers. The shadowed area represents the dynamic domain accessible by such a measurement. The boundary of the dynamic plane explored by the Teixeira and coworkers' experiment is also indicated as a dot-dashed black line.

In particular, from the condition (2), it follows that, after the scattering event, the momentum of the photon $\hbar \vec{k}$ changes in direction, yet not in amplitude; therefore, one has:

$$Q^2 = k_{\mathrm{I}}^2 + k_{\mathrm{F}}^2 - 2k_{\mathrm{I}}k_{\mathrm{F}}\cos(2\theta) = 2k_{\mathrm{I}}^2\left(1 - \cos 2\theta\right) = \left(\frac{4\pi}{\lambda}\right)^2 \sin^2(\theta), \tag{37}$$

where $k_{\mathrm{F}} = k_{\mathrm{I}} = 2\pi/\lambda$, λ is the incident wavelength. The above formula shows that, for IXS, Q and ω are uncoupled, and, specifically, Q depends only on scattering angle and incident wavelength. This implies that the accessible portion of the dynamic plane is virtually unlimited at high (Q,ω) (virtual absence of kinematic limitations), while at small (Q,ω), it is still limited by the finite energy and momentum resolution of the spectrometer.

Taking advantage of the extension in the covered dynamic domain as well as of the statistical accuracy achievable with new synchrotron sources, recent IXS measurements on water droplets [13] evidenced a rather complex spectral shape. This contains both high and low

frequency inelastic modes, reminiscent of the sharper peaks dominating the phonon spectrum of ice, also measured in the same work. This clearly emerges from the two panels of Figure 4: the upper one, comparing the IXS measurement on a water droplet [13] to the INS one on heavy water [11] and lower one, which displays the IXS spectrum of ice.

It clearly appears that the superior spectral contrast of the INS measurement is the key to properly resolve the low energy mode, although this can only be achieved in a restricted dynamic range excluding all high frequency modes.
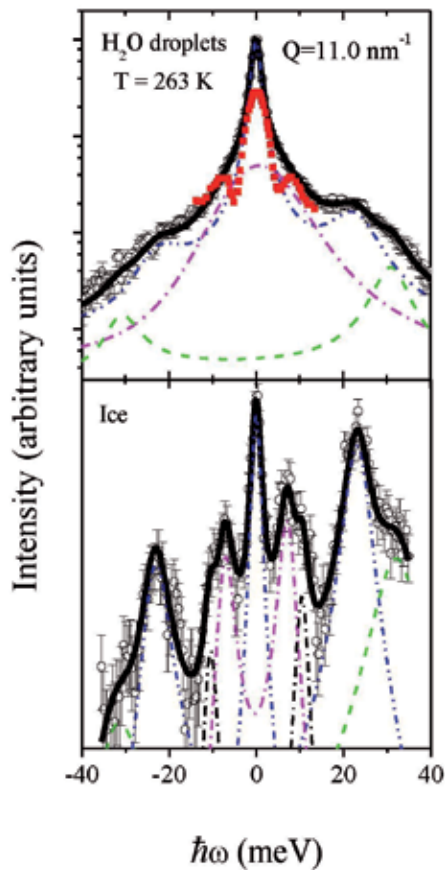
Figure 4. IXS spectra measured in a droplet of supercooled water (upper panel) and in ice (lower panel). Data are re-drawn from [13] and are reported along with best fit line shape (thick black lines) and the various inelastic components (dotted lines). The INS spectrum of bulk heavy water at ambient temperature and same Q values is reported in the upper plot as redrawn from [11], after rescaling for an arbitrary intensity factor (red dots).

3.1.2. Constant Q scans

One of the major drawbacks of INS is that scans of E performed at constant θ in general do not provide a fixed-Q measurement, yet they change the Q value through Eq. 30. This E–Q coupling

is usually inconvenient because most theoretical models deal with constant Q (rather than constant θ) cuts of $S(Q,\omega)$. Two strategies are commonly used in INS experiments to measure constant Q spectra. The one firstly developed [1] is based on the use of triple axis spectrometers [14] in which θ and E movements can be coordinated to keep Q constant (through Eq. 30). This technique is rather time consuming since no more than one Q value can be measured in each scan. Conversely, time of flight (*ToF*) spectrometers [15] enable to map $S(Q,\omega)$ surfaces with points sparse in the (Q,ω) plane, which makes this technique much less time consuming. However, constant Q cuts of $S(Q,\omega)$ can only be interpolated using analytical models, yielding questionable results when $S(Q,\omega)$ surfaces are not sufficiently smooth.

3.1.3. Incoherent scattering

As discussed above, the incoherent scattering contribution to IXS intensity essentially arises from random fluctuations of the electronic form factor, $f(Q)$, while for INS it originates from fluctuations of the scattering length b. The latter depends on Z, A (the atomic number), and $\bar{J}$, the total (electron + nuclear) magnetic moment. The resulting scattering strength can thus be very different not only for different isotopes of the same material, but also for the same isotope species if these have total magnetic moment with different orientations. This can cause substantial mean square fluctuations of b, which provide a significant contribution to the incoherent part of the neutron cross section (indeed $\propto |\langle b \rangle|^2 - \langle |b|^2 \rangle$). Obviously, this is a serious drawback if the experiment aims at investigating the collective dynamics of the sample, as for the examples discussed in this chapter. However, it represents a valuable resource when the experiment focuses on single molecule's dynamics of, because the incoherent scattering provides direct insight on it. In this respect, highly hydrogenated systems are ideal sample for incoherent INS measurements, owing to almost fully incoherent character of the INS cross section of hydrogen.

3.1.4. Incident flux on the sample

Although IXS can be considered a "photon hungry" technique, state of art IXS spectrometers have incident fluxes much higher than that their INS counterparts. Typically, IXS beamlines can produce a photon flux of 10^9–10^{10} photons/s within a focal spot as narrow as 100 μm^2, while for ToF spectrometers, a flux of ≈10^5 photons/s is typically achieved within focal spot of a few square centimeters. Although the collection/spectral analysis of IXS spectrometers ultimately imposes severe intensity penalties, mostly due to the relatively low angular acceptance of IXS analyzers, the final count rate of meV-resolution IXS measurements is usually much higher than that of their INS counterparts.

3.1.5. Multiple scattering

As mentioned, the leading contribution to the attenuation of IXS signal is the photoelectric absorption, which, on the bright side, also causes a strong suppression of multiple scattering events. As a consequence, in IXS measurements the multiple scattering intensity is often negligible compared to the single scattering signal, which is the one proportional to $S(Q,\omega)$. The situation is radically different for INS measurements, for which the attenuation is

dominated by the scattering process itself, and, therefore, multiple scattering events substantially contribute to the inelastic signal.

3.1.6. Transverse beam size

The incident beam of typical IXS spectrometers has an extremely small focal spot, usually few tens of square micrometer or even less. This permits IXS experiments to deal with small-sized samples, thus potentially disclosing the access to extreme thermodynamic conditions, such as high pressure and extremely low or high temperature. This is also a valuable asset when dealing with samples only available in small volumes. The use of smaller samples in IXS measurements is also fostered by the usually high absorption, especially for high Z materials. Conversely, the neutron beam is much larger in size and, also, more deeply penetrating inside the matter and this makes small samples relatively "transparent" to this technique.

3.2. Part B: advantages of INS

3.2.1. Resolution shape

Probably, the most important advantage of INS over IXS is the narrower and sharper energy resolution function. Most importantly, INS offers the opportunity of tailoring the energy resolution width .In fact, the latter can be narrowed according to the specific needs of experimenters, although, unavoidably, to the cost of a shrinkage of the dynamic range covered. The use of a narrow and sharp resolution is crucial in many applications including, for instance, the study of the slow dynamic response of highly viscous systems as glass formers approaching the melting. In fact, in this case all relevant spectral features concentrate in the so-called quasi-elastic region of the spectrum. Resolution functions as narrow as a few meV can be reached using cold neutrons as a probe. Furthermore, INS resolution profiles are usually sharp (nearly Gaussian) as opposite to the broad (mostly Lorentzian) IXS resolution wings.

Although new concept IXS spectrometers discussed in the following promise a drastic improvement of both resolution width (sub-meV) and spectral contrast, the performance of quasi-elastic neutron scattering instruments [16] is unlikely to be ever matched by IXS spectrometers.

3.2.2. Q-decay of the cross section

Due to the highly localized interaction of neutrons with the target nuclei, no appreciable Q decay of the scattering length can be observed up to Q values of the order of the inverse of the nuclear size. This value is nearly a factor 10^3 larger than the typical Q value at which the IXS cross halves its $Q = 0$ value. For this reason, the use of neutrons is particularly convenient for extremely high Q measurements probing the so-called single particle, or impulse approximation, regime [17]. Indeed, the access to this regime has been an exclusive task of deep inelastic neutron scattering (DINS) for decades ([18]. Although some successful attempts to reach the impulse approximation with IXS have been reported in the literature [19], the maximum Q

reached by these measurements is still smaller than the range covered by DINS for more than two orders of magnitude.

3.2.3. Absorption

As mentioned, at the typical incident energies of IXS, the scattered intensity is mostly attenuated by the photoelectric absorption, whose coefficient μ is proportional to Z^4. In high Z samples the absorption dominates over the Thomson scattering term, thus making IXS of limited efficiency for these materials. Conversely, the neutron absorption cross section is, in most cases, relatively low, which makes neutrons an ideal, non-destructive, probe of bulk properties of materials. The low absorption is also a crucial pre-requisite to probe biological systems because a low incident flux reduces the risk of radiation-induced damage in these samples [20]. Consequently, complex or delicate biological materials can be studied less destructively than any other forms of high energy radiation. Even in vivo studies are now being carried out using neutron probes, an area that has great potential for further development and applications in medical research.

On the other hand, the larger penetration depth of neutron probes comes in handy in some large volume high-pressure applications, as it makes the design of high-pressure vessels more straightforward. In fact the cell body can be often penetrated by the neutron beam with no need of using neutron-transparent windows, thereby drastically reducing the risk of high-pressure leaks.

3.2.4. Single particle dynamics

The neutron cross section of hydrogen is substantially higher than the one of other atomic species and is almost completely incoherent. This represents a key advantage when studying the single particle response of hydrogen compounds as well as hydration patterns in proteins and other macromolecules [21].

3.2.5. Contrast variation

When the sample is embedded or floating in a substrate, as for confined systems, solutions, and so on, it is often useful to improve the contrast of the measurement, i.e. the difference between the scattering intensity from the confined sample and the one from the substrate. In principle, the contrast can be enhanced by manipulating the scattering density of a specific component.

However, the IXS intensity of a given component can only be manipulated changing the atomic number, i.e. altering the chemical species. Conversely, the neutron scattering cross section is isotope-specific. Therefore, the scattering can be substantially manipulated through the change of the isotopic composition in the sample, i.e. without altering its chemical properties. This suggests to modulate the cross section by means of a mere isotopic substitution to optimize the contrast [22].

3.2.6. Isotopic substitution

As discussed just above, the INS cross section is isotope-specific, i.e. it depends on the nuclear mass, but not on the atomic number, or, equivalently, the chemical specie of the target sample. One method taking full advantage of this property is based upon parallel INS measurements on chemically equivalent systems in which an "isotopic substitution" has been implemented. In fact, by using a smart isotope manipulation, one in principle can selectively enhance the partial scattering contribution of different atomic species in a molecular sample, or in a mixture [22].

4. Present and future of IXS: ID28 beamline at ESRF and 10ID beamline at NSLS II

4.1. An example of state-of-art IXS spectrometer: ID28 beamline

As discussed in the introductory section, the investigation of collective modes in the spectrum of density fluctuations of fluids imposes a challenging requirement on the relative energy resolution ($\Delta E/E \leq 10^{-7}$). The implementation of IXS monochromators with the required $\Delta E/E$ demands the use of extremely high quality crystals, i.e. crystals having a relative lattice parameter variation, $\Delta d/d$, smaller than 10^{-7}, at least within their active part (diffracting volume).

Furthermore, to preserve the desired energy resolution without significantly reducing the photon flux, the whole divergence of the incoming photon beam must fall within the intrinsic angular acceptance of the considered monochromator reflection, i.e. the Darwin width, w_D. Within the dynamical theory of X-ray diffraction [23], the latter is given by:

$$w_D = (AE/E)h \tan\theta_B,$$

where h and θ_B are the Bragg reflection order and angle, respectively. Since $\tan\theta_B$ diverges for $\theta_B \approx 90°$, upon approaching a backscattering geometry w_D can be enhanced enough to accept the X-ray beams delivered by standard undulators' sources.

Therefore, it was predicted almost 50 years ago that the use of extreme backscattering geometries coupled with the small $\Delta E/E$ typical of high order (high h) Bragg reflections could in principle enable high-resolution (meV) IXS measurements. Historically, the first demonstration that the needed 10^{-7} relative resolution can be achieved with silicon crystals in backscattering geometry was given by [24] and [25]; these results were further developed by [26] for applications to IXS.

The $\Delta E/E$ ultimately achieved in these works was 5×10^{-7} with a photon flux of $\sim 10^6$ photons/s on the sample. However, the best performance achieved back at those times ($\Delta E/E \approx 3.5 \times 10^{-7}$ within 2.l µrad angular acceptance) exploited a "four bounce" crystal array, originally developed for resonant nuclear scattering with synchrotron radiation [27].

The first complete meV-resolution IXS spectrometer, ID16 beamline, was built on 1995 at the European Synchrotron Radiation Facility (ESRF) in Grenoble, France. Few years later another IXS spectrometer, ID28 beamline [31], was developed at *ESRF* with a similar design, yet enabling an extended Q-range coverage. This is the only meV-resolution spectrometer currently active at ESRF and its general description is concisely reported in the following. It is worth stressing, that other meV-resolution IXS spectrometers with slightly different layouts are currently available in Japan [32] and United States [33, 34].

As evident from Figure 5, the design of ID28 (and all current IXS spectrometers) is based on the triple axis concept, first developed in the mid-1950s [1]: the first axis locates at the monochromator crystal, and rotations around it are used to select the energy of incident photons. Rotations around the second axis, located at the sample position, change instead the momentum transfer $\vec{Q}$. Finally, the third axis is the one of the analyzer crystals, and, in principle, rotations around it determine the energy scattered photons, $\hbar\omega_f$. A more detailed layout and a picture of ID28 beamline can be found in Figures 6 and 7, respectively.

At variance of traditional triple axis schemes, implementing energy scans of scattered intensity through rotations of the analyzer crystal(s), at ID28 beamline, these are performed by changing the *d*-spacing of reflecting crystals through the scan of their temperature. The achievement of a $10^{-7} \div 10^{-8}$ relative energy resolution demands a millikelvin accuracy in the temperature control of the monochromator/analyzer optics. This is obtained by using a carefully designed temperature bath controlled by an active feedback system with a precision of 0.2 mK at ambient conditions.
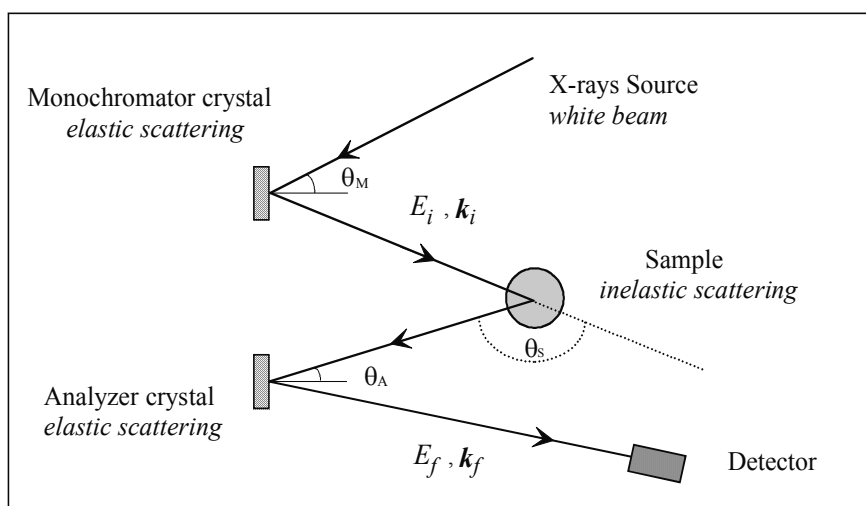
Figure 5. The general scheme of the ID28 IXS spectrometer at ESRF.

The X-ray source consists of three undulators having 32 mm magnetic period, placed in a straight high-beta β section of the electron storage ring. The utilized X-ray radiation energies

correspond to the undulator emission of the third or fifth harmonic. The X-ray beam delivered at these harmonics has $\Delta E/E \approx 10^{-2}$, a 40×15 μRad (horizontal × vertical) angular divergence and about 200 W integrated power. Such a beam is pre-monochromatized to $\Delta E/E \approx 2 \times 10^{-4}$ $\Delta E/E \approx 2 \cdot 10^{-4}$ using a silicon, Si(1,1,1), in vacuum and cryogenically cooled channel-cut crystal. Its main task is to absorb the relevant portion of the irradiated power that will be otherwise impinging on the main monochromator, thus drastically reducing its heat load. This is required to minimize thermal deformations induced on the monochromator crystal that can drastically degrade the energy resolution. The x-photon beam filtered by the pre-monochromator is then back reflected by the high-resolution monochromator, consisting of an asymmetrically cut silicon crystal oriented along the [111] direction and operated at a Bragg angle of 89.98°. This extreme backscattering geometry minimizes geometrical contributions to the total energy resolution broadening. Under these conditions, the angular acceptance of the monochromator is larger than the X-ray beam divergence and all photons are thus reflected within the desired energy bandwidth. Both the use of high-order Bragg reflections (h,h,h) with $(h = 7,8,9,11,12,13)$ and the superior quality of the active optics are required to ultimately achieve the needed relative resolution $\Delta E/E \approx 10^{-7} \div 10^{-8}$. The monochromatic beam is focused on the horizontal and vertical planes by a platinum-coated toroidal mirror, located 25 m upstream of the sample, which provides a 250×80 μm^2 full width at half maximum (FWHM). More performing optical elements are also available at ID28 to focus the beam down to 30 × 40 μm².
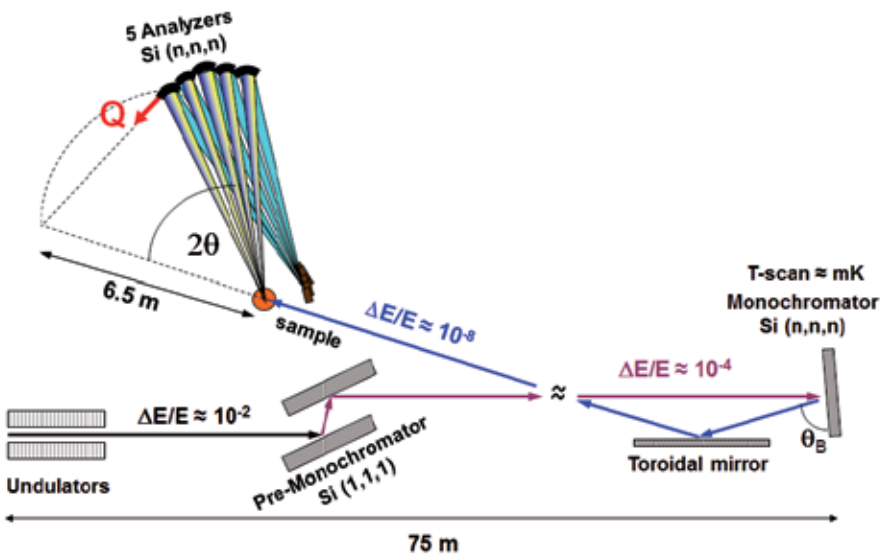
Figure 6. The schematic layout of ID28 beamline at ESRF (courtesy of F. Bencivenga).

The energy of the radiation scattered by the sample is analyzed by five spherical analyzers (nine in the upgraded instrument) mounted on the tip of an horizontal arm, which can be rotated by an angle 2θ so as to reach the desired exchanged momentum. These five (nine)

analyzer units have a mutual angular offset, which enables the simultaneous collection of IXS spectra at five (nine) different Qs. Although the problems connected to the energy resolution are conceptually the same for monochromator and analyzer, the required angular acceptance is very different in the two cases. For the analyzer, the optimal angular acceptance results from the best compromise between conflicting count rate and Q-resolution requirements. In fact, albeit a reduction of the angular acceptance improves the momentum resolution, it reduces the overall count rate.

Figure 7. The ID28 beamline's spectrometer arm of at ESRF (from the ID28 beamline's website, courtesy of A. Bosak)

Considering that for typical IXS measurements an acceptable Q spread is, at the lowest Q's, $\Delta Q_M \leq 0.1 \div 0.5 \text{ nm}^{-1} \ 0.1 \div 0.5 \ nm^{-1}$, the angular acceptance of the analyzer is correspondingly set to few milliradians, a value much larger than the Darwin width of the Bragg reflections typically used. The only option to achieve such a large acceptance is the design of a focusing system, which, however, must minimize possible distortions of the d-spacing ultimately degrading the energy resolution. The solution actually adopted at ID28 beamline is a mosaic of ≈12,000 silicon perfect single square crystals glued on a spherical surface. These analyzer arrays are operated in a 1:1 pseudo-Rowland circle geometry with aberration low enough not to degrade appreciably the desired energy resolution [28].

Each analyzer is equipped with motorized entrance slits setting the desired Q-resolution, its back-reflection being intercepted by Peltier-cooled silicon diode with extremely low dark count (≈1 count over 30 minutes).

The spectrometer arm can be rotated around a vertical axis passing through the sample by an < 55°, which corresponds to Q < 100 nm^{-1}, for Si(11,11,11) monochromator/analyzer Bragg reflection.

The measured resolution profile of the instrument has a FWHM of approximately 1.5 meV, as required to perform spectroscopy measurements of the high frequency dynamics of disordered systems.

4.2. Toward a new generation IXS spectrometer

On a general ground, high resolution measurements as the one discussed above suffer from major drawbacks: the relatively large width of the resolution (≥1 meV) and, perhaps more importantly, the poor spectral contrast, i.e. the slowly decaying (essentially Lorentzian) wings of the instrumental resolution profile. The development of next generation IXS instruments using a new monochromatization/energy analysis holds the promise of effectively tackling these problems.

Currently, state-of-art IXS spectrometers have a working principle similar to the one of the ID28 beamline of ESRF illustrated above, i.e. they use extreme backscattering geometries in which the energy analysis is implemented through temperature scans [28].

In these schemes, the final achievement of a meV-resolution resolution is challenged by two major difficulties: (1) the energy analysis imposes tight constraints on the temperature stability of the optics, as only <10^{-4} K temperature gradients can be tolerated and (2) the higher order Bragg reflections are more deeply penetrating into reflecting crystals, thus being severely affected by extinction losses.

A few alternative schemes based on the dispersion character of Bragg back reflection from asymmetrically cut crystals [35] have been successfully tested. Namely:

1. an array of four silicon crystals, customarily referred to as 4-bounce monochromator [36] and

2. an assembly of collimator (*C*), dispersive (*D*), and wavelength (*W*) selector crystals, usually referred to as *CDW*, or *CDDW*, if two dispersive crystals are used instead [37].

Both optical schemes demonstrated to provide sub-meV broad and extremely sharp, essentially Gaussian, resolution profiles. Furthermore, these optical schemes have a wealth of advantages when compared to current backscattering IXS spectrometers:

1. They do not use high order Bragg reflections, which greatly improves their overall efficiency. In fact, they are operated at moderate energy values at which synchrotron undulators usually perform best.

2. The spectral contrast, i.e. the sharpness of the resolution function, is greatly enhanced by the multiple reflection bounces.

3. They are extremely flexible, offering the opportunity of changing incident energy and tailoring the resolution to any specific needs.

The feasibility of these schemes for IXS application was recently demonstrated [38]. Most importantly, a novel instrument (10ID beamline) with a very narrow (sub-meV) and sharp (essentially Gaussian) resolution function [39, 40] will be soon operated at the new synchrotron source NSLS-II in Upton, New York. A schematic representation of the various components of such a beamline is provided in Figure 8.
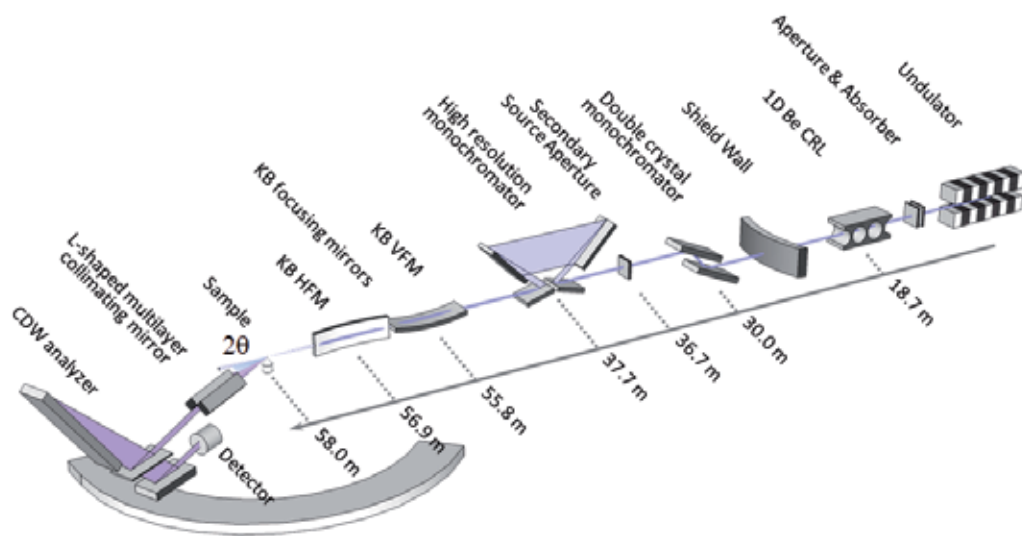
Figure 8. A schematic layout of the new high resolution IXS spectrometer soon available at NSLS II, taken from [40].

5. An example of a joint IXS and IXS experiment: the study of a shear mode propagation in water

Among various topics emerging from the vast literature on THz measurements of $S(Q,\omega)$ of liquids, one of the most controversial focuses on the presence of a second, low frequency, mode in the spectrum of water. More than other research subjects, this topic lends itself to the synergic use of the two complementary THz spectroscopic methods discussed above: IXS and INS.

As mentioned, the presence of the the low-frequency peak of water was also reported in the INS work of [11] and in the later INS measurement by [41]. Both these works, owing to the mentioned kinematic limitations, could not access to the high frequency back then referred, somehow misleadingly (see [42, 43]), to as the "fast sound mode", which was instead observed in the INS work of Teixeira and coworkers [12]. For a long time, the low frequency mode was interpreted as the finite-Q extension of the macroscopic sound mode, based on the overall

consistency between the slope of its low Q dispersion curve and the known value of the adiabatic sound speed [44]. This interpretation was confuted years later by both MD [10] and IXS [45] studies of the water spectrum, which demonstrated that such low frequency mode has instead a transverse acoustic origin. This interpretation initially raised some controversy [46, 47], but found important validations in successive IXS works [13, 45]; a concise account of these studies can be found in [48].

In a way, the onset of a transverse mode in the spectrum of a disorder material may not be too surprising as one recognizes that quasi-polarized (transverse or longitudinal) modes are routinely observed in the inelastic spectra of poly-crystals in the first-Brillouin zone. Therefore, the hypothesis that a definite polarization, either longitudinal or transverse, are intertwined has in principle some ground for a liquid system, especially over distances matching the size of molecular disorder. However, it is broadly accepted that a longitudinal or transverse polarization can be still assigned to a mode in the mesoscopic regime, provided such a mode dominates the current spectra of corresponding – longitudinal or transverse – polarization. Longitudinal current spectra $C_L(Q,\omega)$ are directly determined from the experimentally measured $S(Q,\omega)$ using $C_L(Q,\omega) = (\omega/Q)^2 S(Q,\omega)$. Conversely, transverse current spectra $C_L(Q,\omega)$ can only be determined by computer simulations as the Fourier transform of the autocorrelation function between transverse components of atomic velocities.

It is worth recalling that the (transverse or longitudinal) polarization of the acoustic mode is defined in reference to the direction of the exchanged momentum $\hbar\vec{Q}$. In this respect, it is useful to recall that $S(Q,\omega)$ is the Fourier transform of the correlation function $\sum_{jk}\langle\exp[i\vec{Q}\cdot\vec{R}_k(t)]\exp[i\vec{Q}\cdot\vec{R}_k(t)]\rangle$. Clearly, the presence of the $\vec{Q}\cdot\vec{R}_i(t)$ term in the exponents shows that only longitudinal movements, i.e. movements along the $\vec{Q}$ direction, are relevant to $S(Q,\omega)$. Transverse modes are therefore visible in the $S(Q,\omega)$ shape only indirectly, via the so-called longitudinal–transverse (L–T) coupling. This mainly consists in a coupling between transverse and longitudinal waves, which occurs above some Q threshold. For instance, in water, this threshold was located at 4 or ≈6 nm^{-1} by [49] and [50], respectively.

The onset of an L–T coupling in liquids has been often associated to the intrinsically "open" (large free volume) tetrahedral structure of water, as opposite to the essentially close-packed arrangement of "normal" fluids. In fact, an L–T coupling has been observed in tetrahedral systems such as water itself as well as GeO_2 [52] and $GeSe_2$ [53].

However, nowadays, this interpretation needs some reconsideration because the L–T coupling was also observed in non-tetrahedral systems, such as glassy glycerol [54] and liquid metals [55-59]. Furthermore, a similar effect was reported in more complex systems such as binary mixtures [51] and biophysical samples [60-62].

On a general ground, the ability to support shear propagation can be considered as a manifestation of the solid-like response of a fluid at short times and distances. This seems consistent to the early IXS work of [49], where substantial similarities between the THz dynamic response of water and ice were suggested. Also, based on previous lattice vibrations, i.e. calculations and INS measurements [64], this additional spectral feature in water was assigned to the transverse optical (TO) visible in ice. Consistently with this scenario, the IXS work of Ponte-

corvo and coworkers [45] also demonstrated that an L–T coupling is only visible when density fluctuations propagate at frequencies larger than the inverse of the relaxation time $1/\tau$. Under these conditions, acoustic waves "perceive" the propagation medium as frozen as expected for a glass. These slows degrees of freedom cannot energetically couple with the acoustic wave, which, therefore, travel "elastically," that is keeping its energy constant. The virtual lack of acoustic dissipation of this elastic regime is reflected by the higher sound velocity and the lower sound damping. Furthermore, restoring forces become more effective in fostering a sound propagation in the shear plane. This seems consistent with the result of a successive IXS work [13], where a study of shear mode propagation was jointly performed in normal liquid, solid, and supercooled phase of water.

5.1. The joint use of IXS and INS

The various IXS investigations of transverse propagation in water mentioned above often pushed to limit the capability of this spectroscopic method; as a matter of fact, these studies could be successfully accomplished either reaching somehow extreme thermodynamic conditions (high density and/or low temperature) or accessing to large Q values.

The observation of a transverse mode at low Q's or at high T's would have required a sharp and narrow resolution function, definitely beyond the current capability of IXS. In principle, INS measurements can offer the required resolution performance, but only by confining the covered dynamic range within a restricted region excluding the longitudinal, high frequency, mode (see data reported in Figure 3). A possible method to circumvent these complementary limitations foresees simultaneous IXS and INS measurements on the same heavy water sample.

This is the strategy followed by joint INS–IXS measurement in heavy water [50] and in a successive one on deuterated water–glycerol mixtures [51]. The use of deuterated samples was, of course, imposed by the highly incoherent INS cross section of hydrogen, which would have prevented the INS measurement to reliably determine the coherent spectrum. In these two measurements, the INS spectrometer was operated using an extremely narrow (<0.1 meV) and essentially Gaussian resolution profile, as required for an optimal characterization of the low frequency portion of the spectrum. The parallel use of IXS allowed to dramatically extending the low energy range covered by the neutron experiment. Figure 9 provides an example of spectra measured in heavy water by these two complementary techniques.

Consistent to the other works in the literature [65], the spectrum was approximated by a viscoelastic model accounting for the longitudinal component of density fluctuations, while the additional peak in the spectrum generated by the L–T coupling was approximated by a simple Damped Harmonic Oscillator (DHO) term [66]:

$$\frac{S(Q,\omega)}{S(Q)} = (1 - \tilde{T})S_{VE}(Q,\omega) + \tilde{T}\frac{1}{\pi}\frac{2\Omega_t^2\Gamma_t}{\left[\omega^2 - \Omega_t^2\right]^2 + 4\Gamma_t^2\omega^2}, \tag{38}$$

where the suffix "VE" labels the viscoelastic model, while Ω_t and Γ_t represent, respectively, the characteristic frequency and damping of the low-frequency excitation. Finally, $\tilde{T}$ is a Q-
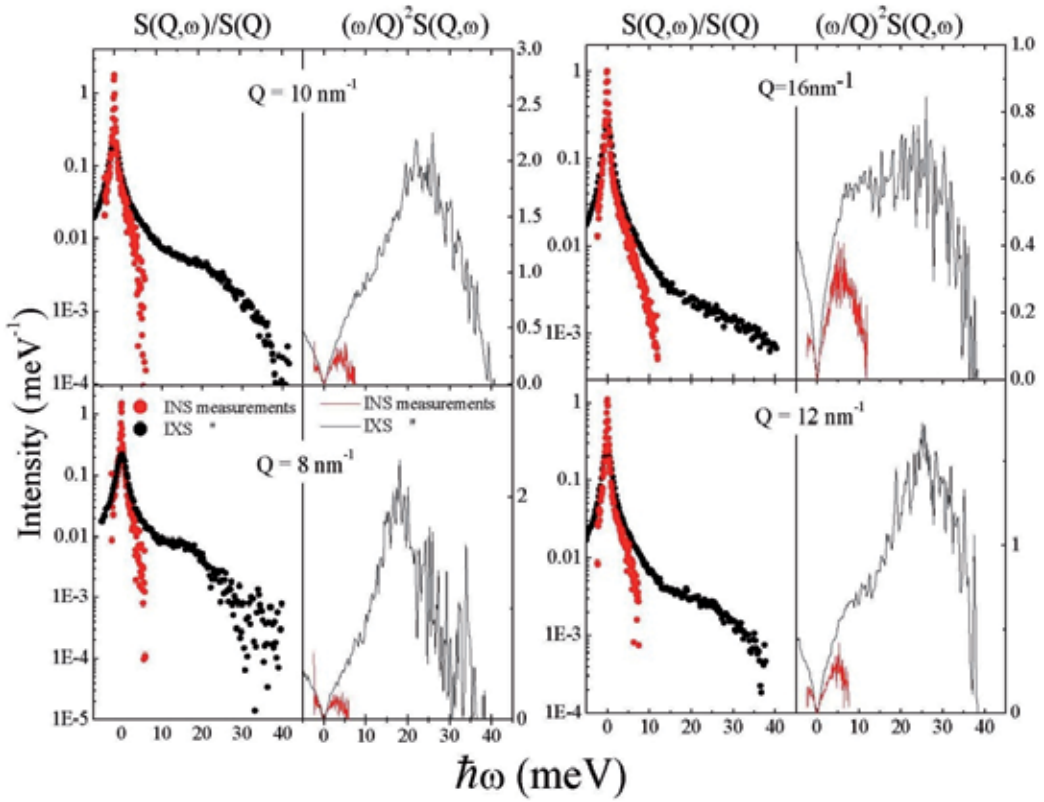
Figure 9. Representative IXS (black dots) and INS (black dots) measurements of water spectra are reported along with the corresponding current spectra (lines of corresponding color). All reported curves are normalized to the S(Q) for consistency. Data are redrawn with permission from Ref. [51], which is copyrighted by the American Physical Society.

dependent scaling factor, yielding the relative weight of the DHO component. Within the hypothesis that the DHO term arises from the L–T coupling, $\widetilde{T}$ provides a measure of the strength of such coupling. An important outcome of this joint measurement is reported in Figure 10.

It clearly appears that at low Q, the transverse mode becomes heavily damped, being its frequency nearly equal to the damping, and therefore, the transverse perturbation assumes a essentially non-propagating character. Interestingly, when this low Q regime is reached, both acoustic frequency and damping are of the same order and the elastic (solid-like) character of the dynamics is lost. At even lower Q values, no clear evidence of a transverse mode in the spectrum can be inferred from measured spectral shape.

The trend discussed above indicates that below the Q threshold of the L–T mode, the inelastic peak merges into the quasi-elastic mode typical of all fluids exhibiting a viscoelastic behavior. This is the well-known Mountain [67] mode, which arises from the coupling of density fluctuations with active relaxation processes.
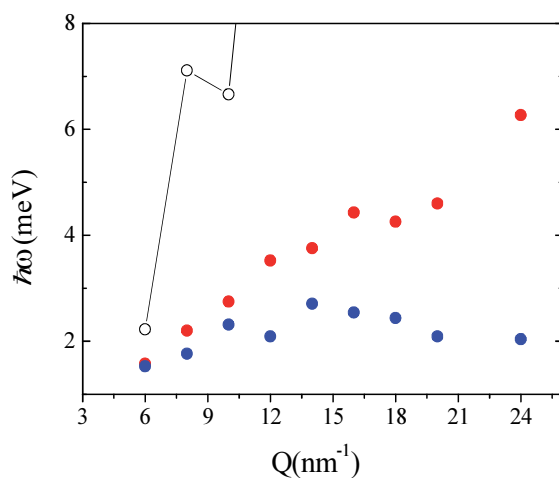
Figure 10. The Q dependence of the frequency Ω_t (red dots) and the damping Γ_t (blue dots) of the transverse acoustic mode in water spectrum are reported along with the inverse of the relaxation time (open circles + line). Data are re-drawn with permission from Ref. [51], which is copyrighted by the American Physical Society.

Acknowledgements

Author details

Alessandro Cunsolo

Address all correspondence to: acunsolo@bnl.gov

National Synchrotron Light Source II, Brookhaven National Laboratory, Upton, NY, USA

References

[1] Brockhouse BN, Stewart AT. Scattering of neutrons by phonons in an aluminum single crystal. Phys. Rev. 1955; 100:756-757. DOI: http://dx.doi.org/10.1103/PhysRev. 100.756

[2] Goodman JW. Introduction to Fourier optics. 3rd ed. Grenwood Village: Roberts and Company Publishers; 2005.

[3]   Jackson JD, Jackson JD. Classical electrodynamics. Vol. 3. New York: Wiley, 1962.

[4]   Sinha SK. Theory of inelastic x-ray scattering from condensed matter. J. Phys. Condens. Matter 2001, 13:7511-7523. DOI: http://dx.doi.org/10.1088/0953-8984/13/34/304

[5]   Dirac PA. The quantum theory of the emission and absorption of radiation. Proc. R. Soc. A, 1927, 40:243-265.

[6]   Van Hove L. Correlations in space and time and born approximation scattering in systems of interacting particles. Phys. Rev. 1954, 95:249-262. DOI: http://dx.doi.org/10.1103/PhysRev.95.249

[7]   Schulke W. Inelastic scattering by electronic excitations. In: Brown G, Moncton DE, editors. Handbook on synchrotron radiation, Amsterdam:Elsevier, 1991; Vol. 3.

[8]   Lovesey SW. Theory of neutron scattering from condensed matter. Oxford: Clarendon Press, 1984; Vol. 1.

[9]   Rahman A, Stillinger FH. Propagation of sound in water. A molecular-dynamics study. Phys. Rev. A 1974, 10:368-378. DOI: http://dx.doi.org/10.1103/PhysRevA.10.368

[10] Sampoli M, Ruocco G, Sette F. Mixing of longitudinal and transverse dynamics in liquid water. Phys. Rev. Lett. 1997, 79:1678-1681. DOI: http://dx.doi.org/10.1103/PhysRevLett.79.1678

[11] Bosi P, Dupré F, Menzinger F, Sacchetti F, Spinelli MC. Observation of collective excitations in heavy-water in 108 cm-1 momentum range. Nuovo Cimento Lett. 1978, 21:436-440. DOI: 10.1007/BF02763195

[12] Teixeira J, Bellissent-Funel MC, Chen SH, Dorner B. Observation of new short wavelength collective excitations in heavy water by coherent inelastic neutron scattering. Phys. Rev. Lett. 1985, 54:2681-2683. DOI: http://dx.doi.org/10.1103/PhysRevLett.54.2681

[13] Cimatoribus A, Saccani S, Bencivenga F, Gessini A, Izzo MG, Masciovecchio C. The mixed longitudinal-transverse nature of collective modes in water. New J. Phys. 2010, 12: 053008. DOI: http://dx.doi.org/10.1088/1367-2630/12/5/053008

[14] Shirane G, Shapiro SM, Tranquada JM. Neutron scattering with a triple-axis spectrometer: Basic techniques. Cambridge: Cambridge University Press, 2002.

[15] Windsor CG. Pulsed neutron scattering. London:Taylor & Francis, 1981.

[16] Bée M. Quasielastic neutron scattering : Principles and applications in solid state chemistry, biology and materials science. Bristol: Hilger, 1988.

[17] Silver RN, Sokol PE. Momentum distributions. New York: Springer Science+ Business Media, 2013.

[18] Sears VF. Scaling and final-state interactions in deep-inelastic neutron scattering. Phys. Rev. B 1984, 30:44-51. DOI: http://dx.doi.org/10.1103/PhysRevB.30.44

[19] Monaco G, Cunsolo A, Pratesi G, Sette F, Verbeni R. Deep inelastic atomic scattering of X rays in liquid neon. Phys. Rev. Lett. 2002, 88:227401. DOI: http://dx.doi.org/10.1103/PhysRevLett.88.227401

[20] Rheinstadter MC, Ollinger C, Fragneto G, Demmel F, Salditt T. Collective dynamics of lipid membranes studied by inelastic neutron scattering. Phys. Rev. Lett. 2004, 93:108107. DOI: http://dx.doi.org/10.1103/PhysRevLett.88.227401

[21] Middendorf HD. Biophysical applications of quasi-elastic and inelastic neutron scattering. Annu. Rev. Biophys. Bioeng. 1984, 13:425-451. DOI: 10.1146/annurev.bb.13.060184.002233

[22] Finney J, Soper A. Solvent structure and perturbations in solutions of chemical and biological importance. Chem. Soc. Rev. 1994, 23:1-10. DOI: 10.1039/CS9942300001

[23] Zachariasen W. A general theory of x-ray diffraction in crystals. Acta Cryst. 1967, 23:558-564. DOI: 10.1107/S0365110X670032

[24] Ando M, Bailey D, Hart M. A simple Bragg-spacing comparator. Acta Cryst. A 1978, 34:484-489. DOI: 10.1107/S0567739478001047

[25] Graeff W, Materlik G. Millielectron volt energy resolution in Bragg backscattering. Nucl. Inst. Meth. 1982, 195:97-103. DOI: 10.1016/0029-554X(82)90764-9

[26] Dorner B, Burkel E, Peisl J. An x-ray backscattering instrument with very-high-energy resolution. Nucl. Inst. Meth. A 1986, 246:450-451. DOI: 10.1016/0168-9002(86)90130-0

[27] Faigel G, Siddons DP, Hastings JB, Haustein PE, Grover JR, Remeika JP, Cooper AS. New approach to the study of nuclear Bragg scattering of synchrotron radiation. Phys. Rev. Lett. 1987, 58:2699-2701. DOI: http://dx.doi.org/10.1103/PhysRevLett.58.2699

[28] Masciovecchio C, Bergmann U, Krisch M, Ruocco G, Sette F, Verbeni R. A. Perfect crystal x-ray analyser with 1.5 meV energy resolution. Nucl. Inst. Meth. B 1996, 117:339-340. DOI: 10.1016/0168-583X(96)00334-5

[29] Verbeni R, Sette F, Krisch MH, Bergmann U, Gorges B, Halcoussis C, Martel K, Masciovecchio C, Ribois JF, Ruocco G, Sinn H. X-ray monochromator with 2 x108 energy resolution. J. Synchrotron Radiat. 1996, 3:62-64. DOI: 10.1107/S0909049595015883

[30] Sette F, Ruocco G, Krisch M, Bergmann U, Masciovecchio C, Mazzacurati V, Signorelli G, Verbeni R. Collective dynamics in water by high energy resolution inelastic x-ray scattering. Phys. Rev. Lett. 1995, 75:850-853. DOI: http://dx.doi.org/10.1103/PhysRevLett.75.850

[31] Krisch M. Status of phonon studies at high pressure by inelastic x-ray scattering. J. Raman Spectrosc. 2003, 34:628-632. DOI: 10.1002/jrs.1033

[32] Baron AQR, Tanaka Y, Miwa D, Ishikawa D, Mochizuki T, Takeshita K. Goto S, Matsushita T, Kimura H, Yamamoto F, Ishikawa T. Early commissioning of the Spring-8 beamline for high resolution inelastic X-ray scattering. Nucl. Inst. Meth. A 2001, 467:627-630. DOI: 10.1016/S0168-9002(01)00431-4

[33] Toellner TS, Alatas A, Said AH. Six-reflection mev-monochromator for synchrotron radiation. J. Synchrotron Radiat. 2011, 18:605-611. DOI: 10.1107/S0909049511017535

[34] Said AH, Sinn H, Divan R. New developments in fabrication of high-energy-resolution analyzers for inelastic x-ray spectroscopy. J. Synchrotron Radiat. 2011, 18:492-496. DOI: 10.1107/S0909049511001828

[35] Shvyd'ko Y. X-ray optics—high-energy-resolution applications, optical science. Berlin:Springer, 2004; Vol. 98.

[36] Yabashi M, Tamasaku K, Kikuta S, Ishikawa T. X-ray monochromator with an energy resolution of 8×10−9 at 14.41 kev. Rev. Sci. Inst. 2001, 72:4080-4083. DOI: http://dx.doi.org/10.1063/1.1406925

[37] Shvyd'ko YV, Lerche M, Kuetgens U, Ruter HD, Alatas A, Zhao J. X-ray Bragg diffraction in asymmetric backscattering geometry. Phys. Rev. Lett. 2006, 97, 13 235502. DOI: http://dx.doi.org/10.1103/PhysRevLett.97.235502

[38] Shvyd'ko Y, Stoupin S, Shu D, Collins SP, Mundboth K, Sutter J, Tolkiehn M. High-contrast sub-millivolt inelastic x-ray scattering for nano- and mesoscale science. Nature Commun. 2014, 5:4219. DOI: 10.1038/ncomms5219

[39] Cai YQ, Coburn DS, Cunsolo A, Keister JW, Honnicke MG, Huang XR, Kodituwakku CN, Stetsko Y, Suvorov A, Hiraoka N, Tsuei KD. The ultrahigh resolution ixs beamline of NSLS-II: Recent advances and scientific opportunities. In: Journal of Physics: Conference Series 2013 (Vol. 425, No. 20, p. 202001). IOP Publishing. DOI: http://dx.doi.org/10.1088/1742-6596/425/20/202001

[40] Suvorov A, Cai YQ, Sutter JP, Chubar O. Partially coherent wavefront propagation simulations for inelastic x-ray scattering beamline including crystal optics. InSPIE Optical Engineering+ Applications 2014 Sep 5 (pp. 92090H-92090H). International Society for Optics and Photonics. DOI: 10.1117/12.2061987

[41] Bermejo FJ, Alvarez M, Bennington SM, Vallauri R. Absence of anomalous-dispersion features in the inelastic neutron-scattering spectra of water at both sides of the melting transition. Phys. Rev. E 1995, 51:2250-2262. DOI: http://dx.doi.org/10.1103/PhysRevE.51.2250

[42] Ruocco G, Sette F. The history of the"fast sound"in liquid water. Condens. Matter Phys. 2008, 11:29-46.

[43] Cunsolo A. The Thz spectrum of density fluctuations of water: The viscoelastic regime. Adv. Cond. Matt. Phys. 2015, 2015:137435. DOI: http://dx.doi.org/10.1155/2015/137435

[44] Ricci MA, Rocca D, Ruocco G, Vallauri R. Collective dynamical properties of liquid water. Phys. Rev. Lett. 1988, 61:1958-1961. DOI: http://dx.doi.org/10.1103/PhysRevLett.61.1958

[45] Pontecorvo E, Krisch M, Cunsolo A, Monaco G, Mermet A, Verbeni R, Sette F, Ruocco, G. High-frequency longitudinal and transverse dynamics in water. Phys. Rev. E 2005, 71:011501. DOI: http://dx.doi.org/10.1103/PhysRevE.71.011501

[46] Petrillo C, Sacchetti F, Dorner B, Suck, JB. High-resolution neutron scattering measurement of the dynamic structure factor of heavy water. Phys. Rev. E 2000, 62:3611-3618. DOI: http://dx.doi.org/10.1103/PhysRevE.62.3611

[47] Sacchetti F, Suck, JB, Petrillo C, Dorner B. Brillouin neutron scattering in heavy water: Evidence for two-mode collective dynamics. Phys. Rev. E 2004, 69:061203. DOI: http://dx.doi.org/10.1103/PhysRevE.69.061203

[48] Cunsolo A, Suvorov A, Cai YQ. The onset of shear modes in the high frequency spectrum of simple disordered systems: Current knowledge and perspectives. Phil. Mag. 2015, 1-11. DOI: 10.1080/14786435.2015.1096975

[49] Sette F, Ruocco G, Krisch M, Masciovecchio C, Verbeni R, Bergmann U. Transition from normal to fast sound in liquid water. Phys. Rev. Lett. 1996, 77:83-86. DOI: http://dx.doi.org/10.1103/PhysRevLett.77.83

[50] Cunsolo A, Kodituwakku CN, Bencivenga F, Frontzek M, Leu BM, Said AH. Transverse dynamics of water across the melting point: A parallel neutron and x-ray inelastic scattering study. Phys. Rev. B 2012, 85:174305. DOI: http://dx.doi.org/10.1103/PhysRevB.85.174305

[51] Cunsolo A, Kodituwakku CN, Bencivenga F, Said AH. Shear propagation in the terahertz dynamics of water-glycerol mixtures. J. Chem. Phys. 2013, 139:184507. DOI: http://dx.doi.org/10.1063/1.4827108

[52] Bove LE, Fabiani E, Fontana A, Paoletti F, Petrillo C, Pilla O, Bento ICV. Brillouin neutron scattering of v-GeO2. Europhys. Lett. 2005, 71:563-569. DOI: http://dx.doi.org/10.1209/epl/i2005-10125-0

[53] Orsingher L, Baldi G, Fontana A, Bove LE, Unruh T, Orecchini A, Petrillo C, Violini N, Sacchetti F. High-frequency dynamics of vitreous GeSe2. Phys. Rev. B 2010, 82:115201. DOI: http://dx.doi.org/10.1103/PhysRevB.82.115201

[54] Scopigno T, Pontecorvo E, Di Leonardo R, Krisch M, Monaco G, Ruocco G, Ruzicka B, Sette, F. High-frequency transverse dynamics in glasses. J. Phys. Condens. Matter 2003, 15:S1269-S1278. DOI: http://dx.doi.org/10.1088/0953-8984/15/11/345

[55] Hosokawa S, Inui M, Kajihara Y, Matsuda K, Ichitsubo T, Pilgrim WC, Sinn H, Gonzalez LE, Gonzalez DJ, Tsutsui S, Baron AQR. Transverse acoustic excitations in liquid Ga. Phys. Rev. Lett. 2009, 102:105502. DOI: http://dx.doi.org/10.1103/PhysRevLett.102.105502

[56] Hosokawa S, Inui M, Kajihara Y, Matsuda K, Ichitsubo T, Pilgrim WC, Sinn H, Gonzalez LE, Gonzalez D.J, Tsutsui S, Baron, AQR. Transverse excitations in liquid Ga. Eur. Phys. J. 2011, 196:85-93. DOI: 10.1140/epjst/e2011-01420-5

[57] Hosokawa S, Munejiri S, Inui M, Kajihara Y, Pilgrim WC, Ohmasa Y, Tsutsui S, Baron AQ, Shimojo F, Hoshino K. Transverse excitations in liquid Sn. J. Phys. Condens. Matt. 2013, 25:112101. DOI: http://dx.doi.org/10.1088/0953-8984/25/11/112101

[58] Hosokawa S, Pilgrim WC, Sinn H, Alp EE. The possibility of transverse excitation modes in liquid Ga. J. Phys. Condens. Matt. 2008, 20:114107. DOI: http://dx.doi.org/10.1088/0953-8984/20/11/114107

[59] Giordano VM, Monaco G. Inelastic x-ray scattering study of liquid ga: Implications for the short-range order. Phys. Rev. B 2011, 84:052201. DOI: http://dx.doi.org/10.1103/PhysRevB.84.052201

[60] Paciaroni A, Orecchini A, Haertlein M, Moulin M, Conti Nibali V, De Francesco A, Petrillo C, Sacchetti F. Vibrational collective dynamics of dry proteins in the terahertz region. J. Phys. Chem. B 2012, 116:3861-3865. DOI: 10.1021/jp211190q

[61] Violini N, Orecchini A, Paciaroni A, Petrillo C, Sacchetti F. Neutron scattering investigation of high-frequency dynamics in glassy glucose. Phys. Rev. B 2012, 85: 134204. DOI: http://dx.doi.org/10.1103/PhysRevB.85.134204

[62] Li MD, Chu XQ, Fratini E, Baglioni P, Alatas A, Alp EE, Chen SH. Phonon-like excitation in secondary and tertiary structure of hydrated protein powders. Soft Matter 2011, 7:9848-9853. DOI: 10.1039/C1SM05954H

[63] Ruocco G, Sette F, Bergmann U, Krisch M, Masciovecchio C, Mazzacurati V, Signorelli G, Verbeni R. Equivalence of the sound velocity in water and ice at mesoscopic wavelengths. Nature 1996, 379:521-523. DOI: 10.1038/379521a0

[64] Renker B. Phonon dispersion in D2O-ice. Phys. Lett. A 1969, 30:493-494. DOI:

[65] Monaco G, Cunsolo A, Ruocco G, Sette F. Viscoelastic behavior of water in the terahertz-frequency range: An inelastic x-ray scattering study. Phys. Rev. E 1999, 60:5505-5521. DOI: http://dx.doi.org/10.1103/PhysRevE.60.5505

[66] Bafile U, Guarini E, Barocchi F. Collective acoustic modes as renormalized damped oscillators: Unified description of neutron and x-ray scattering data from classical fluids. Phys. Rev. E 2006, 73:061203. DOI: http://dx.doi.org/10.1103/PhysRevE.73.061203

[67] Mountain RD. Spectral Distribution of Scattered Light in a Simple Fluid. Rev. Mod. Phys. 1966, 38:205-214. DOI: http://dx.doi.org/10.1103/RevModPhys.38.205

Experimental Methods in the Study of Neutron Scattering at Small Angles

Cristian A. Dragolici

Additional information is available at the end of the chapter

Abstract

Scattering methods are powerful tools used for the examination of condensed matter. They offer the possibility to analyze particles without disturbing their natural environment. Small angle neutron scattering (SANS) can also be used to analyze solid and liquid systems, phase transformations, germination, growth flaws and defects, as well as generally any inhomogeneity occurring in a range of 10–1000 Å. The most common experimental SANS methods and patterns are reviewed and explained.

Keywords: SANS, methods, patterns

1. Introduction

1.1. Material science issues accessible through small angle scattering of X-rays (SAXS) and neutrons (SANS)

The fundamental properties of the neutron make it a powerful tool for materials science investigations. It is useful to introduce neutrons by comparison with X-rays because both probes are used for diffraction investigations, and more workers are familiar with X-ray methods. X-rays can be obtained with a generator tube or, in the past few years, at a synchrotron X-ray laboratory.

Neutrons for neutron beam research arise either from nuclear fission in reactors or from the spallation process. In the latter, accelerator-produced high-energy charged particles yield a large number of energetic neutrons from collisions with heavy-atom nuclei in the accelerator target.

X-ray diffraction was utilized for the first time in establishing the atomic structure of the crystals. Later, this method was used in other applications, extended to the study of imperfections in crystals, of the size of the crystallites, and even to the study of amorphous objects. From the classical discovery by Laue, in 1912, that X-rays are diffracted on their passage through crystals, the development of the applied domain of this technique was due to the subsequent progress of the X-ray diffraction theory and the improvement of experimental methods. The first observations on small angle X-ray scattering (SAXS) were performed in the beginning of the 1930s [1], and its domain was developed later.

In the following years, the small angle X-ray scattering technique has known to be an important development, proved by a great number of publications over the years. SAXS technique was developed from the necessity to observe long lattice spacing in crystals, in comparison with wavelengths of the X-rays used in structural analyses. Such distances are encountered in certain minerals and certain complex molecules such as polymers or proteins. For example, in the study of macromolecular crystals, the systems for X-ray diffraction should be extended to include the very small angles. The fundamental equation which describes the X-ray diffraction in the crystalline substance is $\lambda = 2d\sin\theta$, which shows that the diffraction angle θ inversely varies with the separation distance of the crystalline lattice planes (see Fig. 1) which generates the considered diffraction maximum.
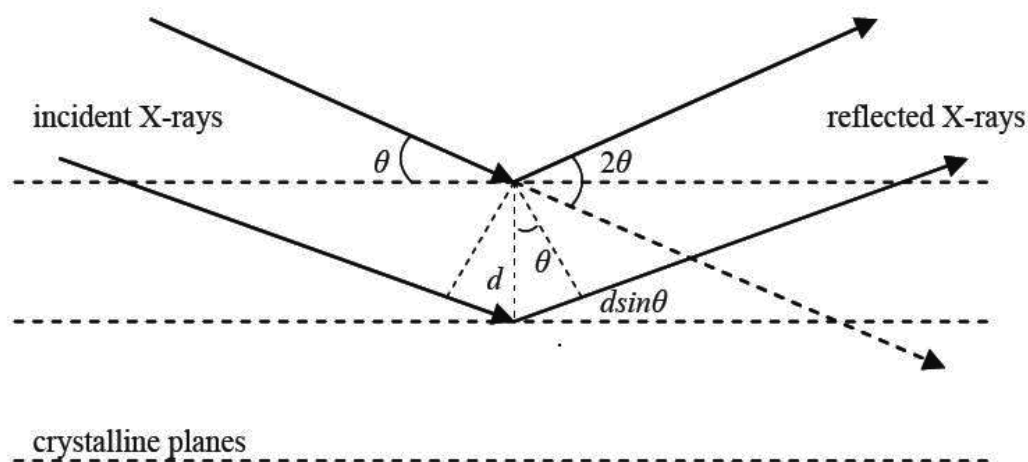
Figure 1. Bragg diffraction of the X-rays.

In ordinary crystals, especially those of inorganic matter, most inter-lattice distances observed are on the same magnitude with the wavelength of utilized X-rays; therefore the used θ angles are quite large. For example, let us consider the radiation Cu k_α and an inter-lattice distance of 100 Å, which would result in a diffraction θ angle of 0.45°; for a distance of 1000 Å, θ would be 0.045° or 2.6′. All these examples had shown the importance of SAXS techniques in biology, biochemistry, etc. Using X-rays with long wavelength to obtain larger diffraction angles for a specific inter-lattice distance is strictly limited by the variation of the material X-ray linear

absorption coefficient with radiation wavelength. Because X-rays are strongly absorbed by the traversed substance, it also became necessary for the utilization of other particles with higher penetrability due to their weak interaction with the matter they are passing through. Elsasser first observed in 1936 that neutron movement could be determined by wave mechanism, and later two experiments were conducted by Halban and Preiswerk and Mitchell and Powers, respectively, which validated this theory [2]. These experiments were performed using source emitting neutrons of different energies, without considering collimation or monochromation of that beam. However, all these conditions were sufficient to emphasize the neutron diffraction but without providing quantitative data. The development of nuclear reactors made possible the availability of neutrons in a very large number to allow collimation in beams, and separation by energy in a narrow band. This was the beginning of the neutron diffraction technique, very similar to X-ray diffraction.

The first device of this type, initially called "neutron spectrometer," was built for the first time in 1945 at Argonne National Laboratory in USA. Since then, many instruments with different shapes and conception were built around the world, and they are mostly known as "neutron diffractometer." The investigation of condensed matter with the help of neutrons is not a substitute for classical X-ray diffractions, but it is a completion of these techniques, because the special nature of neutron interaction with the substance allows the neutron diffraction to provide information that cannot be revealed by other means. The spectrum of neutrons emitted by a reactor is dependent on the moderator temperature, and in most reactors, the spectrum peak is around 1.5 Å. This spectrum is Maxwellian and has a maximum which depends on the temperature. Therefore, for T = 273 K, λ_{max} is around 1.55 Å, and for T = 373 K λ_{max} is 1.33 Å. Using "hot sources," it is possible to move the maximum of the neutron spectrum to short wavelengths up to 0.4 Å. In a similar manner, by cooling the moderator, the maximum of the neutron spectrum can be moved to long wavelengths. We can observe that neutron beams, as spectrum broadening, become comparable with X-ray beams, where the normal range of wavelengths is from 2.2 Å (Cr K_α) to 0.56 Å (Ag K_α), thereby having the advantage of being less absorbed by the matter than X-rays. In the last years, in the competition between X-rays and neutrons, the synchrotron sources have been developed without compromising on the advantages of neutron diffraction. Today, the progress of X-rays and thermal neutron radiation sources makes it possible to use diffraction experiment radiations with λ up to 10 Å, and the development of the technology to obtain crystals with "pre-established inter-lattice" distances assures the conditions to extract monochromatic beams from the radiation emitted by the source. In their competition with X-rays, the neutrons have the huge advantage of being less absorbed by the matter in comparison with X-rays, which allow them to be used in the investigation of not only volume effects but also surface effects. In the case of neutrons, there are two ways of interaction with condensed matter, with the nuclei or with the atomic magnetic moments of the investigated material. Over the years, several methods were developed to investigate the partial order of analyzed systems. Among these methods, the technique of small angle neutron scattering is the most valuable. Technically speaking, the term "small angle scattering" (SAS) does not refer always to small diffraction angles but to small values of the quantity Q which is the scattering vector, $\vec{Q} = \vec{k} - \vec{k}_0$, where $\vec{k}_0$ and $\vec{k}$ are the wave vectors of the incident and scattered radiations. For elastic scattering $Q = (4\pi/\lambda)\sin\theta$, where θ is half of the

scattering angle and λ is the radiation wavelength. In the angular range of SAS, the interested intensity is produced by inhomogeneities extended from 10 to 1000 Å. The quantity D of these inhomogeneities determines the most interesting angular range [3]:

$$\frac{1}{D} < Q < \frac{10}{D}$$

There are many processes that lead to scattering length variations, extended to zones up to 100 Å. Among these, there are the processes in solid phase namely aging, precipitating processes in solid phase, repeated thermal shock, neutron irradiation, the processes in mixed systems, for example the catalysts, where the two coexisting solid crystalline components are of enormous interest, as well as the ferofluids or the polymers in which neither one component is crystalline. The application of SAXS and SANS to material science has its origin from the experiments performed by Guinier in 1938, to study different types of aluminum alloys with various components such as Al–Cu and Al–Ag. He proved the existence of extremely small precipitate zones (so-called Guinier–Preston (GP) zones) as the first step in solidification of the precipitate of these alloys [3]. The GP zones represent submicroscopic regions of the matrix in which are produced a concentration of the initial solvate element. From one point of view, the GP zones could be considered as pre-precipitates because their formation represents a preliminary stage of precipitations set up from ultra-saturated matrix, but from another point of view it could be considered "clusters," in the sense that represent preferential associations of atoms.

In Al–Cu alloys, it has a diameter of about 80 Å and a thickness of 3–6 Å. With an average composition of 90% Cu, it comes out that the GP zones in these alloys are predominant constituted from Cu atoms. The physical nature and structural characteristics of the formed precipitates are dependent on temperature and heating duration because the precipitates are formed by germination and growing up processes, based on diffusion phenomena. The most important modification of alloy proprieties occur in the initial stages of the aging, with low temperatures and short heating durations when microstructural transformations are to a scale size under the resolution limit of optical microscopy (submicron precipitates). All these phenomena could be emphasized by SAXS and SANS methods. Regrouping of various atoms species during the precipitation process modifies the dispersion strength of X-rays or neutrons in different zones of aged alloy, due to the existence of an important density difference between the precipitated zones and the rest of alloy matrix. Among the structural processes produced through thermal treatment, which is applied to solid crystalline materials, the spinodal transition is something special [3]. The first phases of coherent precipitation took place through phase separation inside the crystalline lattice. Phase separation could start only through a nucleation process followed by nuclei growing. The germination of a new phase in a solid solution needs that in some regions the solid solution should considerably modify its composition. To be transformed into stable germs, these regions should have a specific dimension (about 10 Å). In these conditions, the interface between the germ and the solid solution (matrix) shows a distinct structural discontinuity, and therefore it has a free positive energy which

inhibits the germination. This germination difficulty is more evident in spinodal decomposition. In this case, the matrix regions, where the composition is modified, became more extended than classical germs and are named clusters. The interface between the matrix and the regions with modified composition became diffusive and does not present anymore a distinct structural discontinuity characterized by a positive free energy. To produce regions with modified composition, extended on large volumes, long-range composition fluctuations are necessary that would tend to decompose the original solid solution. The probability of these long-range composition fluctuations is much more increased when the temperature of original solid solution is situated close to the alloy "spinodal temperature." Above the spinodal temperature T_s (where the second derivative of the Gibbs free energy for the solid solution is positive), the supersaturated solid solution is metastable. Below the T_s spinodal temperature, the second derivative of the Gibbs free energy is negative, resulting in an unstable solid solution, which separates immediately by spinodal decomposition. Concentration fluctuations of spinodal transition are detected by their geometrical parameter values, in SAS methods structural observation domain. By these methods, it can be defined as a wavelength λ_c and obviously its reciprocal $Q = 2\pi/\lambda_c$ that depend on different factors as temperature difference $(T_s - T)$ or energy gradient. Cahn provided a quantitative description of the primary phase's kinetics of spinodal decomposition, in his linear approximation theory. In accordance with this theory, the growing rate has a maximum for the wavelength $\lambda_m = 2^{1/2}\lambda_c$. Thus both wave vectors Q_c and Q_m can be experimentally deduced by SAS because the intensity $I(Q)$ is proportional with the amplitude square of the suitable concentration waves. SAS methods provide quantitative information not only about particle dimensions but also about volume fraction of the second phase as well as metastable mixture limits. Therefore, the idea of using SANS as a nondestructive testing method for the industry came to reality. Because neutron absorption in the substance is very low, machine components of relatively large thickness can be easily investigated by SANS. The initial steps in this direction began in Italy by a research group from Fiat Corporation. They built a cold neutron source for different material studies. They began in 1974 when Pizzi and coworkers performed several tests on various materials used in machine components and spare parts [3]. For example, they tested the palettes of a turbine that works for a very long time in a power plant. The base material was a Ni alloy, with the particle dimensions between 200 and 300 Å, which confer some mechanical properties to that alloy. After 16,000 of hours working time, they noticed a radial growth of the constituent particles, in the middle and top of the palettes, reaching 900 Å when the breaking occurred after approximately 60,000 working hours. Similar effects were observed in the aviation turbine palettes, where the heavy working conditions affected the particles situated mostly in the middle of the palettes. Other tests were carried out on different machine parts built of heterogeneous materials subject to cyclic deformations or having areas affected by strong heating (welding zones). The conclusion was that any change in the dimension of constituent particles (up to 1000 Å) could be easily observed using the SANS technique. Another field of SAS applicability is the study of flows (voids) appearing in some materials irradiated with neutrons [3]. The components of nuclear reactors are subject to massive exposure to high rapid neutron fluxes, therefore resulting in the necessity of the determination and study of defects that might appear in those materials, having effects on the modification of initial proprieties.

The stress yielding of the material is correlated with the occurrence of a high concentration of micropores having a diameter between 200 and 1000 Å. Pores having smaller dimensions (≤ 25 Å) are usually present in a very large number and influence the material density. The intermediary sized pores give the gas permeability and the stability to irradiation of the covering layers. All these become visible by SAS technique utilization. SANS is a very useful instrument in the study of microscopic distribution of the magnetic field and the static interaction of spins from different magnetic system as well. Magnetic scattering is caused by the interaction between the neutron magnetic moment and the local magnetization of the sample. If this occurs at a small Q, it will show the magnetization fluctuations adequate for large distances in the studied sample and also the magnetic periodicities extended on large distances.

Another important field of study is offered by complex disordered materials such as ceramics, clays, cement, or glasses. Among these, the importance of cement in modern society cannot be underestimated. Cement is found in concrete structures everywhere such as buildings, roads, bridges, dams, and even for conditioning radioactive wastes. There is no escape from the impact of cement in our everyday life. Due to its great importance in the following, we will point only on its applications. Cement, as it is commonly known, is a mixture of compounds made by burning limestone and clay together at very high temperatures ranging from 1400 to 1600°C. Water is the key ingredient, which when mixed with cement forms a paste that evolves as a hard product. The water causes the hardening of the cement by a process called hydration. Hydration is a chemical reaction in which the major compounds in cement form chemical bonds with water molecules to yield hydrates or hydration products.

The heterogeneous nature and chemical complexity of the cement make the characterization of this system difficult. In spite of the inherent difficulties of the system, considerable understanding of the nature of cement and concrete has been obtained through the use of a wide variety of tools.

Studies of the cement pore liquid as a function of time, X-ray diffraction investigations, electron microscope, and NMR experiments have all contributed to a better understanding of the behavior of this material.

The greater penetrating power of neutrons (in comparison to X-rays), the opportunities for in situ measurement of hydrating pastes, the ability to use very long wavelength incident neutrons and the unique opportunities to change contrast offered by D_2O–H_2O exchange make SANS attractive as a means to probe the internal microstructure of cement pastes. The issue to be resolved, however, is the interpretation of the small angle scattering data. While the actual measurements are generally straightforward, the complexity of phases, contrasts, object morphologies, and size ranges forms a barrier to simple interpretations.

Small angle neutron scattering was first used to study the microstructure of cements in the early 1980s by Allen and coworkers [4]. They measured the small angle neutron scattering from a set of cement specimens hydrated at different water to cement ratios. They also examined the effect of soaking the specimen in heavy water and the change in SANS obtained when the specimen was dried. In their analysis of the SANS data, they assumed a simplified

model of the cement hydration reactions. In this model, the hydrated compounds C_6AFH_{12}, C_4AH_{13}, C_3ACSH_{12}, and $C_3S_2H_{2.5}$ and the hydroxides $Mg(OH)_2$, $Ca(OH)_2$, $NaOH$, and KOH in appropriate amounts were the products of cement hydration. Each of these compounds represented a different volume fraction of the cement paste. The strength of the SANS signal from the specimen in the small Q Guinier region was directly proportional to the square of the scattering length density difference (the contrast, see Equation 18) and to the total volume of the scattering particles. If the scattering in the two-phase model is to be interpreted as between the matrix $C_3S_2H_{2.5}$ and pores in the $C_3S_2H_{2.5}$ gel, it matters whether the pores are filled with light water, heavy water, or with air. The contrast between $C_3S_2H_{2.5}$ and water will vanish where the scattering length density curves intersect, at approximately 60% D_2O. If SANS data from cement paste are to be interpreted on the basis of a two-phase model, one issue is the identification of the appropriate phases. While the contrast is proportional to the SANS intensity, the detailed shape of the SANS curves will depend on the size distribution and shape of the scattering objects.

The SANS is presumed to be caused by a size distribution of objects of a known shape. To calculate the form factor for objects of known shape we can use Equation 17.

The parameters describing the object and its size distribution are then varied to minimize the difference between the calculated scattering and the data. Spheres, cylinders, and disks were considered by Allen and coworkers, and it was ultimately concluded that the SANS from their cement paste specimens was created by a distribution of water-filled spherical pores approximately 5 nm in diameter and a smaller component of pores with diameters of about 10 nm. SANS from the specimen that had been dried and not rewetted was interpreted as the one due to scattering from a much broader distribution of pore sizes with a peak of about 5 nm but extending to much larger diameters.

SANS from the specimens immersed in D_2O showed that the heavy water rapidly exchanged with the water in the pores and with the water in the surrounding C–S–H gel. The total porosity was of the order 1% of the volume.

All these are only a few examples that illustrate the large field of SAS application, where the immediate observation of the phenomena produced in materials lead to solving many practical problems and to extend the theoretical knowledge as well.

2. Physical principle of SANS

SANS is a method used to obtain information regarding the shape, dimensions, and internal configuration of the zones with scattering density significantly different from the average value, having relatively small dimensions (up to 1000 Å), unevenly distributed in some environment, where the distance arrangement is present or not. In a considered sample, all scattering centers participate in the scattering process. The scattering centers could be atoms, molecules, or particles of the analyzed system. System response could be a spatial distribution of scattered radiation reducible to a succession of maximums, determined by the existence of

distance arrangement in a material, or a succession of overlapping maximums over a continuous distribution when the distance arrangement is accompanied by disordered processes, such as amorphization, precipitation in solid phase, flaws, etc., or by a continuous distribution which present one or two isolated maximums like in the case of liquids (in this case the maximum is owed to the next close vicinity of each scattering center) or a continuous curve in case of SANS. Because X-ray scattering is similar to neutron scattering, in the following presentation I will start with the theoretical principles of SAXS accordingly adapted for SANS. It is well known that a diffraction image of a sample could be easily described in terms of reciprocal space or Fourier space [1]. If we consider $\rho(\vec{x})$ as the electronic density of the scattering body in a point defined by the vector $\vec{x}$, then $A(\vec{Q})$ is defined as the transform of $\rho(\vec{x})$ in the point defined by the vector $\vec{Q}$ in the reciprocal space, and it is given by

$$A\left(\vec{Q}\right) = \int \rho\left(\vec{x}\right) \exp\left(-i\vec{Q} \cdot \vec{x}\right) d\vec{x} \tag{1}$$

The X-ray diffraction theory is based on the fact that $A(\vec{Q})$ represents the amplitude of scattered radiation when $\vec{Q}$ is defined as

$$\vec{Q} = \left(\frac{2\pi}{\lambda}\right)\left(\vec{s} - \vec{s}_0\right) \tag{2}$$

where λ is the wavelength of the radiation, $\vec{s}_0$ and $\vec{s}$ are the unit vectors on the incident radiation direction and scattered radiation direction, respectively. The magnitude of $\vec{Q}$ is equal to $(4\pi/\lambda)\sin\theta$, where $2\theta = \theta_s$ is the scattering angle (the angle between incident ray and scattered ray). Therefore, very small scattering angles correspond to small values of the Q quantity. Analyzing Equation (1), we find that the intensity of the scattered radiation observed for a specific value of $\vec{Q}$ is equal to the square value of $A(\vec{Q})$, where $A(\vec{Q})$ is the suitable component of $\vec{Q}$ in the Fourier serial development of $\rho(\vec{x})$. For small values of Q that are produced at very small angles, the terms in $\rho(\vec{x})$ that define the quantity $A(\vec{Q})$ give a periodicity of $x = 2\pi/Q$, which is large enough in comparison with X-ray wavelength. These general considerations show that the very small diffraction angle (smaller than a few degrees) provides information on the structure of the matter to a relatively large scale in comparison with X-ray wavelength. It was experimentally observed that some samples generate a continuous and intense scattering at angles under 2°, without producing the normal diffraction effects from the usual X-ray experiments. This was first time noticed in specific types of fine carbon, black carbon powders, and different types of other substances, all having in common the fine particles of submicroscopic sizes. Later, it was concluded that continuous scattering around the direct beam is owed to the existence of the matter composed of small particles or, more general, to the existence of heterogeneities in the analyzed substance that can have dimensions from a few tens to a few hundred times the wavelength of the X-ray. The qualitative description of the central scattering, due to the presence of very small particles, could be done by analogy with the well-known light diffraction phenomena, which lead to the appearance of a halo when the light ray traverses a powder with grains having the dimensions 10 times larger than the wavelength of the light radiation.

Let us consider a particle bathed in an X-ray beam; thus all the electrons are wave scattering sources. If the scattering direction is the same as the incident ray, we can say that the scattered rays are all in phase and, if the scattering angle increases, the phase difference between the different scattered waves will also increase. Therefore, the amplitude of the resulting scattered wave will have values bigger or smaller in accordance only with the existing phase differences. This happens for a scattering angle about $2\theta = \lambda/D$, D being the average size of the particle, proving in this way that the study of central scattering offers a method to obtain the particle dimensions. This method is applicable only to the particles with dimensions between some specific limits. If D is too big, the scattering is limited to angles so small that are experimentally inaccessible. If D is too small, of the order of a few wavelengths, the scattering is too broad and too weak to be observed. To show more precisely which factors depend on the small angle scattering, let us consider a small particle of electronic density $\rho(\vec{x})$. Let us define a form factor $s(\vec{x})$ of this particle, which has a value of 1 when $\vec{x}$ vector is inside the particle, and a value of 0 when $\vec{x}$ is outside the particle. Thus, according to Equation (1), the amplitude of the scattered radiation from this particle will be

$$A_1\left(\vec{Q}\right) = \int \rho(\vec{x}) s(\vec{x}) \exp\left(-i\vec{Q}\cdot\vec{x}\right) d\vec{x} \tag{3}$$

If $A(\vec{Q})$ and $S(\vec{Q})$ are the Fourier transforms of $\rho(\vec{x})$ and $s(\vec{x})$, respectively, then

$$A_1\left(\vec{Q}\right) = A\left(\vec{Q}\right)\cdot S\left(\vec{Q}\right) \tag{4}$$

This can be demonstrated in the following manner. Let us consider the functions

$$a(\vec{x}) = \rho(\vec{x}) * s(\vec{x}) \text{ and } a(\vec{x}) = \int \rho(\vec{y})\cdot s(\vec{x}-\vec{y}) dv_y$$

Thus, the Fourier transform of $a(\vec{x})$ is $A_1(\vec{Q})$;hence

$$A_1\left(\vec{Q}\right) = \int a(\vec{x})\exp\left(2\pi i\vec{Q}\cdot\vec{x}\right) dv_x = \iint \rho(\vec{y}) s(\vec{x}-\vec{y})\exp\left(2\pi i\vec{Q}\cdot\vec{x}\right) dv_x dv_y$$

Using the notations $Y = y$, $Z = x - y$

we replace the elementary differentials $dv_x dv_y$ with $dv_Y dv_Z$ and to obtain

$$
\begin{aligned}
A_1\left(\vec{Q}\right) &= \iint \rho(\vec{y}) s(\vec{Z})\exp\left[2\pi i\vec{Q}\cdot(\vec{Y}+\vec{Z})\right] dv_Y dv_Z = \\
&= \int \rho(\vec{Y})\exp\left(2\pi i\vec{Q}\cdot\vec{Y}\right) dv_Y \cdot \int s(\vec{Z})\exp\left(2\pi i\vec{Q}\cdot\vec{Z}\right) dv_Z = A\left(\vec{Q}\right)\cdot S\left(\vec{Q}\right) \\
A_1\left(\vec{Q}\right) &= A\left(\vec{Q}\right)\cdot S\left(\vec{Q}\right)
\end{aligned}
$$

Giving the dimensions of the region where $s(\vec{x})$ is different from zero, its transform $S(\vec{Q})$ is completely determinated and, if the particle has dimensions from some few tens to a few hundreds of atomic diameters, $S(\vec{Q})$ will be different from zero only for very small values of $\vec{Q}$. Now, let us consider the function $A(\vec{Q})$. If we suppose that the sample has a constant electronic density $\rho(\vec{x})=k$, then the transform $A(\vec{Q})$ will behave like a Dirac delta function, being zero overall with the exception of the point $\vec{Q}=0$, where it is infinite and $\int \delta(\vec{x})d\vec{x}=1$. We can conclude that small angle scattering is the method to study the dimensions of the system constituent particles, but the supposition of the existence of the identical particles separated by long distances between them is not quite accurate in the case of real samples. Therefore, the generalization of the theory is needed to take into consideration the diversity of particle sizes and shapes as well as the effect of particle close packing. Without considering the particles, a mathematical expression should be obtained for the scattered intensity in the vicinity of the center that should take into account the electronic density in all the points of the sample. Further, we will discuss only the process of single scattering, neglecting the multiple scattering phenomena and Compton scattering. We will consider an X-ray beam, sufficiently large to irradiate a large number of particles, but narrow enough in comparison with the sample-detector distance, to be like a ray in the experimental device geometry. The amplitude of scattered radiation from the P_n point (Fig. 2) will depend on the scattering factor u_n and the direction defined by the unit vector $\vec{s}$

$$A_n = A_e u_n \exp\left[-i\frac{2\pi}{\lambda}\left(\vec{s} - \vec{s}_0\right) \cdot \left(\overrightarrow{OP_n}\right) \right] \tag{5}$$

where A_e is the amplitude scattered by a single electron in the same conditions, O is an arbitrary origin that serves to describe the pathway difference between different rays, and $\vec{s}_0$ is the unit vector defining the incident radiation direction.
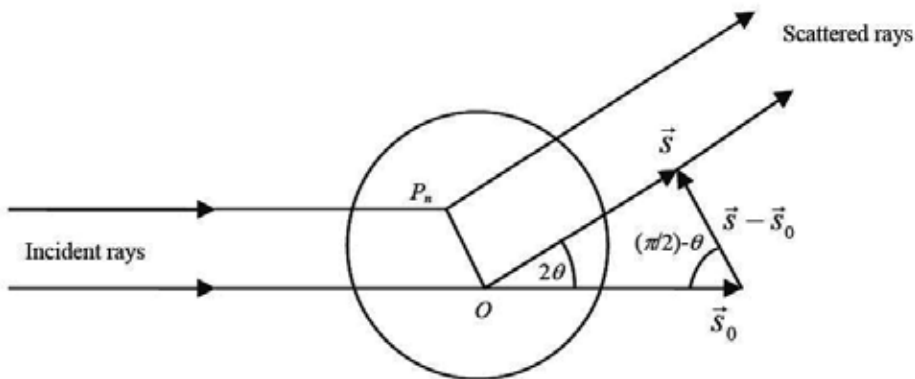
Figure 2. Diffraction by a scattering body.

The total amplitude of scattered radiation will then be

$$A(\vec{Q}) = \sum_n A_n = A_e(\vec{Q}) \sum_n u_n \exp\left(-i\vec{Q} \cdot \overrightarrow{OP_n}\right) \tag{6}$$

and the scattered intensity, the product between the amplitude A, and its complex conjugate A^*, will be

$$I(\vec{Q}) = \left|A_e(\vec{Q})\right|^2 \sum_n \sum_j u_n u_j \exp\left[-i\vec{Q} \cdot \left(\overrightarrow{OP_n} - \overrightarrow{OP_j}\right)\right] \tag{7}$$

The intensity scattered by an electron is

$$I_e(Q) = A_e^2(Q) = A_0^2 \frac{e^4}{m^2 c^4} \cdot \frac{1}{r^2} \sin 2\theta = I_0 \frac{e^4}{m^2 c^4} \cdot \frac{1}{r^2} \sin 2\theta \tag{8}$$

which is a three-variable function, the incident intensity, the scattering angle, and the distance of observation; I_0 is the intensity of incident beam; and r is the distance from the particle to detector. If the analyzed environment has a center of symmetry, and this center is placed in the origin O, then to each $\overrightarrow{OP_n}$ vector will correspond another vector $-\overrightarrow{OP_n}$. Thus, we will obtain a simplified expression for the scattered amplitude:

$$A(\vec{Q}) = \sum_n A_n = A_e(\vec{Q}) \sum_n u_n \cos\left(\vec{Q} \cdot \overrightarrow{OP_n}\right) \tag{9}$$

We define the structure factor of the environment as the report between the total scattered amplitude and the radiation amplitude scattered by a single electron in the same conditions:

$$F(\vec{Q}) = \frac{\sum_n A_n(\vec{Q})}{A_e(\vec{Q})} = \sum_n u_n \cos\left(\vec{Q} \cdot \overrightarrow{OP_n}\right) \tag{10}$$

The scattered intensity will then be

$$I(\vec{Q}) = I_e(\vec{Q})\left[\sum_n u_n \cos(\vec{Q} \cdot \overrightarrow{OP_n})\right]^2 = I_e(\vec{Q}) F^2(\vec{Q}) \tag{11}$$

The term "P_n point" was used to define the structure of a particle. If we consider a large particle, the base element in its description is the atom; in this case, the point P_n refers to the center of the nth atom, and the scattering factor u_n is the scattering factor of this nth atom. In the interested angular domain for SAS, $u_n(\vec{Q})$ can be considered as a constant equal to $u_n(0)$. If we

consider a small region, then P_n point refers to a small volume element that surrounds it. The scattering factor u_n is then equal to $\rho_n dv_n$, where ρ_n is the electronic density of the particle in the vicinity of P_n point, and dv_n is the volume of considered element. Generally, it is convenient to describe the particle structure taking into account enough small elements to consider the scattering factors of these elements to be constant, independent of scattering angle over the whole domain where the structure factor of the considered particle is different from zero. This theory of small angle X-ray scattering can be adapted very easily to neutrons.

Small angle neutron scattering is used where the X-rays cannot provide the desired information either of the lack of scattering contrast or of severe absorption of the studied material. The choice of thermal neutrons as a means of substance investigation was owed to their wavelengths and their energies corresponding to the inter atomic distances and excitation energies of condensed matter. Neutron absorption from the matter is very low, thus resulting in the samples that can have thicknesses larger than in the X-rays case which are strongly absorbed with an increase in the volume of analyzed samples. We can say that SANS allows the investigation of materials in various conditions, such as in containers, furnaces, cryostats, etc. Due to its magnetic moment, the neutron provides unique possibilities to the study of magnetic structures, magnetic moment distribution, and magnetic excitations. Being a nuclear propriety, the nuclear scattering amplitude can be considerably different between various isotopes of a specific chemical species. For example, the big difference between the coherent scattering lengths of hydrogen and deuterium lead to the usage of phase contrast in the study of hydrogenate materials, allowing a good resolution in analyzing polymers and biological substances in general. Because thermal neutrons interact very low with the matter, this interaction can be theoretically treated on the base of first Born approximation [5, 6]. We will show further that the variation of the scattering density is very important in the study of condensed matter through SANS. In the following, we will consider the "static approximation"; the scattering process is produced only at nuclear level on fixed targets letting those targets unchanged after the collision, and without considering the polarization effects.

Thus, we can write the coherent elastic scattering differential cross section on a single atom:

$$\frac{d\sigma}{d\Omega} = \frac{1}{N}\left|\sum_R b_R \exp\left(i\vec{Q}\cdot\vec{R}\right)\right|^2 \tag{12}$$

where N is the number of scattering nuclei exposed to the beam, and b_R is the coherent scattering length of the chemical species that occupy a specific place determined by the position vector $\vec{R}$. If we replace b_R through an average local scattering length density $\rho_b(\vec{r})$, where $\vec{r}$ is a continuously variable position vector, we can write

$$\frac{d\sigma}{d\Omega} = \frac{1}{N}\left|\int_V \rho_b(\vec{r})\exp\left(i\vec{Q}\cdot\vec{r}\right)d^3\vec{r}\right|^2 \tag{13}$$

where the integration is performed over the whole sample volume *V*.

The scattering length density $\rho_b(\vec{r})$ can now vary on distances of the order of $d_{\min}$, where $d_{\min} \cong \pi/Q_{\max}$, $Q_{\max}$ being the maximal value accessible by experiment. Thus, we can write that

$$\rho_b(\vec{r}) = \Delta\rho_b(\vec{r}) + \bar{\rho}_b \tag{14}$$

where ρ_b is averaged on volumes larger than the instrument resolution volume, determined by the minimum observed value of *Q*. Therefore, the cross section that contains the useful information about the studied system is dependent on $\Delta\rho_b(\vec{r})$. By substituting Equation (14) in Equation (13) we obtain

$$\frac{d\sigma}{d\Omega} = \frac{1}{N}\left|\int_V \left[\rho_b(\vec{r}) - \overline{\rho_b}\right]\exp(i\vec{Q}\cdot\vec{r})d^3\vec{r}\right|^2 \tag{15}$$

For a specific distribution of scattering length, the cross section can be analytically calculated with the help of Equations (13) and (15). Because the cross section values are not known everywhere in reciprocal space, $\rho_b(\vec{r})$ determination by experimental measurements of $d\Sigma/d\Omega$ values is very hard to be carried out, or even impossible. Let us take a sample containing N_p particles with scattering length densities $\rho_{bp} = b_p/v_{ap}$, where b_p is the scattering length averaged on the particle volume, and v_{ap} is the atomic volume from the particle. Let us consider that these particles are packed in a homogeneous matrix having scattering length densities $\rho_{bm} = b_m/v_{am}$.

Using Equation (13) we obtain

$$\frac{d\Sigma}{d\Omega}(\vec{Q}) = \frac{1}{N}\left(\rho_{bp} - \rho_{bm}\right)^2 \left|\int_{V_t} \exp(i\vec{Q}\cdot\vec{r})d^3\vec{r}\right|^2 \tag{16}$$

where the integral is extended over the volume V_t occupied by all the particles. In the most general case, this integral will contain spatial and orientation correlation elements between particles, and effects owed to the size distribution of the particles. Taking into account the form factor expression for a single particle

$$F_p(\vec{Q}) = \frac{1}{V_p}\int_{V_p} \exp(i\vec{Q}\cdot\vec{r})d^3\vec{r} \tag{17}$$

where V_p is the particle volume so that $\left|F_p(0)\right|^2 = 1$. We will now consider N_p identical particles for which we can write the following expression

$$\frac{d\Sigma}{d\Omega}(\vec{Q}) = \frac{V_p^2 N_p}{N}\left(\rho_{bp} - \rho_{bm}\right)^2 \left|F_p(\vec{Q})\right|^2 \tag{18}$$

that is valid in the case of binary systems, without contributions from the interferences between particles.

The interference term from Equation (16) that was neglected in Equation (18) is the Fourier transform $\Psi(\vec{Q})$ of the correlation function:

$$\Psi\left(\vec{Q}\right) = \frac{1}{N_p} \sum_{i \neq j} \exp\left[i\vec{Q} \cdot (\vec{r}_{0i} - \vec{r}_{0j})\right]$$

(19)

where $\vec{r}_{0i}$ and $\vec{r}_{0j}$ are the position vectors of the particle centers denoted by i and j.

The $\Psi(\vec{Q})$ function will be zero for all the values of $\vec{Q} \neq 0$ if the distance distribution between the particles is completely random, approximately like in the case of very diluted systems. Equation (18) is valid for particles anisotropically oriented, but all are identically oriented. In most cases of random distribution of the orientations or in discrete but multiple orientations of anisotropic particles, suitable averages of $|F_p(\vec{Q})|^2$ are used. Guinier shows that at small values of Q, the scattering function $S(\vec{Q}) = |F(\vec{Q})|^2$ for a specific physical system can be written as

$$S\left(\vec{Q}\right) = \exp\left(-Q^2 R_D^2\right)$$

(20)

where R_D means the gyration radius which is a material parameter having the length dimension defined through

$$R_D^2 = \frac{1}{V_p} \int_{V_p} r_D^2 q\left(r_D\right) dr_D$$

(21)

where $q(r_D)$ is the geometrical cross section of the particle, through the length of a plane normal to a direction D and at a distance r_D from the origin inside the particle. For a system of particles randomly oriented

$$S\left(\vec{Q}\right) = \exp\left(-Q^2 R_G^2 / 3\right)$$

(22)

with

$$R_G^2 = \frac{1}{V_p} \int_{V_p} r^2 d^3\vec{r}$$

(23)

For spheres of radius R_S, $R_G = (3/5)^{1/2}R_S$, and Equation (21) coincides with the expression

$$S_s\left(QR_s\right) = \left[3\left(\sin\left(QR_s\right) - QR_s\cos\left(QR_s\right)/Q^3R_s^{\;3}\right)\right]^2$$

to the term proportional with Q^4. The subsequent terms in the developments of the two series are in a good concordance, but the corresponding terms have the same sign. Guinier approximation is thus accepted over a large range of QR_G (<1.2).

For rotational ellipsoids, the Guinier approximation coincides with the extension of scattering functions until Q^6. For other shapes of the particles, it might be necessary for an investigation of the small values of Q to be able to determine R_G with sufficient accuracy. In the case of homogeneous particles, with pronounced margins and area A_p, Porod has proved that

$$\overline{S\left(\vec{Q}\right)} \cong 2\pi A_p / V_p^2 Q^4 \tag{24}$$

This shows the average decrease in the scattering function at large Q. Q should be larger than the reciprocal value of the smallest dimension of the particle.

3. Experimental methods used in the study of condensed matter by SANS

The goal of SANS method is to measure $I(Q)$ and to extract from that measurement the "structural" data regarding the studied system. The quantity Q is defined as $Q = \dfrac{4\pi\sin\theta_s}{\lambda} \approx \dfrac{2\pi}{\lambda}\theta$, if $\theta = \dfrac{\theta_s}{2}$ is small enough.

Therefore, to measure $I(Q)$, it is sufficient to measure $I(\theta)$ at constant λ or $I(\lambda)$ at constant θ. In the following, we will discuss both experimental alternatives.

3.1. The method $I(\theta)$ at constant λ

This method is based on monochromatic (λ = constant) beam extraction from the white thermal neutron spectrum provided by a research reactor. The thermal neutrons released from the reactor are first collimated with a Soller collimator (with plane parallel slits) and after that they are monochromatized with either a mechanical monochromator or a crystal. Monochromatization is the method that allows the extraction of desired neutrons from the neutron beam provided by the source; in other words, to obtain thermal neutrons with energies in a very narrow interval centered around a value E_0 of the energy. Neutron monochromation is based either on their corpuscular proprieties (mechanical monochromators) or on their wave proprieties (crystal monochromator). The mechanical monochromator is a cylinder endowed with helicoidal slits on the whole length of its generatrix.

When the cylinder is rotating with the angular speed ω, the neutrons with their motion direction parallel with the rotor axis would traverse the monochromator slits without modifying their distance to the slits walls only if they would have a specific speed v_0, directly correlated with ω and which is corresponding to the wavelength λ_0 of the neutrons transmitted by the monochromator. Another type of mechanical monochromator uses disks instead of a cylinder. Its functional principle is identical with the cylindrical monochromator, but having the difference that the place of helicoidal slits is taken by straight slits cut off on a rigid mounted disc on a horizontal axis, which rotates with an angular speed ω. The disks are positioned on the axis having the slits displaced to provide a selective opening in accordance with the axis rotation speed ω, only to the neutrons moving with a specific speed v_0. Nevertheless, the most used monochromatization method is by using a crystal. Crystal utilization in spectrometer devices is based on the neutron diffraction phenomena.

Monochromatic neutron beam separation from the thermal neutron beam provided by the reactor is realized through its Bragg reflection on a monocrystal. If we note the distance between the crystalline planes with d_{hkl} determined by the h, k, l indexes, and θ_B the neutron incident angle on these planes, then the reflected neutron wavelength is given by the Bragg law

$$n\lambda = 2d_{hkl}\sin\theta_B = \frac{nh}{\sqrt{2mE}}$$

where m and E are the neutron mass and neutron energy, respectively, but n is the reflection order.

In other words, if a monocrystal is used to select neutrons with a specific wavelength λ that satisfies the Bragg relation, then the neutrons selected by the crystal would also have the wavelengths $\lambda/2$, $\lambda/3$, $\lambda/4$,..... etc., which means that reflections with a higher order take place, with n = 1, 2, 3,.... In the case of monochromators with crystal, the presence of high-order reflections could be a serious problem because sometimes, depending on the spectral distribution of the incident beam and the crystal structure factor, the reflection intensities become comparable and even greater than the first-order reflection intensity. In most neutron physics experiments, first-order reflection (n = 1) is used, but other reflections (high-order contaminations) should be eliminated by different means.

Analyzing the Bragg relation, we can see that by using of monochromator crystals, only monochromatic neutrons with the wavelength of $\lambda_{max} \leq 2d_{max}$ can be selected, where d_{max} is the maximum distance between the crystal planes. The neutrons having the wavelength $\lambda > 2d_{max}$ are not presenting Bragg reflections.

This observation suggests a simple way to eliminate the second-order reflections, utilized mostly when the monochromatic neutrons desired to be extracted from the reactor emergent beam have wavelengths relatively large, for example, in the range $\lambda > 6$ Å. It is sufficient to introduce a polycrystalline filter of convenient size in the pathway of neutron beam falling on the monochromator crystal, with its crystalline structure characterized by $d_{max} < \lambda_0/2$, where λ_0

is the wavelength of the neutrons to be extracted. There is another experimental solution to eliminate second-order reflections, for example, using a monochromator of special monocrystals with an internal composition that cancels the structural factor for some specific groups of crystalline indexes. Because the problem of high-order reflections is overpassing the goal of this chapter, we will not insist on this subject.

Frequently, the experimental pattern used to obtain monochromatic neutron beams in this way contains a Soller collimator which spatially delimitates the incident neutron beam coming out from the reactor, the monochromator crystal, and the second Soller collimator which delimitates the diffracted beam. Simultaneous rotations of the second collimator and the crystal with angular speeds staying in a ratio of 2:1 allows to extract monochromatic neutron beams of different wavelengths from the continuous spectrum of the incident thermal neutron beam. The monochromatic neutrons are recorded by a detector placed after the second collimator rotating in the same time with it.

The devices built on this principle, the so-called neutron spectrometer with crystal, allow the determination of total cross section by the measurement of sample transmission in accordance with neutron wavelength. To study the angular distribution of scattered neutrons by a certain target and implicitly to measure the differential cross sections, a pattern with a third Soller collimator between the sample and detector is used. To investigate the neutron scattering of different wavelengths, the whole system built from the second collimator, the studied sample, the third collimator, and the neutron detector should be rotated around the first fixed axis that is going through the middle of the monochromator crystal and together with it; the angular speed ratio of the crystal and the mentioned system should be 1/2. For a certain position of the monochromator crystal and the second collimator, the third collimator and the detector could be rotated around the second fixed axis (that is going through the middle of the sample) allowing the measurement of sample differential cross section for thermal neutrons having the wavelengths determined by the monochromator preceding the sample. This experimental pattern is named neutron spectrometer with two axes. Many experimental systems use optical patterns derived from the two axis spectrometer described earlier. Anticipating the discussion in the next section, we would mention that from the simple presentation of the optical pattern of considered spectrometer arises a specific limitation of its efficiency. Actually, to measure $I(Q)$ with sufficient precision in the optical pattern described before, it is necessary to increase the distances (R) between the studied sample and the detector, as much as possible; increasing this distance obviously will lead to decreasing the lower limit of the explored Q range. Because the intensity of the scattered beam varies with $1/R^2$, the obtained resolution gain is drastically affected by losing the luminosity of the experimental system. If we add to this inconvenience the construction of experimental devices having excessive dimensions, the continuous search for more efficient SANS optical patterns becomes explicable. One of the identified optical patterns which is considered most acceptable is by using two crystals, with the sample staying between them.

Two crystal systems were used as monochromators in spectrometric assemblies long time ago, first in X-ray physics and then in neutron physics. To discuss the utilization manner of two monocrystals systems in SANS, we have to reveal the optical characteristics of these systems.
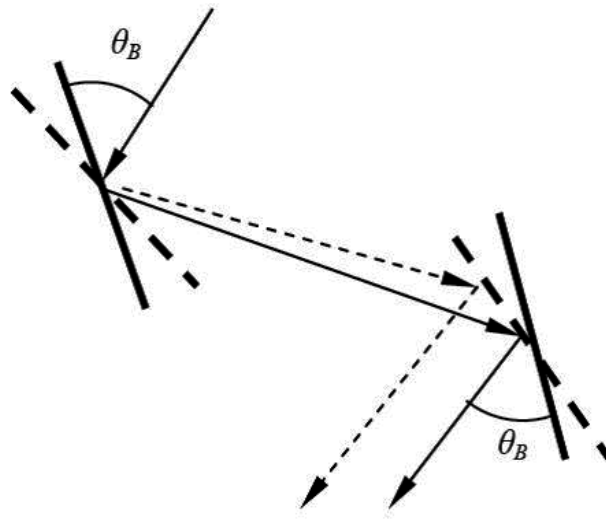
Figure 3. Parallel pattern.
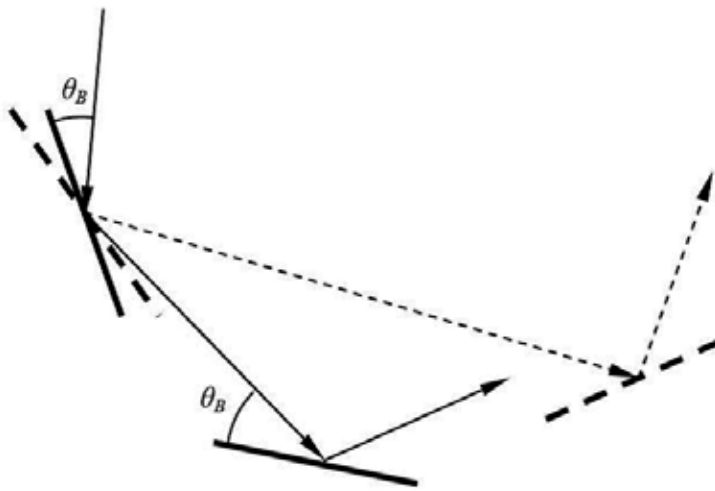
Figure 4. Antiparallel pattern.

To simplify the explanation, we will limit our case to consider that the two monocrystals are ideal identical crystals, from the point of view of their internal crystalline structure and their cutting method (has the same active reflecting planes). A two-monocrystal system could work in two optical patterns: parallel (Fig. 3) and antiparallel (Fig. 4).

In the parallel pattern, any selected wavelength from the incident polychromatic beam through Bragg reflection on the first crystal leads to the propagation of the double reflected beam in parallel direction with the incident beam. Therefore, this pattern is not dispersive (does not
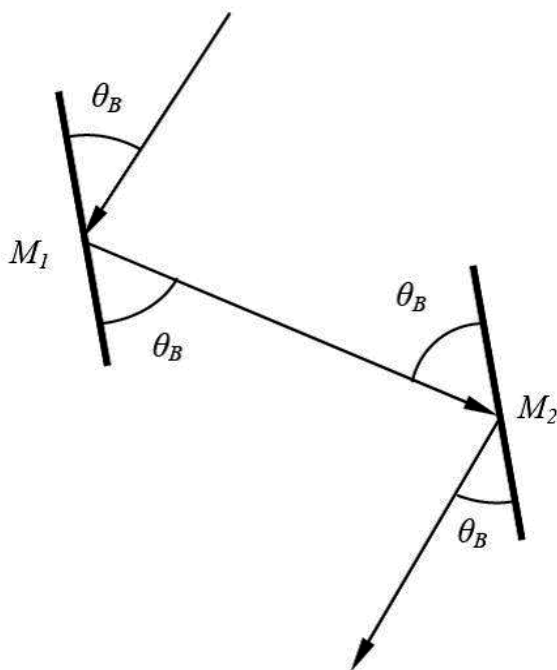
Figure 5. Double crystal parallel pattern.

spatially separate the beams of different wavelengths). In the second optical pattern, the Bragg double reflected beam is propagated on a direction oriented toward the region containing the radiation source and is named antiparallel. To notice that the wavelength change of the selected radiation beam through double reflection is realized along two directions depending on the wavelengths, revealing the dispersive feature of the antiparallel pattern. In the case of the parallel pattern, the thermal neutron beam falling on the first monochromator crystal under the incident angle θ_B, it will be Bragg reflected on the second crystal, the double reflected ray making the same angle θ_B with the second crystal (Fig. 5).

If a sample is interposed between the two crystals, then the beam reflected by the first crystal will be scattered by the sample under the θ_S angle and will fall on the second crystal under the θ incident angle (Fig. 6).

To detect the scattered beam, we have to rotate the second monochromator crystal together with the detector by an angle α; thus the Bragg relation is satisfied by obtaining the same incident θ_B angle for the sample scattered ray. Among these angles, we can write the following relations:

$$\theta - \alpha = \theta_B \Rightarrow \theta - \alpha = \theta_B$$
$$\theta_S + \theta_B = \theta \Rightarrow \theta - \theta_S = \theta_B \Rightarrow \alpha = \theta_S$$
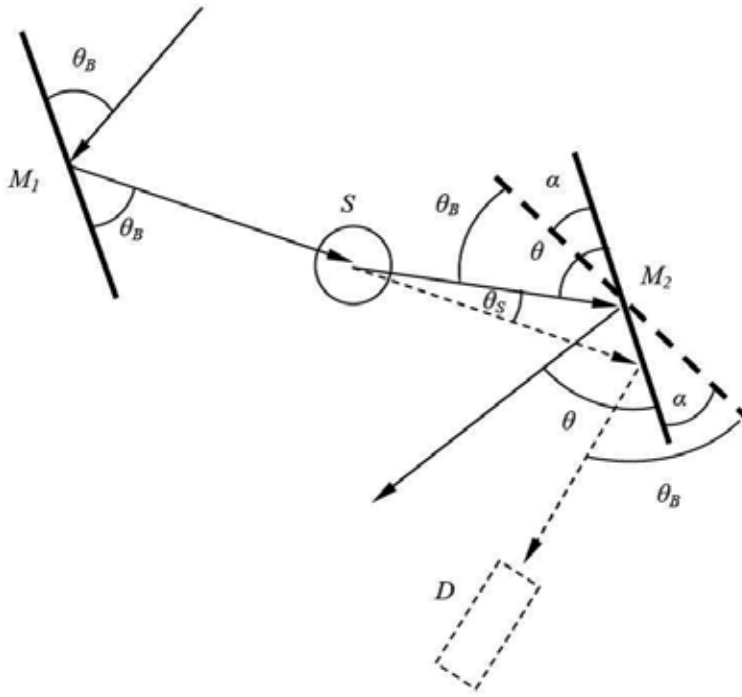
Figure 6. Three axes parallel pattern.

Because the sample is scattering, the neutrons under different angles $\theta_S(\theta_{S1}, \theta_{S2},..., \theta_{Sn})$ arise that the system composed from the second monochromator and the detector should be rotated in accordance with the suitable $\alpha(\alpha_1, \alpha_2,..., \alpha_n)$ angles to be able to detect all scattered neutrons. Let us now consider the case of the antiparallel pattern. The thermal neutron beam falls on the first monochromator crystal under the incident θ_B angle and is reflected on the second monochromator crystal, the double reflected ray leaving the system under the same θ_B angle (Fig. 7).

If we have a sample between the two crystals, then the reflected beam by the first crystal will be scattered by the sample under a θ_S angle and will fall on the second crystal under the θ angle (Fig. 8).

The neutrons scattered by the sample S could be detected only by rotating the second crystal with the α angle, thereby reestablishing the Bragg law by remaking the initial incident θ_B angle. Also, we found that

$$\theta + \alpha = \theta_B \Rightarrow \theta + \alpha = \theta_B$$
$$\theta_B - \theta_S = \theta \Rightarrow \theta + \theta_S = \theta_B \Rightarrow \alpha = \theta_S$$
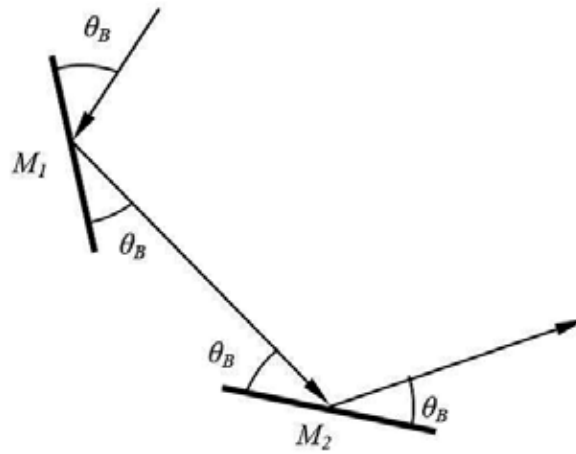
Figure 7. Double crystal antiparallel pattern.
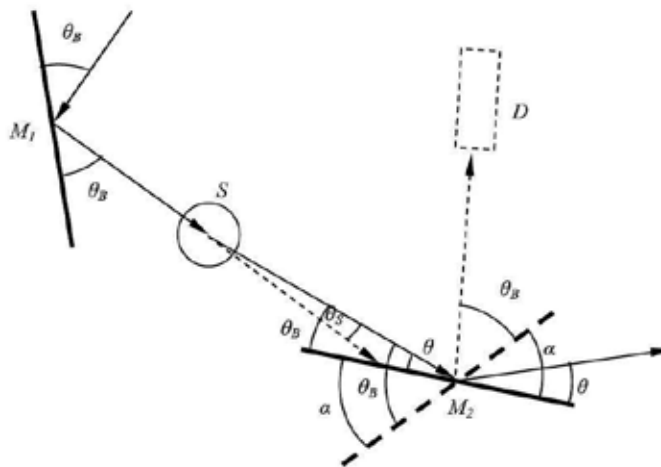
Figure 8. Three-axe antiparallel pattern.

To notice that this pattern is the most frequently used due to its dispersive feature this allows a better measurement of the interest neutrons.

3.2. The method $I(\lambda)$ at constant θ

Another method is to make the observation only on a certain scattering direction 2θ = constant. This time the directly measurable quantity is the wavelength (or the energy) of the coherent radiation scattered by the sample. This method is based on λ determination for every detected neutron, by its time of flight measurement along a known distance. According to the De Broglie equation

$$\lambda = \frac{h}{mv} = \frac{ht}{mL}$$

where L is the distance between the neutron source and detector, h is the Planck constant, and m is the neutron mass. The neutrons with a wavelength λ will have a speed $v = h/m\lambda$ so that to cover an L distance, the time $t = L/v$ will be necessary.

Neutrons of different wavelengths will need different time to cover the same distance L. If the moment of neutron pulse emission coincides with the time scale origin of the neutron detector impulse analyzer, the detector impulse selection in accordance with the impulse appearance time (practically by neutron arrival time) allows the spectral distribution measurement of the neutron beam. The electronic devices performing this selection are "the time of flight analyzers." The analyzer has a number of channels in which the impulses are accumulated due to the neutrons arriving to the detector in the time intervals $t_0 + \tau$, $t_0 + 2\tau$, $t_0 + 3\tau$, and so on.

Here, t_0 represents a "delay time" of the impulse temporally analyzer system start-up, which could be varied with the used experimental pattern particularities, and τ is the channel temporal width, a quantity that can be varied in stages for a specific instrument. The measurements by the time of flight method can be made using both steady-state reactors and pulsed reactors as neutron sources.

In the case of steady-state reactors, the neutron beam leaving the reactor channel meets an obturator in its way which opens the way only for very short time intervals. In this manner, the detector "notices" a pulsed neutron beam with a determined time length, for a specific obturator–detector distance, by the neutron energetic spectrum. The detector is connected with a time of flight analyzer, which can be unleashed by the obturator opening. To the pulsed reactors, the obturator function is undertaken by the neutron source itself. The time of flight analyzer start-up command is given by the neutron source when the pulse is accomplished. In every SANS experiment, the main goal is to determine with a good precision and in a reasonably short time the Q dependence of the analyzed sample coherent elastic scattering differential cross section in a large as possible Q variation range. From the point of view of the Q range explored value extension, the two SANS investigation methods indicate the following possible performances:

$$\frac{Q_{max}}{Q_{min}} = \left[\frac{\theta_{max}}{\theta_{min}} \right]_{\lambda = const.} \quad \text{and respective} \quad \frac{Q_{max}}{Q_{min}} = \left[\frac{\lambda_{min}}{\lambda_{max}} \right]_{\theta = const.}$$

For any $Q_{max} - Q_{min}$, the interest interval for a certain sample, the first method seems to be more reasonable because the Q limitation apparently is dictated only by the measurement conditions, but in the case of the second method, the λ limitation is dictated by the spectral characteristics of the neutron source. If the neutron source is in steady state, then the first method utilization is certainly more advantageous because pulsing the neutron beam with a chopper leads to a usage of 10^{-4}–10^{-3} from the produced neutrons even if we consider the advantage of

the second method to replace the sequential measurement of $I(Q)$ with the simultaneous one. The advantage of the first method toward the second in the case of utilization of a steady-state source is more evident if we estimate the consequences resulting in the obtained precisions and the experiment duration from the efficient utilization of the neutron beam emitted by the source. In the case of pulsed sources, the same criteria of neutron beam efficient utilization impose the application of the second working method. The approximate equivalence of the two methods, the first by the steady-state reactors and the second the pulsed sources, can be motivated that in present, at realized impulse fluxes and obtained pulses frequencies, the pulsed sources lead to getting middle fluxes comparable with the one obtained from the steady-state reactors of the same category. All these reasons justify the topics discussed in the next section, the presentation of SANS equipment used by the first method at the steady-state reactors or the second method used at the pulsed sources.

4. Experimental patterns

4.1. The method $I(Q)$ at constant λ

As it was discussed in Section 3, from among the optical patterns, the one with two crystals and the sample situated between them is much more appreciated. This pattern was used in many reactors, and a typical description of it is given in Fig. 9.
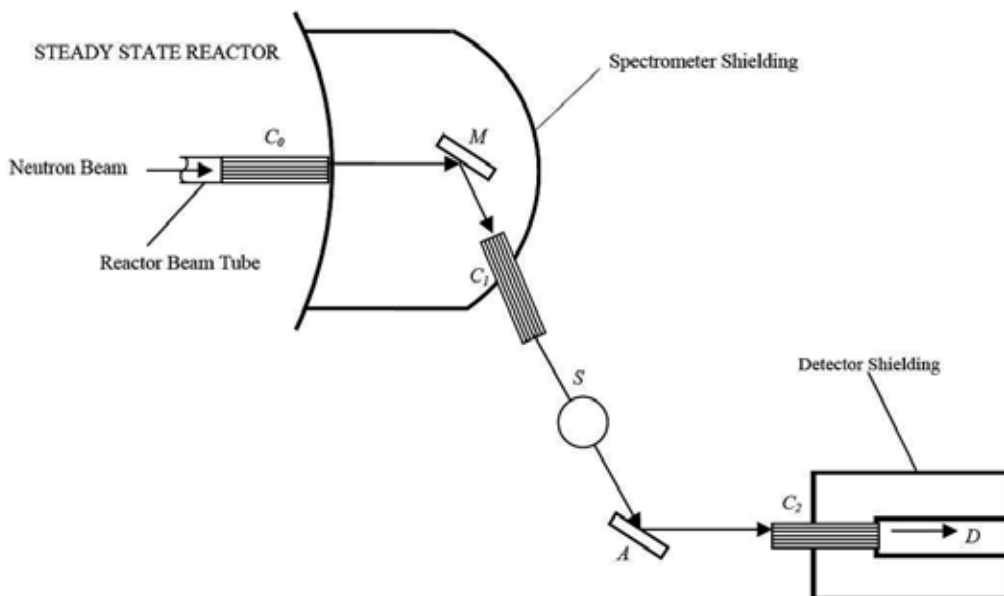
Figure 9. Three-axe spectrometer.

The monochromator group built by C_0 and C_1 collimators, and the monocrystal M sets up a monochromatic beam falling on the studied sample S. The analyzing group formed by the monocrystal A, the collimator C_2, and the detector D is initially tuned to detect the incident neutrons in the sample. To determine the neutron angular distribution produced by small angle scattering in the sample, we have to perform a combined scanning of the detector and the analyzer crystal around a vertical axis going through the center of the A crystal. Let us consider a small reactor providing a neutron flux of 1×10^{13} neutrons/cm²s at 2 MW maximal power. From the white thermal neutron flux transmitted through the C_0 collimator, the M monochromator selects a very narrow band centered around the $\lambda = 1.15$ Å, with a wavelength resolution of $\Delta\lambda/\lambda = 4.5 \times 10^{-3}$. This beam is transmitted further through the C_1 collimator to the analyzed S sample and scattered at small angles (between 0 and 2 minutes). The A crystal collects the scattered beam and transmits it to the D detector through the C_2 collimator.

We consider that both crystals are copper monocrystals identically cut, with the reflecting plane orientation in the (002) direction and a mosaic divergence structure of 14 minutes. The C_0 and C_1 collimators have an angular horizontal divergence of 10 minutes, while that of the C_2 collimator is only of 5 minutes. The 2θ monochromator angular range is 50° but the scattering range of monochromator and analyzer is maximum 120°. The detection system is an ordinary BF_3 detector. Another type of neutron spectrometer is by using a cold source to allow neutron moderation at low temperatures, such as the VVR-SM reactor from Budapest Neutron Center (BNC). With an active core providing an average power of 10 MW, the neutron balance is improved by the mean of a beryllium reflector up to 10^{14} neutrons/cm²s. The small angle scattering spectrometer described (Fig. 10) in the following is a conventional one. It uses a mechanical monochromator instead of a crystal monochromator. The mechanical selector with helical slits gives a wavelength resolution $\Delta\lambda/\lambda$ between 5 and 20% for a λ lying between 3.5 and 8 Å.

The neutron beam is geometrically built up by a 3 m-long vacuum collimator. The maximal beam dimension in the sample is 2 cm diameter. The distance from the sample to detector can vary from 1 to 5 m. The spectrometer is provided with an automatic sample changer controlled by a computer. The scattering vector range lies between 5×10^{-3} Å$^{-1} < Q < 2$ Å^{-1}. The scattered neutrons are detected by an XY positional detector with BF_3 having the dimension 64×64 cm².
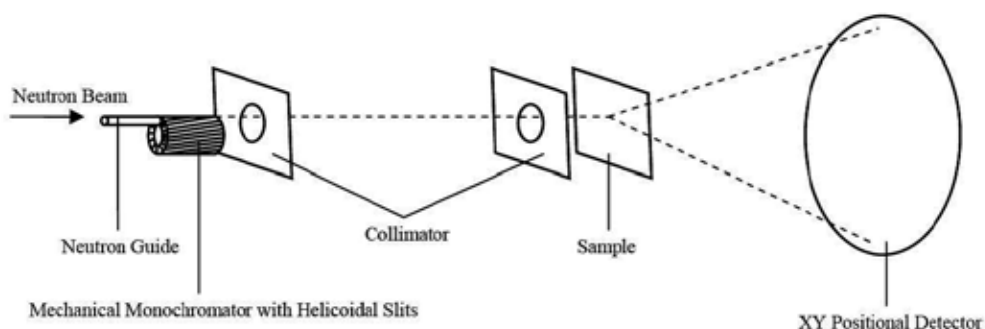
Figure 10. Spectrometer with mechanical monochromator.

Measurement instrument control and experimental data collection are performed by a computer.

4.2. The method $I(\lambda)$ at constant θ

This method is used mostly for the neutron pulsed sources. This type of spectrometer built on the time of flight principle is installed to the IBR-2 pulsed nuclear reactor at Joint Institute for Nuclear Research (JINR) in Dubna, Russian Federation. The name of the spectrometer is YuMo [7], given from its constructor, the scientist Yu. M. Ostanevich (Fig. 11). The reactor fuel is plutonium oxide, and uses liquid sodium as a coolant. The reactor reflector is composed of a static part and a rotational one with constructive and movement characteristics that determine the issue of fast neutron pulsed flux. The produced neutrons are moderated in water and through the horizontal beam tubes that surround the reactor active core in the experimental hall.

In the current working conditions, the reactor provides a maximum flux of thermal neutrons of 10^{16} neutrons/cm²s per pulse at the moderator surface. The frequency of pulse repetition is 5 Hz.
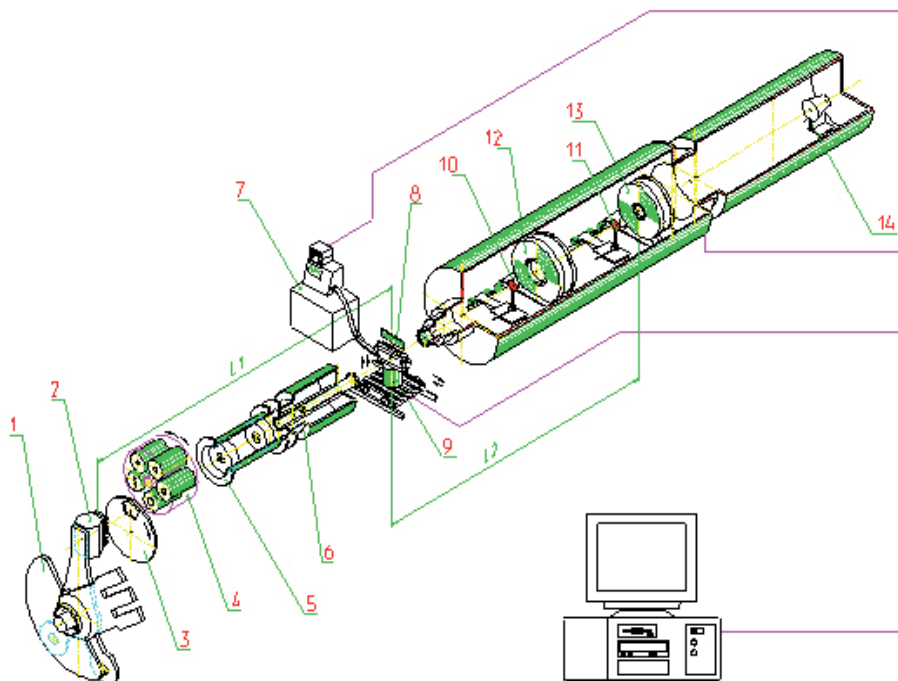
Figure 11. SANS spectrometer YuMo.1) two reflectors, 2) zone of reactor with moderator, 3) chopper, 4) first collimator (C1), 5) vacuum tube, 6) second collimator (C2), 7) thermostat, 8) samples table, 9) goniometer, 10)–11) vanadium standard, 12) ring-wire detector, 13) position-sensitive detector "Volga," 14) direct beam detector.

The chopper placed after the neutron moderator plays the main role to remove the neutrons from other reactor pulses and to assure that the neutrons from the interested pulse arrive at the detector. The neutron tube is made by steel pipes of different diameters and is kept under vacuum of about 10^{-2} Torr to avoid neutron absorption.

It is connected to the central vacuum system which is controlled from reactor control room and is provided with a mechanical beam stop that automatically closes the beam. A complete cycle of closing–opening the beam stop lasts about 6 minutes. The chopper is followed by a collimator with discrete variable aperture (C_1) that assures a geometrical pre-shape of the neutron beam and by the monitor whose signals are used for the normalization of the data obtained from different reactor pulses. The next collimator (C_2) assures the geometrical profile of the incident neutron beam in the sample and defines its dimensions. The collimator (C_1) is composed of four cylinders of different diameters (100 mm, 80 mm, 60 mm, and 40 mm), but with the same length which can be remote-controlled to be aligned in the neutron beam by a rotational movement in accordance with the experimental requirements of the beam geometrical pre-shape. The collimator (C_2) which limits the geometrical profile of the incident neutron beam in the sample has a remote-controlled variable opening (28 mm, 14 mm, and 7 mm). The holder with the collimation orifices of the (C_2) collimator are made from boron polyethylene having an insignificant scattering cross section in comparison with the absorption cross section. All collimators and the most important shielding elements are covered with a mixture of polyester and boron carbonate or boron acid. The sample holder having six slots is connected to a special remote-controlled mechanism of sample changing that allows each sample to be introduced in the neutron beam according to the experimental program. The sample is placed at 18.74 m from the moderator surface. The sample holder is provided with a cooling and warming system that allows adjusting the sample temperature between 20 to 150°C.

To record and analyze the scattered neutrons in accordance with their time of flight, the experimental equipment is provided with a measurement system having two detectors. The detectors are functionally identical but different by dimensions that assure their efficiency in observing the Q values at small and large ranges. Therefore, both detectors are provided with eight active ring detectors; one detector having the central opening of 80 mm while the second of 200 mm having outside diameters of 730 mm and 560 mm, respectively. Each detector can be settled in one of the eight positions having the sample detector distance fixed in the interval of 4.5 –12.5 m. The active part of each detector is divided into eight independent ring detectors by means of a concentric copper partition (the cathodes); at the center of each ring exists a tungsten wire of 25 μm thickness (the anode). This type of assembly provides eight independent ring detectors that offer more accuracy of the measurements by partial overlapping of the detection range of each ring with the range of the previous ring. The detector efficiency for neutrons with $\lambda = 1.8$Å is about 70%.

The detector room is located after the samples and is made from a steel pipe of 1200 mm diameter and 12 m length having the inside surface covered with a cadmium layer of 0.5 mm thickness. Inside the room are mounted two rails for the movement of the electric-driven detectors trucks. The incident neutron beam is transmitted through the central hole of the detectors. At a distance of about 1.5 m from the reactor side, the detector is placed on a truck-

driven mechanism in the vanadium standard (a vanadium metal sheet of about 0.3 mm thickness) that allows the introduction of the beam according to a program. This standard is used for the obtained experimental data calibration. The incident beam detector placed after the annular detectors measures the spectral distribution of the incident neutrons in the sample and forwards the normalization to this spectra of the scattered neutron spectra.

5. Conclusions

To summarize, we can say that small angle scattering is the collective name given to the techniques of SANS and SAXS scattering. In each of these techniques, radiation is elastically scattered by a sample, and the resulting scattering pattern is analyzed to provide information on the size, shape, and orientation of some components of the sample. They offer the possibility to analyze particles without disturbing their natural environment. The type of sample that can be studied by SAS, the sample environment that can be applied, the actual length scales that can be probed, and the information that can ultimately be obtained all depend on the nature of the radiation used. For example, SAXS cannot be used to study thick samples or samples requiring complex containers, while SANS can penetrate deeper in the condensed matter. SANS is produced by heterogeneities in matter. If these are randomly oriented, every atom pair contributes to the scattering of a sample. Inhomogeneities of sizes larger than atomic distances (10–1000 Å) produce scattering patterns with Q ranges $1/D < Q < 10/D$, if D is the dimension of the inhomogeneities.

A scattering experiment sees a scattering length density; in the case of X-rays, this is simply the electron density. The absolute density is not important but, in contrast, the difference between the particle and the surrounding medium.

The result of the experiment is the Fourier transformation of the contrast distribution. By comparing the experimental data with the theoretically calculated intensities or by a Fourier back transformation, we receive information about the contrast distribution, e.g., the mass density distribution of one particle. In the case of concentrated systems, we receive combined information about the single particle and the interaction between different particles.

In most cases, the sample and/or the sample environment are rather bulky.

Therefore, SANS instruments usually have to be large themselves in order to yield the desired resolution. Small SANS instruments can only serve a very limited number of applications. For reasons of intensity, a relatively large beam divergence, i.e., a beam cross section larger than the sample size is accepted as well as wavelength resolutions $\Delta\lambda/\lambda$ of up to about 20%.

SANS and SAXS techniques are complementary; however, they share several similarities. Perhaps the most important of these is the fact that, with minor adjustments to account for the different types of radiation, the same basic equations and "laws" (for example, those due to Guinier and Porod) can be used to analyze data from any of the two techniques. This is a great advantage and one that has certainly eased the transition from one technique to another.

Author details

Cristian A. Dragolici[*]

Address all correspondence to: adrag@nipne.ro

Horia Hulubei National Institute for R&D in Physics and Nuclear Engineering (IFIN-HH), Bucharest-Magurele, Romania

References

[1] Guinier A., Fournet G. Small-Angle Scattering of X-rays. New York: John Wiley & Sons Inc.; 1955. 268 p.

[2] Bacon G. E. Neutron Diffraction. 3rd ed. Oxford: Claredon Press; 1975. 636 p.

[3] Gerold V., Kostorz G. Small-angle scattering applications to materials science. J. Appl. Cryst. 1978; 11: 376–404.

[4] Allen A. J., Windsor C. G., Rainey V., Pearson D., Double D. D., Alford N. M. A small angle neutron scattering study of cement porosities. J. Phys. D: Appl. Phys. 1982; 15: 1817–1833.

[5] Marshall W., Lovesey S. W. Theory of Thermal Neutron Scattering. 1st ed. Oxford: Claredon Press; 1971. 599 p.

[6] Kostorz G., editor. Treatise on Materials Science and Technology. 1st ed. New York: Academic Press; 1979. 523 p.

[7] Ostanevich Y. M. Time-of-flight small-angle scattering spectrometers on pulsed neutron sources. J. Makromol. Chem. 1988; 15: 91–103.

Probing Giant Magnetism on Fe-N Thin Film by Polarized Neutron Reflectivity

Xiaowei Zhang, Nian Ji, Valeria Lauter, Haile Ambaye and Jian-Ping Wang

Additional information is available at the end of the chapter

Abstract

With the development in hard drive and permanent magnet industry, higher saturation magnetization (Ms) or magnetic induction (Bs) material is on high demand. According to the Slater-Pauling curve, the highest Bs value is ~2.45 T, which belongs to FeCo alloy. However, in 1972, Kim and Takahashi [1] announced that the new material Fe-N thin film exhibited an increase in the Bs value of 18%. From then on, tons of research works [2, 3, 4] had been dedicated in this area with conclusions on both sides, achieving either high Bs or low Bs. Among those works, the Bs values were obtained from the measurement of the thin film magnetic moment and its volume, which might cause a considerable amount of error depending on the accuracy of the film thickness and area measurement. Other concerns also include the uncertainty of Ms value due to the subtraction of Fe underlayer. Indeed, a direct measurement of Bs is the key to clarify the discrepancies between these results. Here, we are presenting the method of polarized neutron reflectometry (PNR) to measure the Bs of the partially ordered $Fe_{16}N_2$ thin film. PNR allows the interface magnetism study, [5] the *absolute* magnetization determination and magnetic depth profile in single thin films, [6, 7, 8, 9] and complicated superlattice structures. [10, 11] In the following scenarios, different partially ordered $Fe_{16}N_2$ thin films are fabricated and are measured using PNR subsequently. Their Bs values are obtained using the fitting results of nuclear scattering length density (NSLD) and magnetic scattering length density (MSLD). Also, a PNR application on FeN thin film will also help us to understand the switching picture of the FeN thin film with external applied field.

Keywords: $Fe_{16}N_2$, high saturation magnetization, polarized neutron reflectivity, thin film

1. Introduction

1.1. PNR Introduction

The interaction of neutrons with matter can be described in the optical formalism using the concept of reflective index for the medium. This can be obtained by Schrödinger equation, where the interaction of the neutron with medium is denoted by V:

$$\left[-\frac{\hbar^2}{2m}(\Delta + k_0^2) + V \right]\Psi = 0 \tag{1}$$

$$\frac{\hbar k_0^2}{2m} = \omega \tag{2}$$

where m is the neutron mass, k_0 is the wave vector in vacuum, $\hbar\omega$ is its energy. So the refractive index can be written as:

$$n^2 = 1 - V / \hbar\omega \tag{3}$$

Here, we can define the strong interaction potential with born approximation, which can be described by the Fermi pseudopotential: [12]

$$V_F(r) = b\left(\frac{2\pi\hbar^2}{m}\right)\delta(r), \tag{4}$$

where b is the scattering length and r is neutron position. The mean potential of the interaction between neutron and medium is the given by the integration of the space:

$$V = \frac{1}{V}\int V(r)d^3r = \frac{2\pi\hbar^2}{m}Nb, \tag{5}$$

where N denotes the number density of the atoms. The multiplicity of number density and scattering length is called scattering length density (SLD) ρ.

2. Specular reflectivity of neutrons from interface

If we compare the situation of neutron reflection to the light propagation at the interface of different mediums, the different interaction potential of neutron with medium can be seen as different mediums with different refraction indices. This follows Fresnel equations (Fig. 1).
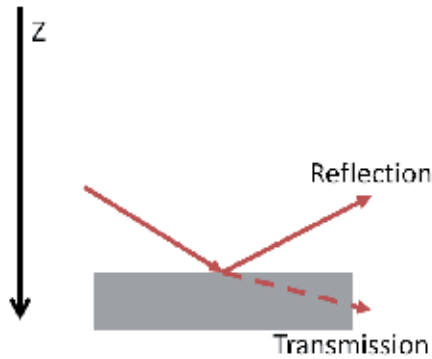
Figure 1. A schematic illustration of neutron interacting with matters at the interface obeys the Fresnel equations in analogy to the optical formalism.

$$R = |r|^2 = \left| \frac{k_1 - k_2}{k_1 + k_2} e^{i2k_1 z} \right|^2$$
$$T = |t|^2 = \left| \frac{2k_1}{k_1 + k_2} e^{i2(k_1 - k_2)z} \right|^2$$
(6)

For bulk materials, after applying Snell-Descartes' law, the reflection coefficient at a small incident angle can be written as a function of the wave-vector transfer q:

$$R(q) = \left| \frac{q_z - \sqrt{q_z^2 - q_c^2}}{q_z + \sqrt{q_z^2 - q_c^2}} \right|^2 ,$$
(7)

where q_c is the wave vector, which corresponds to critical angle of total external reflection. It is also easy to show that at high q limit, the reflectivity R follows the $1/q^4$ power law (Fresnel decay).

Dynamic calculation can also be applied with Born approximation. The reflectivity is equal to the Fourier transformation of the SLD profile: [13]

$$R = \frac{1}{q_z^2} \left| \int_{-\infty}^{\infty} e^{iq_z y} \rho(y) \, dy \right|^2 .$$
(8)

It is worth mentioning that Fresnel decay originates from a planar surface and the decay will result in a extremely low intensity at high q value, which will be very difficult to collect with the mixture of background noise or incoherent scattering from the substrate.

The critical angle θ_c is usually small and can be written as follows at the total reflection condition:

$$\cos\theta_c = n = 1 - \frac{\lambda^2}{2\pi}Nb,$$ (9)

where λ is the wavelength. It is useful to use Taylor expansion. Therefore, the critical angle θ_c and the corresponding critical wave vector q_c are

$$\theta_c = \sqrt{\frac{Nb}{\pi}}\lambda$$ (10)

$$q_c = 4\sqrt{\pi Nb}.$$ (11)

Usually the thickness of the thin film is larger than the wavelength of neutron, and so the reflecting beams of the neutron will give constructive/destructive patterns according to Bragg's diffraction law. Figure 2 is an example of a reflectivity from a bare bulk substrate and of a typical thin film:
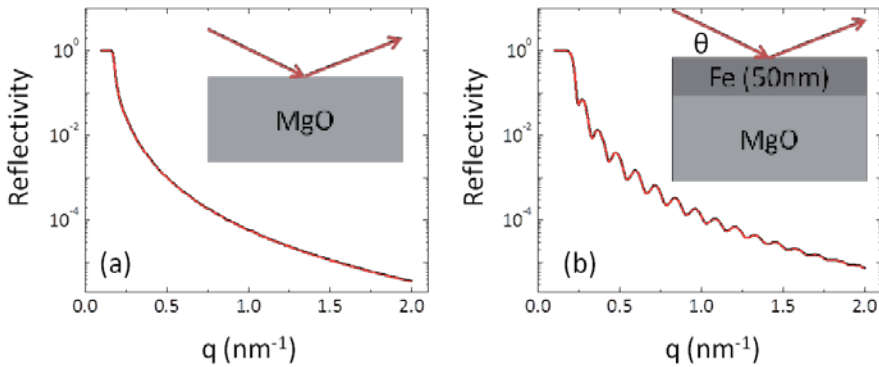
Figure 2. Simulated neutron reflectivity curves of (a) a flat MgO substrate and (b) a flat 50-nm-thick Fe thin film grown on MgO substrate.

3. Neutron reflectivity from a magnetic interface

In the presence of an external magnetic field, B, Zeeman energy will be present due to the spin of neutron itself:

$$V_Z = -g_n \mu_n B, \tag{12}$$

where $g_n \mu_n$ gives the neutron magnetic moment. Since $B = \mu_0 H + M$, where M is the magnetization of the material, we can express the potential in terms of M. At the magnetic interface with the addition of this energy, the total interaction potential energy between the neutron and medium can be written as follows:

$$V = \frac{2\pi\hbar^2}{m}(\rho_n \pm \rho_m), \tag{13}$$

where ρ_n is the nuclear SLD of the medium and ρ_m is the magnetic SLD of the medium, which can be defined by:

$$\rho_m = -\frac{m}{2\pi\hbar^2}\mu_n \sum M. \tag{14}$$

The sign ± represents spin-up and spin-down cases corresponding to the magnetization of the medium. In respect to neutron polarization, this shows that the magnetic SLD is directly related with the magnetization in the medium that the neutron is shining upon, which gives a direct measurement of the saturation magnetization when saturated in the external field.

Similarly, the critical angle θ_c and corresponding critical wave vector q_c can be written as:

$$\theta_c = \sqrt{\frac{\rho_n \pm \rho_m}{\pi}}\lambda \tag{15}$$

$$q_c = 4\sqrt{\pi(\rho_n \pm \rho_m)}. \tag{16}$$

Therefore, spin-up reflectivity will have a large critical angle/momentum transfer compared to spin-down reflectivity (Fig. 3). If we present the potential in the matrix form with Pauli operator, then:

$$V = \frac{2\pi\hbar^2}{m}\begin{pmatrix} \rho_n & 0 \\ 0 & \rho_n \end{pmatrix} \mp \mu_n \begin{pmatrix} B_z & B_x - iB_y \\ B_x + iB_y & -B_z \end{pmatrix} = \frac{2\pi\hbar^2}{m}\begin{pmatrix} \rho_n + \rho_{mz} & \rho_{mx} - i\rho_{my} \\ \rho_{mx} - i\rho_{my} & \rho_n - \rho_{mz} \end{pmatrix}. \tag{17}$$

The potential we obtained above is the diagonal terms, which corresponds to the non-spin flip situation. The off diagonal terms [14]will represent the spin flip situation, which will not be discussed in this article.
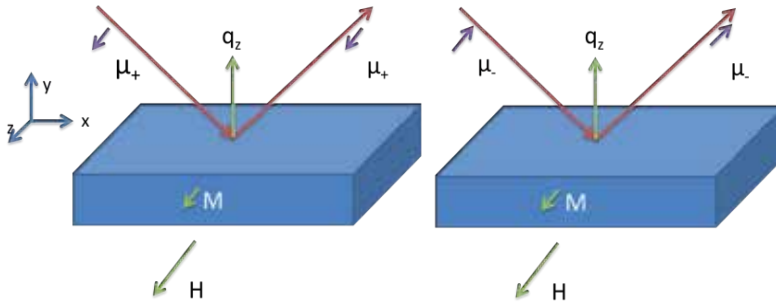
Figure 3. Polarized neutron reflectivity with two different spin polarizations. The spin-up (μ+) and spin-down (μ−) neutrons are indexed as parallel and anti-parallel with respect to the external field direction.
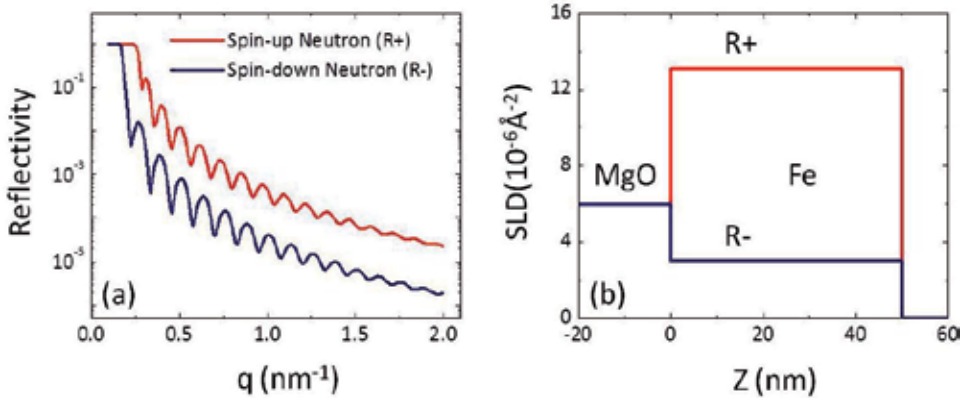
Figure 4. (a) The simulated reflectivities of a 50-nm Fe thin film grown on MgO substrate after saturation in-plane with external field. (b) The depth-dependent SLD according to the reflectivity curves in (a).

As seen from the reflectivity curves (Fig. 4), the magnetic interaction splits the non-magnetic oscillation curve into two branches. Fitting the reflectivity will yield the SLD for each spin case:

$$\rho_{tot+} = \rho_n + \rho_m$$
$$\rho_{tot-} = \rho_n - \rho_m. \tag{18}$$

We can solve for ρ_m and, therefore, retrieve the Ms of the sample.

4. Giant Bs induced by strain effect on epitaxial $Fe_{16}N_2$ thin film [15]

Two sets of partially ordered $Fe_{16}N_2$ thin film samples are fabricated on MgO substrate with facing target sputtering system. After the deposition of Fe underlayer at 300°C, a Fe-N layer

is grown subsequently on the top of Fe layer at room temperature with the optimum volume ratio of N_2 and Ar mixture so that the stoichiometry in Fe-N layer is Fe/N=8:1. An in-situ annealing is carried out right after at 120°C for 20 hours in vacuum. To explore the in-plane tensile strain effect on the Bs value of Fe-N thin film, two samples are grown with different Fe underlayers, 2 nm and 20 nm, respectively.
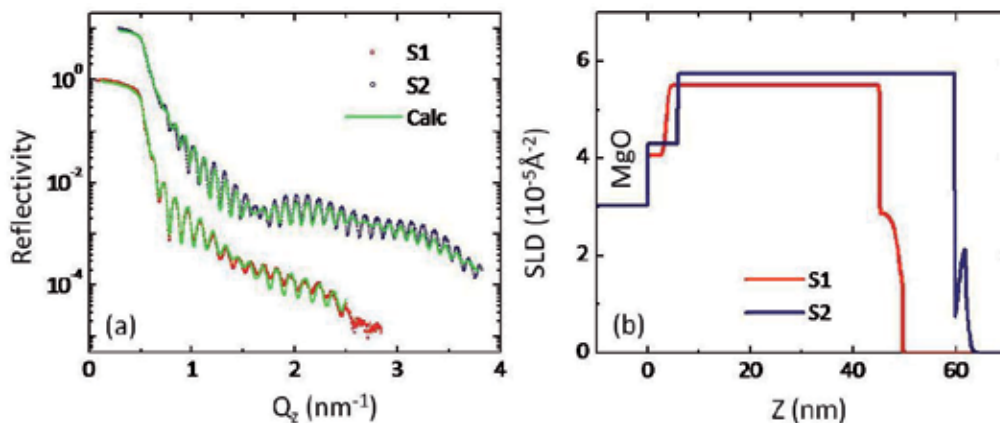
Figure 5. X-ray reflectivity characterization. (a) The fitted x-ray reflectivity curves measured on samples S1 and S2 (vertically offset by a factor of 10). (b) Calculated depth-dependent x-ray SLD profiles.

Both samples are investigated by PNR using the Magnetism Reflectometer at Spallation Neutron Source at Oak Ridge National Laboratory (SNS ORNL). [16] The reflectivities with the spin of the neutrons being either parallel (R^+) or anti-parallel (R^-) to the applied magnetic field are collected simultaneously. From these data the depth profiles of the SLD of both NSLD and MSLD are obtained. The PNR experiments are performed at room temperature in the saturation external field of *H*=1.0 T applied in-plane of the sample. The R^+ and R^- reflectivity data are fitted simultaneously using a genetic algorithm with an exact recursive matrix calculation embedded in the *Simulreflec 1.0* package. [17] The experimental reflectivity and calculated curves with best chi-squared fit for samples S1 and S2 are shown on Fig. 6a and b, respectively. Their corresponding structural NSLD and magnetization depth profiles are plotted in Fig. 6c and d.

In data modeling process, the structural NSLD and layer choice were constrained to closely match X-ray Reflectivity (XRR) results (Fig. 5). To account for the possibility that the film possess homogeneous chemical composition but potentially different magnetization, the Fe-N layer was subdivided into three slabs where NSLD are forced to be identical but thickness, roughness, and MSLD were allowed to vary independently. When fitting the data to extract the physical depth profile of the film structure, the only free parameter that was allowed to vary was the magnetization as other parameters were already framed by the XRR result and only marginal improvement was possible. After the comparison of the XRR and PNR result, we can find a relatively large roughness at high Q range, which is most likely due to either not
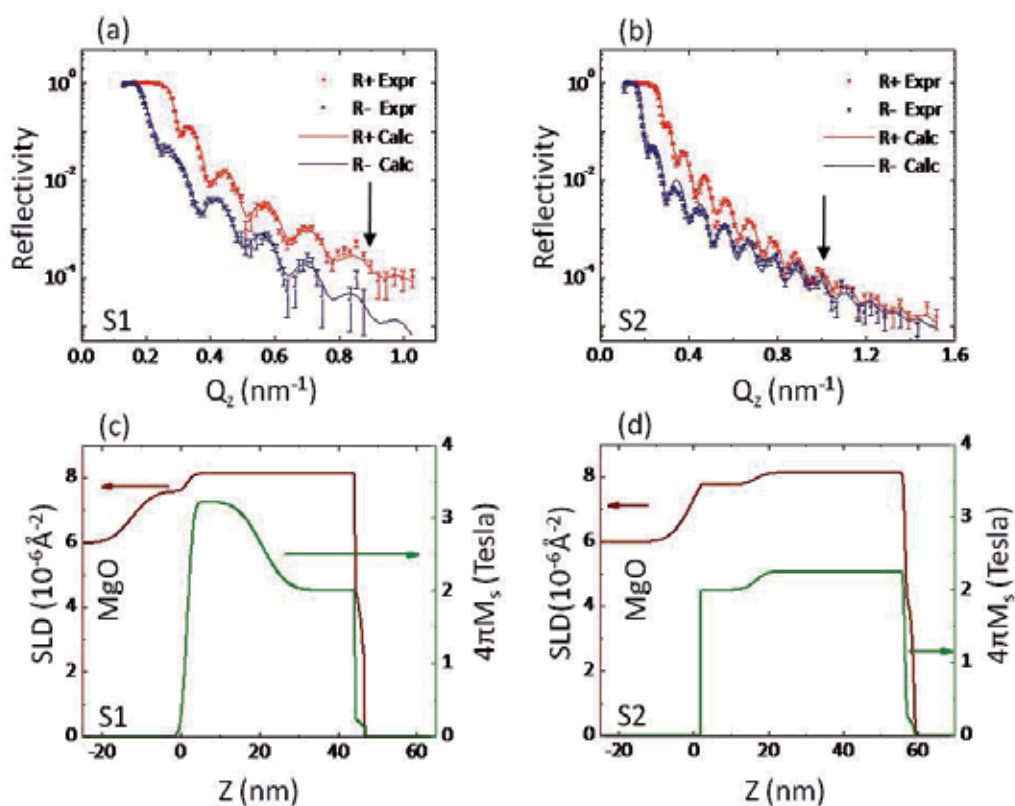
Figure 6. Polarized neutron reflectivity characterization. (a) and (b) Experimental polarized neutron reflectivities together with the fitted curves as functions of momentum transfer Q for samples S1 and S2 as labeled, respectively. The arrows at high Q region (>0.8nm⁻¹) indicate the difference of the magnetic properties toward the bottom interface between these two samples. (c) and (d) Structural (Brown) and magnetic (Green) depth profiles for samples S1 and S2 as labeled correspondingly.

enough data acquisition at this specific range or the chemical compound that is formed at the interface during the thin film growth or annealing process, such as MgO:N.

It is very obvious that an anomalously large magnetization is formed at the bottom of the film with a range of about 20 nm. The MSLD for this part of the film is $7.2\sim7.5 \times 10^{-6}\text{Å}^{-2}$, which in turn means the Ms value is $3.1\sim3.2$ T. This value is significantly higher than bulk Fe (40~50%) and $Fe_{65}Co_{35}$ (20~30%). When the SLD profile extends to higher layer of the film, the MSLD values drops to $4.66 \times 10^{-6}\text{Å}^{-2}$ and represents a low Ms value of 2.01 T. This non-uniformity of the magnetization across the film cannot be replaced by single layer model, which will fail to resemble the reflectivity behavior of the experiment. For sample S2, the resulted MSLD is close to $5 \times 10^{-6}\text{Å}^{-2}$ for the Fe-N layer, corresponding to Ms of 2.15 T, which does not show the presence of giant Bs. The different Bs results of the two samples are due to the strain that is experienced by the epitaxial growth of the Fe-N layer. In sample S1, larger in-plane tensile strain contributes to high Bs.

Further justification for the different magnetic structure upon Fe buffer thickness change comes from the spin asymmetry (SA) $(R^+ - R^-)/(R^+ + R^-)$ plot shown in Fig. 7. SA of both samples were fitted with experiment data. Initially, the SA values of both samples are oscillating at a high value. However, the SA value of sample S2 drops rapidly close to zero, whereas that of sample S1 almost reaches unity. In this high scattering vector region ($q > 0.8 nm^{-1}$), the interface of the bottom layer will dominate MSLD and NSLD. To account for the disparity of the different behaviors of two samples, |MSLD–NSLD| >> MSLD needs to be satisfied for sample S1. Since NSLD is similar for both samples, this observed feature directly proves the substantial enhancement of MSLD in the high Ms sample comparing to that of S2 at the bottom interface.
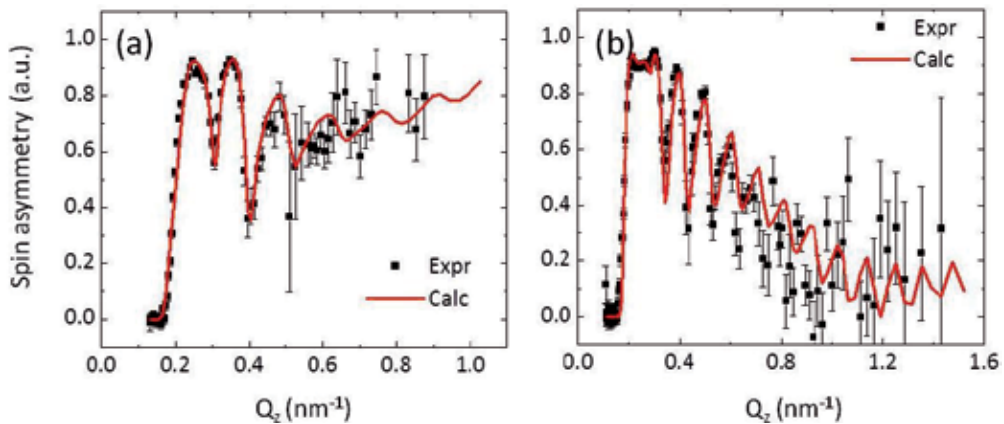
Figure 7. Spin asymmetry plotting of samples S1 (a) and S2 (b). It is clear as it approaches high q, the trend of the curves are different for these two samples.

5. High Bs obtained on partially ordered $Fe_{16}N_2$ multilayer thin film [16]

Multilayer structures are very common in many areas that they can bring many new physical phenomena. To explore the possibility of applying $Fe_{16}N_2$ in multilayer structure, two samples are fabricated on GaAs substrate with Fe/Fe-N layer stack. Samples L1 and L3 are with 1 and 3 repetitions, respectively.

It is known that co-refining the x-ray and neutron reflectivity curves allows an unambiguous determination of magnetic depth profile. [19, 20] When modeling the chemical part of the film structure, consistent structure for fitting both samples is set the same for both PNR and XRR. In this case, only marginal adjustment is allowed during the fitting process. The two layer model for L1 and four layer model for L3 work well in both fitting, which illustrates the neutron scattering of Fe and N elements that accounts for the difference for each layer. It is also found out that the N concentration at the interface region is lower than that before annealing process.

PNR was conducted on these two samples, respectively, with field applied in-plane to saturate the magnetic moment. It is important to notice that these samples are different from the ones
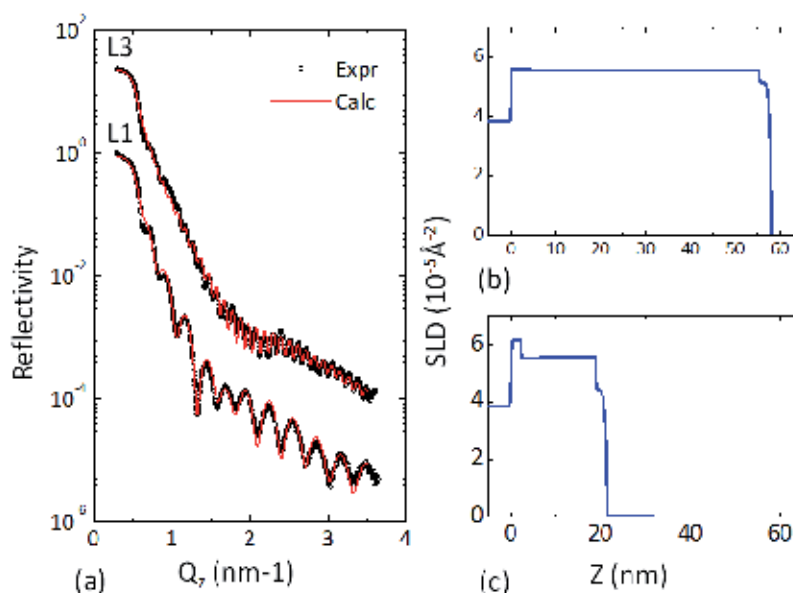
Figure 8. (a) X-ray reflectivity of $Fe_{16}N_2$ samples L1 and L3. (b) Electron SLD of L3 was homogeneous through the whole sample. (c) SLD of L1 stayed the same after the first ~2 nm bump.

with optimum FeN atomic ratio (Fe/N=8/1), whose Ms values are homogeneous throughout the film according to PNR measurement. In Fig. 9, reflectivity curves showed different oscillatory periods due to the differences in film thickness. Green lines of both samples in Fig. 9 (b) and (d) indicate the giant Ms at the bottom of the film, with a thickness of 5 nm, respectively. Since all the other FeN phases possess low Ms values, the only option for this enhancement should come from $Fe_{16}N_2$. Considering the fact that Fe seed layer is deposited before FeN layer, N atoms diffusion is most likely to occur to form $Fe_{16}N_2$ at the bottom as N atoms are initially rich on the top of Fe underlayer. $Fe_{16}N_2$ is formed at this specific location near the substrate with the right stoichiometric amount of N atoms. On the top of this giant Ms layer, a N rich phase is expected since N atoms are initially rich and a lower Ms result is obtained by PNR. This transition of Ms from high to low also occurs on L3. A reduced but still "giant" magnetization resides at the bottom interface. Compared to sample L1, the transition from high Ms to low Ms is comparably slow. Considering the XRD analysis achieved above, α''-$Fe_{16}N_2$ and α'-Fe-N martensites are present in the film structure. Since high Ms behavior is obtained, these observation on PNR analysis can only be explained by the presence of high Ms $Fe_{16}N_2$ phase and N rich phase. The formation of these mixture phases is most likely due to the strain that the film experiences with thinner Fe underlayer on the substrate. Multilayer structure of Fe/FeN provides the same environment of single Fe/FeN layer, but the difference is that higher Fe/FeN layers, which are not next to substrate, do not exhibit giant Ms. This is a result of the lattice strain relaxation in the film norm direction. To better demonstrate the fitting of PNR, chemical structure extracted from NSLD was checked and the corresponding model also fitted XRR data. It is noticeable that the bottom part of samples L1 and L3 have different
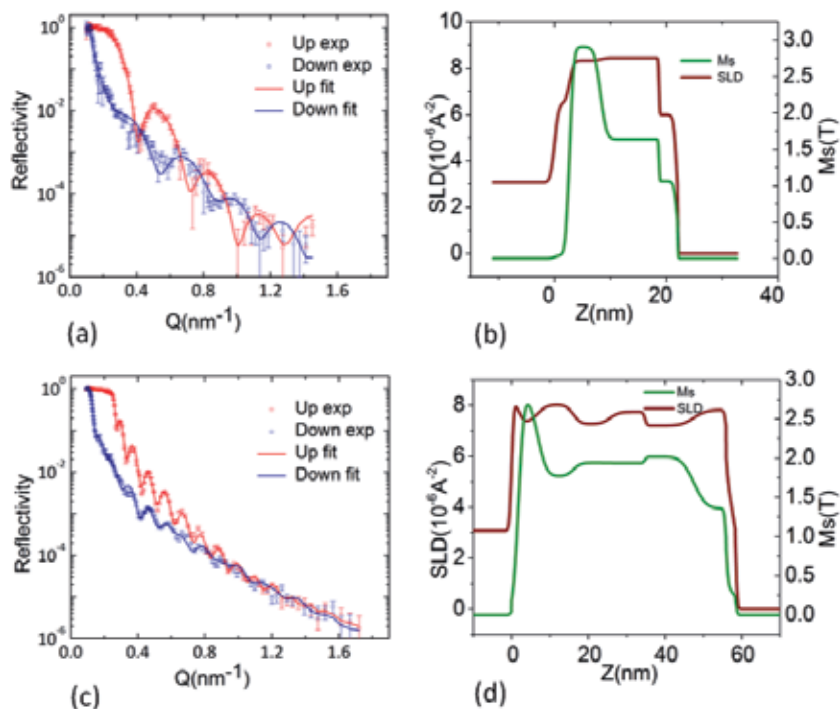
Figure 9. (a) Experimental and fitted reflectivity of sample L1. (b) Sample L1 SLD and Ms in-depth profile after fitting. (c) Experimental and fitted reflectivity of sample L3. (d) Sample L3 SLD and Ms in-depth profile after fitting. Both (b) and (d) curves exhibit high Ms value at bottom part of the film for ~5 nm scale.

electron and NSLD from XRR and PNR result. This region is most likely Fe and GaAs compound due to the inter-diffusion of Fe and GaAs atoms at their interface. The addition of this layer actually improved our fitting to the experiment data and was confirmed by SLD depth profile.

6. Using PNR to visualize the high perpendicular crystalline anisotropy [19]

The ordered $Fe_{16}N_2$ unit cell possesses tetragonality that gives rise to a high crystalline anisotropy, which is perpendicular to the film plane. This can be measured using vibrating sample magnetometer (VSM) in Fig. 10. However, VSM will not give detail information that will illustrate the FeN layer behavior in presence of the applied magnetic field.

During the PNR experiment, the external field is applied in the film plane direction. Both spin configuration signals are collected simultaneously. Fig. 11a–c show the reflectivity curves with fitting for spin-up and spin-down cases in three different external field intensities. At an external field of 20 kOe, the whole film magnetic moment will be saturated in the external field direction.

Since the same sample is tested in different fields, the chemical part, namely NSLD, stays the same during the fitting process. Three different MSLD depth profiles are generated after fitting in Fig. 11e. Since only one field intensity is strong enough to saturate the film in the film plane direction, the MSLD represent the in-plane component of the magnetization. It is clearly seen that the MSLD value drops rapidly for Fe-N layer, compared to Fe layer, when the external field is lowered. Since Fe layer is magnetically soft, all three fields will keep the Fe moment aligned in-plane. For Fe-N layer, there could be two scenarios to consider. First, the Fe-N film consists of antiferromagnetic domains in the film plane, which means the Fe-N layer has uniaxial in-plane anisotropy. This would directly contradict the fact that in-plane M-H loop does not depend on the in-plane orientation. Also, in this case, a strong off-specular signal should be observed, which is not our case either. Second, the magnetic moment turns out-of-plane due to perpendicular easy axis. This does explain our result since we do not observe off specular signal. When external field is lowered, the out-of-plane component of Fe-N film parallels the neutron beam momentum transfer and in-plane component contributes to the specular reflectivity. Therefore, the reduction of the magnetization in the in-plane direction after lowering external field can be explained by the out-of-plane easy axis of the Fe-N film.

Also, it is worth to mention that the oscillation amplitude of the reflectivity curves for R^- curve is much smaller than that of R^+ curve. This is most likely due to the modulation of the external field that the SLD is getting close to that of the substrate. This phenomenon is more robust when it approaches the Fe/GaAs interface where the reflectivity behavior is most dominated by this region at high q_z.
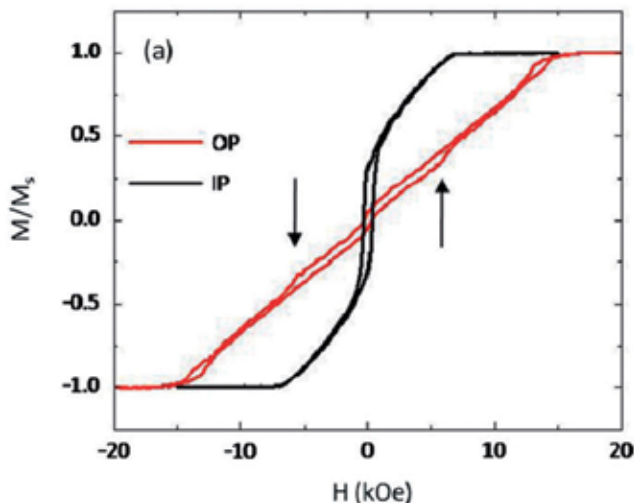
Figure 10. In-plane (black) and out-of-plane (red) M-H loops measured on one partially ordered $Fe_{16}N_2$ sample. The Fe-N layer switches at Hc~5.7 kOe (black arrows).
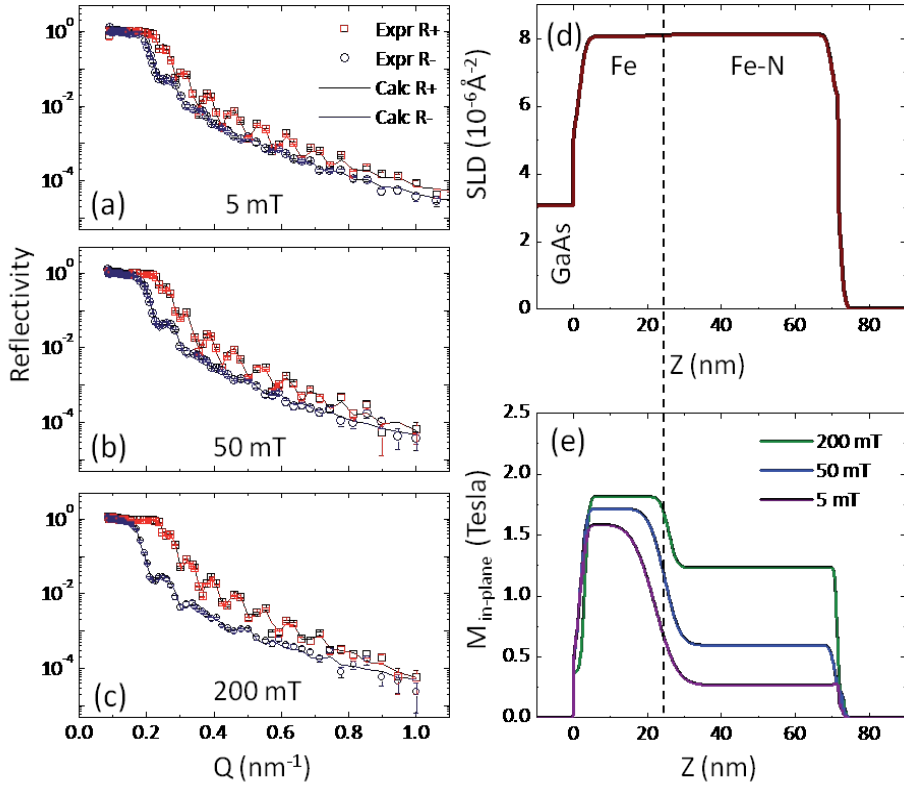
Figure 11. (a)–(c) Fitted reflectivity curves with experiment data of Fe-N sample at external field of 5, 50, and 200 mT, respectively. (d) NSLD depth profile of Fe-N sample and (e) MSLD, the in-plane magnetization component, depth profile of Fe-N sample at above three different external fields.

7. Summary

By using PNR, the Bs value can be accurately obtained directly in contrast to the conventional way that involves the thin film volume. In addition, we are also obtaining the Fe-N thin film NSLD and MSLD in-depth profile, which helps us to understand the physics behind the high Bs value. The above results are all derived from the specular reflections of the polarized neutron beam. This will facilitate the understanding of the giant Bs partially ordered $Fe_{16}N_2$ thin film in the film plane direction.

Acknowledgements

Author details

Xiaowei Zhang[1,2*], Nian Ji[1,2], Valeria Lauter[3], Haile Ambaye[3] and Jian-Ping Wang[1,2]

*Address all correspondence to: jpwang@umn.edu

1 Electrical and Computer Engineering Department and the Center for Micromagnetics and Information Technologies (MINT), University of Minnesota, Minneapolis, Minnesota, USA

2 Physics Department, University of Minnesota, Minneapolis, Minnesota, USA

3 Neutron Science Scattering Division, Oak Ridge National Laboratory, Oak Ridge, Tennessee, USA

References

[1]   T. K. Kim and Takahashi, Appl. Phys. Lett. 20, 492 (1972).

[2]   Y. Sugita, H. Takahashi, M. Komuro, K. Mitsuoka and A. Sakuma, J. Appl. Phys. 76, 6637 (1994).

[3]   M. A. Russac, C. V. Jahnes, E. Klokholm, J. Lee, M. E. Re, and B. C. Webb, J. Appl. Phys. 70, 6427 (1991).

[4]   J.-P. Wang, N. Ji, X. Liu, Y. Xu, C. Sánchez-Hanke, Y. Wu, F. M. F. de Groot, L. F. Allard , and E. Lara-Curzio Depa.

[5]   J. Chakhalian, J. W. Freeland, G. Srajer, J. Strempfer, G. Khaliullin, J. C. Cezar, T. Charlton, et al., Nat. Phys. 2, 4 (2006) 244–248.

[6]   J. A. C. Bland, D. Pescia, and R. F. Willis, Phys. Rev. Lett. 58, 1244 (1987).

[7]   M. A. M. Gijs, F. Petroff, Magnetic Ultra Thin Films, Multilayers and Surfaces Elsevier, 1997.

[8]   J. A. C. Bland, J. Lee, S. Hope, G. Lauhoff, J. Penfold, D. Bucknall, J. Magn. Magn. Mater. 165, 46 (1997).

[9]   S. J. Blundell, M. Gester, J. A. C. Bland, H. J. Lauter, V. V. Pasyuk, and A. V. Petren-ko, Phys. Rev. B 51, 9395 (1995)

[10] J. A. Borchers, J. A. Dura, J. Unguris, D. Tulchinsky, M. H. Kelley, C. F. Majkrzak, S. Y. Hsu, R. Loloee, W. P. Pratt Jr., and J. Bass, Phys. Rev. Lett. 82, 2796 (1998).

[11] J. Hoppler, J. Stahn, C. Niedermayer, V. K. Malik, H. Bouyanfif, A. J. Drew, M. Rös-sle, A. Buzdin, G. Cristiani, H. U. Habermeier, and B. Keimer, Nat. Mater. 8, 315 (2009).

[12] X. L. Zhou and S. H. Chen, Phys. Rep. 257, 223–348 (1995).

[13] M. R. Fitzsimmons and C. F. Majkrzak, Application of Polarized Neutron Reflectom-etry to Studies of Artificially Structured Magnetic Materials. pp 15

[14] N. Ji, V. Lauter, X. Zhang, H. Ambaye, and J. P. Wang. Appl. Phys. Lett. 102, 072411 (2013).

[15] V. Lauter-Pasyuk, H.J. Lauter, B. Toperverg, O. Nikonov, E. Kravtsov, L. Romashev, V. Ustinov, J. Magn. Magn. Mater., 226 Part 2, 1694 (2001).

[16] V. Lauter, et. al., Physica B 404, 2543 (2009).

[17] http://wwwllb.cea.fr/prism/programs/simulreflec/simulreflec.html.

[18] X. Zhang, N. Ji, V. Lauter, H. Ambaye, and J. P. Wang, J. Appl. Phys. 113, 17E149 (2013).

[19] G. P. Felcher, Phys. Rev. B 24, 1595 (1981).

[20] C. F. Majkrzak, Physica B 173, 75 (1991).

[21] N. Ji, M. S. Osofsky, V. Lauter, L. F. Allard, X. Li, K. L. Jensen, H. Ambaye, E. Lara-Curzio and J.-P. Wang, Phys Rev B 84 (24), 245310 (2011).

Thermophysical Properties and SANS Studies of Nanoemulsion Heat Transfer Fluids

Bao Yang and Jiajun Xu

Additional information is available at the end of the chapter

Abstract

Cooling is one of the most important technique challenges faced by a range of diverse industries and military needs. There is an urgent need for innovative heat transfer fluids with improved thermal properties over currently available ones. This chapter discusses the development and characterization of nanoemulsion heat transfer fluids with phase changeable nanodroplets to increase the thermophysical properties and the heat transfer rate of the fluid. Nanoemulsion heat transfer fluids can be formed by dispersing one fluid into another immiscible fluid as nanosized structures such as droplets and tubes, in which those nanostructures are swollen reverse micelles with the dispersed phase and stabilized by the surfactant molecules. In addition to the enhancement of thermophysical properties such as thermal conductivity by mixing another liquid of higher thermal conductivity, an even larger amount of heat can be absorbed or released when these nanodroplets undergo phase transition from liquid to gas or vice versa, and thus enhancing the heat transfer rate. Three types of nanoemulsion heat transfer fluids are introduced: alcohol-in-polyalphaolefin, water-in-FC-72, and water-in-polyalphaolefin. Structural and property characterizations of these nanoemulsion heat-transfer fluids are the two main aspects of this chapter. This chapter also identifies several critical issues in the nanoemulsion heat transfer fluids to be solved in the future.

Keywords: Nanoemulsion, Thermophysical Property, Heat Transfer, Small Angle Neutron Scattering (SANS)

1. Introduction

Cooling is one of the most important technical challenges faced by a range of diverse industries: microelectronics, optoelectronics, and, especially, power electronics [1–8]. This technology gap is the result of the higher currents, switching frequencies, and component densities of today's electronics and power electronics. The advances in semiconductor materials and more precise

fabrication techniques have the unfortunate side effect of generating higher amounts of waste heat within a smaller volume. Today, it is not unusual to see heat fluxes of 200 W/cm^2 in a power module, a figure that is expected to increase over 1000 W/cm^2 in the near future.

Thermal management of such high flux is becoming the bottleneck to improvements in electronics and power electronics. Existing cooling systems is striving to meet the ever-increasing demand in higher computational power and smaller footprint. It is important that a cooling system with significantly improved heat transfer systems and their kernel components can be developed; in particular the cooling fluid used inside many heat transfer systems but yet has received little attention. The heat transfer fluids used in these heat transfer systems, including the coolants, lubricants, oils, and other fluids, limit the capacity and compactness of the heat exchangers that use these fluids due to their inherently poor heat transfer properties. The heat transfer capability of the heat exchangers can be easily amplified if fluids with better thermal properties are used. Therefore, development of innovative heat transfer fluids with improved thermal properties over those currently available is urgently needed.

The strategy of adding solid, highly conductive particles to improve thermal conductivity of fluids has been pursued since Maxwell's theoretical work was first published more than 100 years ago [9]. Early-stage studies have been confined to millimeter- or micrometer-sized solid particles dispersed in fluids. In the past decade, researchers have focused on suspensions of nanometer-sized solid particles, known as nanofluids [2, 8]. Many reviews and introductory reports on nanofluids have already been published [1, 2, 4, 10–14].

In this paper, it is intended to introduce some recent developments in another type of engineered heat transfer fluids, in which phase changeable nanodroplets are added to increase the thermophysical properties and heat transfer rate of the base fluids [15–22]. This chapter starts with the introduction of nanoemulsion fluids with potential application in thermal fluids. It is followed by the discussion on structural and thermophysical characterization techniques for nanoemulsion fluids [15–19, 21]. Then, three groups of nanoemulsion fluids and their properties are discussed. This chapter is not intended to serve as a complete description of all nanoemulsion fluids available for heat transfer applications. The selection of the coverage was influenced by the research focus of the authors and reflects their assessment of the field.

2. Nanoemulsion heat transfer fluids

One fluid is dispersed into another immiscible fluid as nanosized structures such as droplets and tubes to create a "nanoemulsion fluid." Those nanosized structures of the dispersed phase are micelles stabilized by the surfactant molecules on the outside. Nanoemulsion fluids are part of a broad class of multiphase colloidal dispersions [15–19, 21]. Different from the preparation of the nanofluids and emulsions [23–31], the nanoemulsion fluids are spontaneously generated by self-assembly which does not require external shear force. Thus the nanoemulsion fluids are thermodynamically stable [16–19, 23, 32–44]. Table 1 is the comparison between self-assembled nanoemulsion fluids and conventional emulsions. Nanoemulsion fluids made of specific fluids are suited for thermal management applications. Figure 1 shows

a picture of ethanol-in-polyalphaolefin (PAO) nanoemulsion heat transfer fluids: both PAO and PAO-based nanoemulsion fluids are transparent but the nanoemulsion exhibits the Tyndall effect [15, 16, 19, 21, 45, 46].
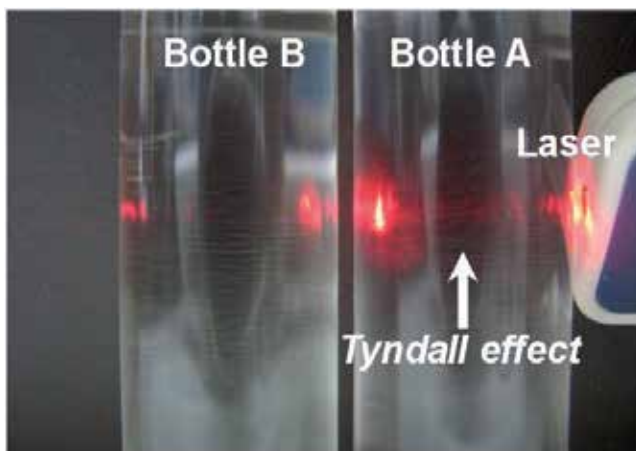
Figure 1. Pictures of ethanol-in-PAO nanoemulsion fluids (Bottle A) and pure PAO (Bottle B). Liquids in both bottles are transparent. The Tyndall effect (i.e., a light beam can be seen when viewed from the side) can be observed only in Bottle A when a laser beam is passed through Bottles A and B.

Sample	Property	Nanoemulsion	Emulsion
1	Appearance	Transparent	Turbid
2	Interfacial tension	Ultra low (usually <<1 mN/m)	Low
3	Droplet size	<50 nm	>500 nm
4	Stability	Thermodynamically stable, long shelf life	Thermodynamically unstable
5	Preparation	Self-assembly	N of external shear
6	Viscosity	Newtonian	Non-Newtonian

Table 1. Comparison of nanoemulsion fluids and emulsions

2.1. Formation of self-assembled nanoemulsion fluids

Self-assembled nanoemulsion fluids are thermodynamically stable, and the formation of these fluids can be explained using the classical thermodynamic theory [23, 34–39, 42, 43, 47–49]. The nanoemulsion fluid consists of one oil phase, one water phase, and certain surfactants. The adding of surfactant lowers the surface tension of the oil–water interface and the change in free energy of the system is given by Equation 1,

$$DG_f = \gamma DA - T \cdot DS \tag{1}$$

where DG_f is the free energy of formation, γ is the surface tension of the oil–water interface, DA is the change in interfacial area upon nanoemulsification, DS is the change in entropy of the system, and T is the absolute temperature. The change in DA is very high due to the large number of nanosized droplets in the nanoemulsion fluids. However, the interfacial tension γ is very small (usually <<1 mN/m), and therefore the increase in the surface energy, γ DA, could be smaller than the entropy arising from the mixing. The favorable entropic contributions also arise from dynamic processes such as surfactant diffusion in the interfacial layer and monomer–micelle surfactant exchange. The entropy of mixing can be large enough to compensate for the positive interfacial free energy and to give the nanoemulsion system a free energy lower than that of the unmixed components. So the self-assembled nanoemulsion fluids can be formed through self-assembly and are in fact thermodynamically stable system [23, 43, 50]. There are mainly two approaches to prepare nanoemulsion fluids: the spontaneous emulsification method (or the so-called phase titration method) and the phase-inversion method [23, 43].

Figure 2 shows the typical phase behavior diagram of a ternary system that contains two immiscible so-called oil and water phases and an amphiphilic surfactant component. The term "water" refers to a polar phase while "oil" is used for an apolar organic phase. When a system has a composition that lies in the shaded areas, a nanoemulsion fluid, either oil-in-water or water-in-oil, can be formed through self-assembly.
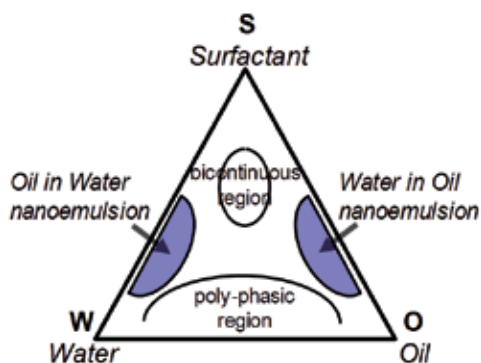
Figure 2. Schematic phase diagram of a water-oil-surfactant ternary system. The shaded areas are regions where self-assembled nanoemulsions are found.

2.2. Structure characterization methods

Similar to other multiphase colloidal dispersions, the microstructure of nanoemulsion fluids is sensitive to many factors, including the different dispersed liquid, surfactants and base fluid, and molar ratio of dispersed liquid to surfactant [34]. In addition to that, temperature, pH-value, and salinity also play an important role in the microstructure [23]. So accurate charac-

terization of the microstructure of nanoemulsion fluids is important to understand the nanoemulsion fluids and yet challenging and costly to perform. In the past, small angle X-ray scattering (SAXS), small angle neutron scattering (SANS), dynamic or laser-light scattering (DLS), transmission electron microscopy (TEM), and nuclear magnetic resonance (NMR) have been used for the structure characterization [23]. In addition, the measurement of nanoemulsion properties, such as viscosity, electric conductance, thermal conductivity, dielectric permittivity, electrophoretic birefringence, ultrasonic interferometry, and ultrasonic absorption, can also provide information on the internal microstructure.

SANS allows the characterization of the structures inside the material on the nanometer (10^{-9} m) to micrometer (10^{-6} m) scale [51]. Many advanced engineering materials obtain unique performance because of their engineered structures on this length scale. For example, the toughness of high-impact plastics depends on the admixture of stiff and flexible segments of polymer molecules on the nano-to-micro scale, as well as, many biological processes in cells: from the storage of information on magnetic disks, to the hardness of steels and superalloys, to the conduction of current in superconductors, and many other materials properties.

Among all methods currently available for characterizing the microstructure of nanoemulsion fluids, small-angle neutron scattering (SANS) provides a unique approach to probe structure in liquids thanks to the distinctive penetrating power of neutron. Unlike the conventional dynamic light-scattering method using laser or X-rays, it can be applied to "concentrated" colloidal suspensions (e.g., >1 % volume fraction) and can penetrate through a container [51–57]. Another advantage of SANS method is the deuteration method, in which deuterium labeled components in the sample in order to enhance their contrast that it can probe specific molecules or structure inside the sample with the deuteration technique. This unique method allows SANS to measure density fluctuations and composition (or concentration) fluctuations, which is very important to understand the structure inside nanoemulsion fluids [23].

2.3. Thermophysical properties characterization methods

2.3.1. Thermal conductivity

Low thermal conductivity is a primary limitation in the development of energy-efficient heat transfer fluids that are required in many industrial applications. Conventional heat transfer fluids have relatively poor thermal conductivity compared to metals [9]. It has been reported that the dispersed liquid nanodroplets could alter thermal conductivity of the base fluids [1, 2, 4, 58–61]. However, because of the absence of a theory for the thermal conductivity of nanoemulsion heat transfer fluids, an investigation of the effect of nanodroplets on the thermal conductivity will be conducted.

There are two widely used methods to measure the thermal conductivity of nanoemulsion fluids which includes (1) the transient hot-wire technique and (2) 3ω-wire method [62]. In the transient hot-wire method, thermal conductivity value is determined from the heating power and the slope of temperature change versus logarithmic time. The 3ω-wire method is used to measure the fluid thermal conductivity [19, 21, 62, 63]. This method is actually a combination of the transient hot-wire method and the 3ω-wire method, in which a metal wire is suspended

to a liquid acting as both heater and thermometer. One advantage of this 3ω-wire method is that the temperature oscillation can be kept low enough: it is usually below 1 K as compared to about 5 K for the hot-wire method. It greatly helps to retain constant liquid properties of test liquid during measurement. Calibration experiments were performed for hydrocarbon (oil), fluorocarbon, and water at atmospheric pressure before each measurement.

2.3.2. Viscosity

Viscosity is a measure of the resistance of a fluid which is being deformed by either shear stress or tensile stress. Viscosity is another macroscopically observable parameter that characterizes a nanoemulsion fluid, and it may range anywhere between a low viscous fluid and a gel state. It is an important quantity for many practical applications of nanoemulsion fluids, especially those used for hydraulic fluids. For instance, pumping such systems might be of interest in their application, and here viscosity plays an important role. Viscosity can be determined from the equation below:

$$F = \mu A \frac{u}{y} \tag{2}$$

where F is the stress force, u is the velocity, A is the area and μ is the proportionality factor called dynamic viscosity. The kinematic viscosity v is related to the dynamic viscosity by dividing by the density of the fluid, $v = \frac{\mu}{\rho}$.

Viscosity of a nanoemulsion fluid depends largely on its microstructure, that is, the type of aggregates that are present, on their interactions, and on the concentration of the system. So the viscosity can be used to monitor structural changes in the nanoemulsion system. In order to do so, one has to compare the experimental data to theoretical expressions that give the viscosity expected for certain model systems.

2.3.3. Specific heat measurement

The specific heat is the amount of heat per unit mass required to raise the temperature by one degree Celsius. A differential scanning calorimeter (DSC) is usually used to measure a material's specific heat. In DSC measurement, it compares the differential heat flow (heat/time) between the measured material and the empty reference pan by adjusting the heat flux into a pan containing the sample with the heat flux into an empty pan while keeping both the measured sample and reference sample at nearly the same temperature. The difference in the amount of heat supplied to the sample and the reference is recorded as a function of temperature (or time), and the positive or negative peaks in the relationship correspond to exothermic or endothermic reactions in the sample, respectively. In order to determine the sample heat capacity, three measurements are usually carried out: for the sample, for the baseline, and for a standard. The baseline is subtracted from the sample measurement to obtain absolute values of the heat flow to the sample. The heat capacity is to be determined by the heat flow, the temperature rise, and the sample mass.

3. Nanoemulsion heat transfer fluids

3.1. Ethanol-in-Polyalphaolefin (PAO) nanoemulsion fluids

Polyalphaolefin (PAO) has been widely used as dielectric heat transfer fluids and lubricants due to its chemical stability within a wide temperature range. However, its thermal properties are relatively poor compared to other heat transfer fluids [64]. Ethanol-in-PAO is a liquid–vapor phase change nanoemulsion fluid, in which over 90 % consist of PAO to keep its chemical stability very close to pure PAO. Meanwhile, the ethanol nanodroplets could evaporate explosively and thus enhance the heat-transfer rate of the base fluid PAO [16]. The microstructure and thermophysical properties of the ethanol-in-PAO nanoemulsion fluids are discussed below.

3.1.1. Microstructure of ethanol-in-PAO nanoemulsion fluids

The microstructure of ethanol-in-PAO nanoemulsion fluids are on the NG-3 (30 m) beamline at the NIST Center for Neutron Research (NCNR) in Gaithersburg, MD. Samples are loaded into 2-mm quartz cells. Figure 3 shows the SANS data, the scattering intensity I versus the scattering vector $q = 4\pi \sin(\theta/2)/\lambda$, where λ is the wavelength of the incident neutrons, and θ is the scattering angle. The approximation $q = 2\pi\theta/\lambda$ is used for SANS (due to the small angle θ). The analysis of the SANS data suggests that the inner cores of the swollen micelles, that is, the ethanol droplets, are spherical and have a radius of about 0.8 nm for 9 vol. %.
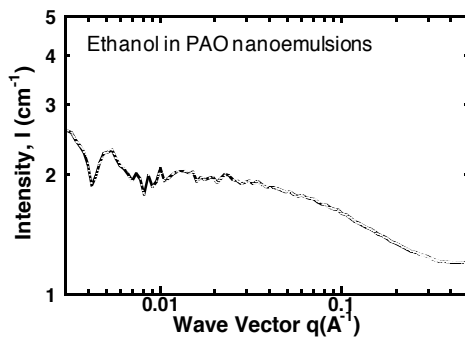
Figure 3. Intensity I vs. Wave Vector q measured in ethanol-in-PAO nanoemulsion fluids.

3.1.2. Thermal conductivity of ethanol-in-PAO nanoemulsion fluids

The relative thermal conductivity in ethanol-in-PAO nanoemulsion fluids measured using the 3ω-wire method along with the prediction by the Maxwell model (one model based on effective medium theory [EMT]) is shown in Figure 4. The relative thermal conductivity is defined as k_{eff}/k_o, where k_o and k_{eff} are thermal conductivities of the base fluid and nanoemulsion fluids, respectively. The effective medium theory reduces to Maxwell's equation for suspensions of well-dispersed, non-interacting spherical particles,

$$\frac{k_{\text{eff}}}{k_\text{o}} = \frac{k_p + 2k_\text{o} + 2\phi\left(k_\text{p} - k_\text{o}\right)}{k_p + 2k_\text{o} - \phi\left(k_\text{p} - k_\text{o}\right)} \tag{3}$$

where k_o is the thermal conductivity of the base fluid, k_p is the thermal conductivity of the particles, and ϕ is the particle volumetric fraction.

It can be seen in Figure 4 that the relative thermal conductivity of ethanol-in-PAO nanoemulsion fluids is rather moderate (e.g. 2.3 % increase for 9 vol. % ($k_{\text{PAO}} = 0.143$ W/mK and $k_{\text{alcohol}} = 0.171$ W/mK [64, 65]), and no strong effects of Brownian motion on thermal transport are experimentally found in those fluids although the nanodroplets are extremely small, around 0.8 nm [16]. The thermal conductivity also appears to be linear with the loading of ethanol nanodroplets over the loading range from 0 to 9 vol. %. The Maxwell's equation, however, underestimates the viscosity increase in the ethanol-in-PAO nanoemulsion fluids, as can be seen in Figure 4. This is probably because Maxwell's equation does not take into account the shape transformation with different ethanol concentrations. It may suggest that the ethanol droplets form column-like with high aspect ratio of length to radius, which leads to a higher thermal conductivity enhancement in nanoemulsion fluids than the spherical droplets.
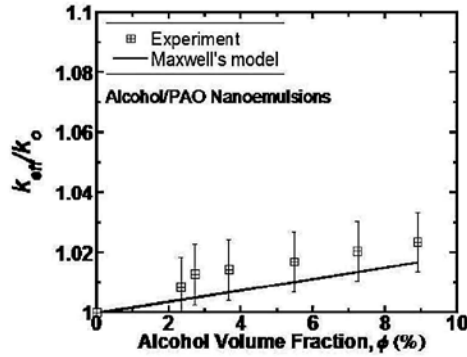
Figure 4. Relative thermal conductivity of ethanol-in-PAO nanoemulsions measured at different volume fractions of ethanol nanodroplets. The estimate from Maxwell's model is shown for comparison.

3.1.3. Viscosity of ethanol-in-PAO nanoemulsion fluids

Figure 5 shows the relative dynamic viscosity, $\mu_{\text{eff}}/\mu_\text{o}$, for the ethanol-in-PAO nanoemulsion fluids with varying alcohol loading, which is measured using a commercial viscometer (Brookfield DV-I Prime). The calibration is carried out using the pure PAO and its dynamic viscosity is found to be 7.3 cP which compares well with the literature value. Similar to thermal conductivity plotted in Figure 4, an approximately linear relationship is observed between the viscosity increase and the loading of alcohol nanodroplets in the range of 0–9 vol. %, but at a much larger percentage. For example, the measured viscosity increase is 31 % for 9 vol. %.

ethanol loading, compared to a 2.3 % increase in thermal conductivity. The viscosity increase of dilute colloids can be predicted using the Einstein equation[12],

$$\mu_{eff} / \mu_0 = 1 + 2.5\phi \qquad (4)$$

where μ_{eff} is the nanoemulsion viscosity, μ_0 is the base fluid PAO viscosity and φ is the volumetric fraction of encapsulated ethanol nanodroplets. The viscosity increase in the ethanol-in-PAO nanoemulsion fluids is underestimated by the Einstein equation, as can be seen in Figure 5. This discrepancy is probably because the droplet volume fraction, ϕ, used in the viscosity calculation does not take into account the surfactant layer outside the alcohol core and Einstein equation used here is derived from dilute system.
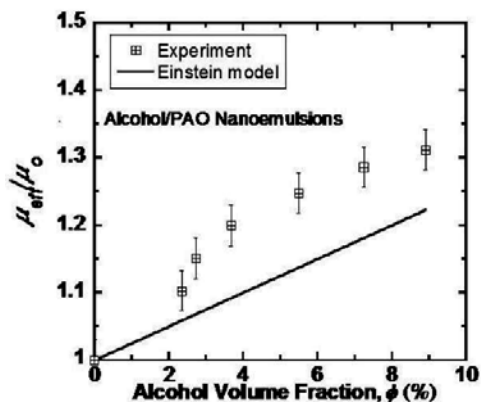
Figure 5. Relative viscosities of ethanol-in-PAO nanoemulsions measured at different volume fractions of ethanol nanodroplets. The estimate from Einstein model is shown for comparison.

3.2. Water-in-FC-72 nanoemulsion fluids

Water-in-FC-72 nanoemulsion fluids are another group of nanoemulsion fluids designed for heat transfer purpose, in which water could undergo liquid–solid transition and thus increase heat transfer rate of the base fluid FC-72. FC-72 is one of the lines of Fluorinert™ Electronic Liquids developed by 3M™, which is used as the cooling fluids in liquid-cooled thermal management systems due to its low boiling point and excellent dielectric properties [66]. However, its heat transfer properties such as thermal conductivity and heat capacity are much inferior, compared to other fluids such as water.

3.2.1. Microstructure of water-in-FC-72 nanoemulsion fluids

Water-in-FC-72 nanoemulsion fluids are generated by emulsifying deionized water into FC-72 with a small amount of perfluorinated amphiphiles. Figure 6 (a) shows the picture of the water-in-FC-72 nanoemulsion fluids and the pure FC-72. The autocorrelation function of the scattered

light for the 12 vol. % water-in-FC-72 nanoemulsion fluids is plotted in Figure 6 (b), in which the curve shows a typical exponential decay of the correlation function versus time [19, 21]. The Brownian diffusivity and effective hydrodynamic radius of the nanodroplets are found to be 3.5×10^{-7} cm^2/s and 9.8 nm at $T = 25$°C, respectively.
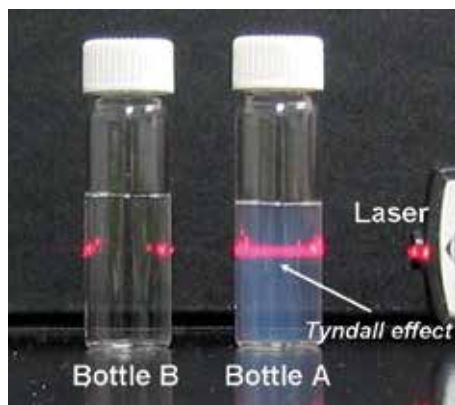
(a)
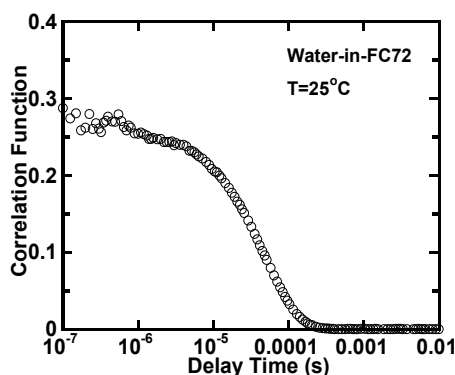
(b)

Figure 6. (a). Pictures of Water-in-FC-72 nanoemulsion fluids (Bottle A) and pure FC-72 (Bottle B). (b). Correlation function of the scattered light for the 12 vol.% Water-in-FC-72 nanoemulsion fluids. Measurements taken by a Photocor-Complex DLS instrument.

3.2.2. Thermal conductivity of water-in-FC-72 nanoemulsion fluids

Thermal conductivity of the water-in-FC-72 nanoemulsion is measured for different water loadings, and the results are shown in Figure 7. The 3ω -wire method is used to measure the fluid thermal conductivity. In water-in-FC-72 nanoemulsion fluids, the water phase has a thermal conductivity much higher than that of the base liquid FC-72. Water's thermal conductivity is 0.609 W/(mK) at 300 K and FC-72's thermal conductivity is much smaller, about 0.066 W/mK [66]. The addition of water is expected to improve the effective thermal conductivity of FC-72.

A very large increase in thermal conductivity (up to 52 % for water-in-FC-72 nanoemulsion of 12 vol. % water) can be seen in Figure 7. The observed enhancement in thermal conductivity is much larger than that predicted by the EMT with assumption of spherical droplets [67]. This suggests that the water droplets are column-like with high aspect ratio of length to radius, which leads to a higher thermal conductivity enhancement in nanoemulsion fluids than the spherical droplets.
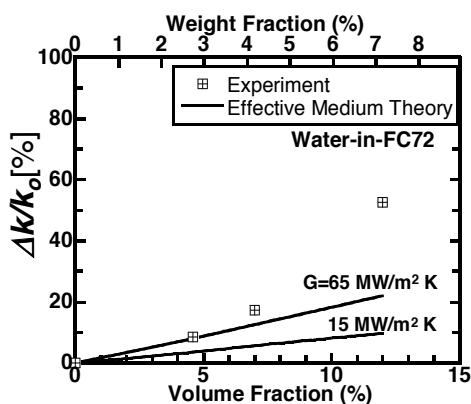
Figure 7. Relative thermal conductivity of water-in-FC-72 nanoemulsion fluids versus volume fraction of water. The estimate from EMT is shown for comparison.

3.2.3. Viscosity of water-in-FC-72 nanoemulsion fluids

The dynamic viscosity of water-in-FC-72 nanoemulsions of different nanodroplet concentrations is measured using a Brookfield viscometer at room temperature. The results have been normalized to the viscosity of pure FC-72 and are shown in Figure 8. The measured viscosity increase is nonlinear with the higher concentration of water added inside which agrees well with the nonlinear increase in thermal conductivity. This nonlinear increase in viscosity is common in colloidal systems, and has been interpreted by the aggregation of nanodroplets, that is, formation of column-like microstructure. Similar to the ethanol-in-PAO nanoemulsion fluids discussed previously, the Einstein equation significantly underpredicts the viscosity increase in the water-in-FC-72 nanoemulsion fluids at relatively high water loadings, as can be seen in Figure 8.

3.2.4. Effective heat capacity of water-in-FC-72 nanoemulsion fluids

Another significant thermal property enhancement can be achieved here using the phase change of water nanodroplets formed inside the water-in-FC-72 nanoemulsion fluids. In water-in-FC-72 nanoemulsion fluids, the fluid's heat capacity can be increased by the high specific heat of water(the volumetric heat capacity of water is about 4.18 J/ml K, and is over two times the heat capacity of PAO (1.74 J/ml K) [65]) and/or the latent heat of water is the highest among common heat transfer fluids (ΔH =334 J/g), depending on the operating
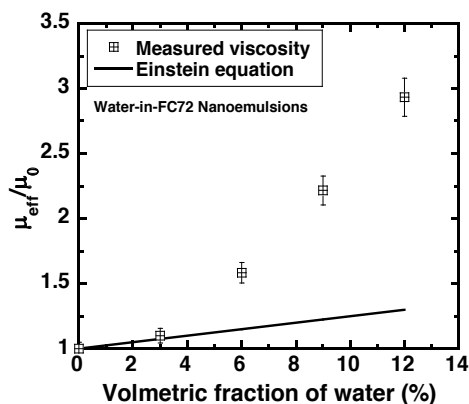
Figure 8. Relative Viscosity of Water-in-FC-72 Nanoemulsions versus volume fractions of water nanodroplets. The estimate from Einstein model is shown for comparison.

temperature of the fluids [66]. For example, the solid–liquid phase change of these droplets can increase the effective specific heat of the nanoemulsion fluid by a factor of $1 + \dfrac{\alpha \cdot H_{\text{water}}}{\Delta T \cdot C_{\text{FC72}}}$, where α is the water-volume fraction, H_{water} is the latent heat of fusion of water per unit volume, and ΔT is the temperature difference between the heat transfer surface and the bulk fluid.

The measured and calculated heat capacities of the water-in-FC-72 nanoemulsion fluids using a TA-CC100 DSC are shown in Figure 9. It can be seen that over 15 % increase in heat capacity can be achieved for a water volumetric fraction of 12 %, in which the measured $\alpha \cdot H_{\text{water}}$ values of the water-in-FC-72 nanoemulsions for water loadings of 3, 6, 9, and 12 vol. % are 10.52, 15.44, 25.48, 39.78 J/ml, respectively. The effective heat capacity of FC-72 can be enhanced by more than 200 % for a 12 vol.% of water-in-FC-72 nanoemulsion, according to these experimental data. It agrees well with theoretical prediction using the model mentioned above.

The use of phase-changeable nanodroplets (e.g. water nanodroplets) provides another way to simultaneously increase the effective specific heat and thermal conductivity of conventional heat-transfer fluids.

3.3. Water-in-PAO nanoemulsion fluids

3.3.1. Microstructure of water-in-PAO nanoemulsion fluids

Figure 10 shows the SANS data for water-in-PAO nanoemulsion fluids with water volumetric concentration covering 1.8 vol. % to 10.3 vol.%.

It is clear from the SANS data that intensity curves of water-in-PAO nanoemulsion fluids gradually change the shape with increasing water loading. They can be further classified into three ranges (marked using three different colors): the 1.8–4.5 vol. % water-in-PAO nanoemulsion fluids with a smooth and gradually increasing scattering intensity for low q range
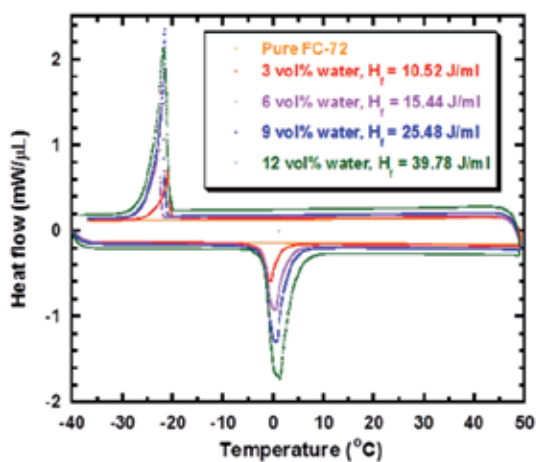
(a)
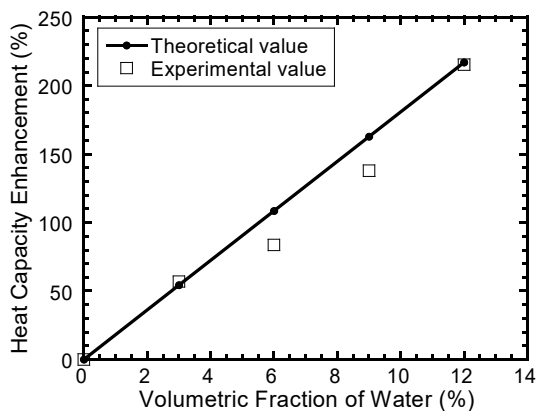
(b)

Figure 9. (a) DSC curves and latent heat of fusion values of water of the water-in-FC-72 nanoemulsion fluids with different water loadings. (b) The measured and calculated heat capacity enhancement in the water-in-FC-72 nanoemulsion fluids when the dispersed water droplets undergo solid–liquid phase transition.

(less than 0.1 Å); the 5.3–7.8 vol. % water-in-PAO nanoemulsion fluids with a sharper increase of q for the high q range (larger than 0.1 Å) and a flatter intensity curve for low q (less than 0.03 Å); and for even higher concentrations like 8.6 and 10.3 vol. % water-in-PAO nanoemulsion fluids tested here, the "hump" for high q is even more obvious and the intensity for low q increases more sharply which appears to have scattering curves made of three different sections. It indicates there is a dramatic microstructural change inside the water-in-PAO nanoemulsions of different water concentrations. Simple correlation length model cannot fit all the SANS curves well for both low and high q regions, as shown in Figure 11.

The hard sphere model (one typical simple correlation length model) fits well for low water concentrations (i.e. 1.8 % to 4.5 % volume fractions), and nanodroplet radii are found to be 13.2
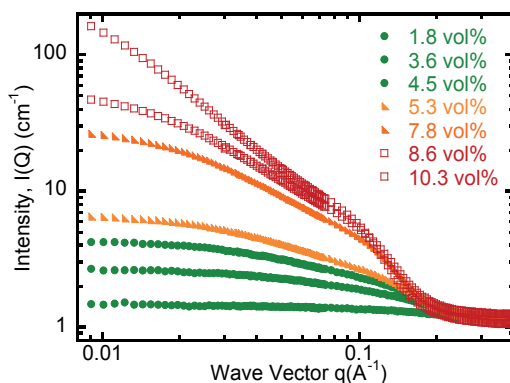
Figure 10. SANS curves for water-in-PAO nanoemulsion fluids for water volume concentration from 1.8 % to 10.3 %. Statistical error bars are smaller than the plotting symbols.
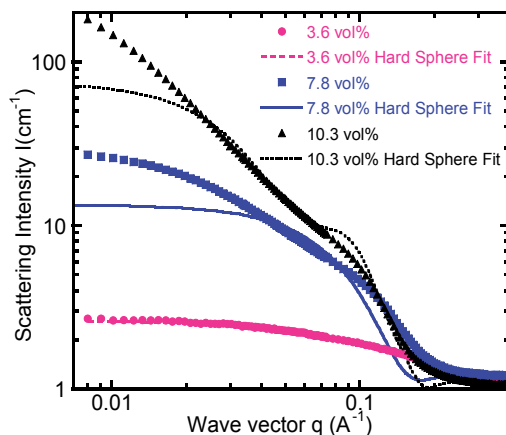
Figure 11. Small-angle neutron scattering curves for water-in-PAO nanoemulsion fluids (solid symbols) and hard sphere model curve fittings (colored lines).

Å, 25.6 Å, and 96 Å for water loading 1.8 vol. %, 3.6 vol. %, and 4.5 vol. %, respectively. For higher water concentration (i.e. 7.8 vol. % to 10.3 vol.%), the hard-sphere model does not fit well especially for scattering variable q less than 0.1 Å region, which suggests that those nanodroplets are not simply spherical.

Thus, a more comprehensive fitting model must be used to take into account of the structure change inside the water-in-PAO nanoemulsion fluids. Here, the three-region Guinier–Porod empirical model is used to accommodate the structural changes inside the system by fitting curves that are shown in Figure 12 [51, 54, 56, 68].

Generally, the scattering intensity is given by two contributions in the Guinier–Porod model:

$$I(Q) = \frac{G_2}{Q^{s_2}} \exp(\frac{-Q^2 R_{g2}^2}{3-s_2}) \text{ for } Q \le Q_2$$

$$I(Q) = \frac{G_1}{Q^{s_1}} \exp(\frac{-Q^2 R_{g1}^2}{3-s_1}) \text{ for } Q_2 \le Q \le Q_1 \tag{5}$$

$$I(Q) = \frac{D}{Q^d} \text{ for } Q \ge Q_1$$

Here $3-s_1$ and $3-s_2$ are the dimensionality parameters, and R_{g1} and R_{g2} are the radii of gyration for the short and overall size of the scattering object. This generalized Guinier–Porod model can be used to analyze SANS patterns for nonspherical objects. In general, for scattering objects with spherical symmetry $s_1=s_2=0$ and for cylindrical objects $s_2=0$ and $s_1=1$. For lamellae with equal width and length, one has $s_2=0$ and $s_1=2$.
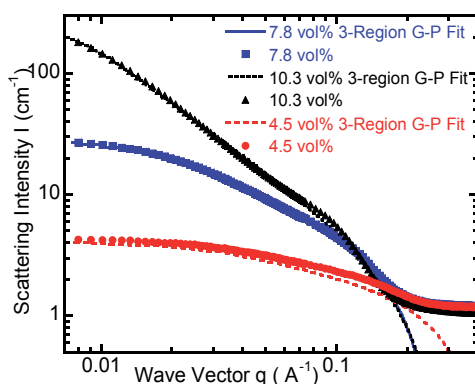
Figure 12. Small-angle neutron scattering curves for water-in-PAO nanoemulsion fluids (solid symbols) and three-region Guinier–Porod model curve fittings (colored lines).

Based on the fitting curves using the three-region Guinier–Porod model, there are two dimensionality parameters s_1 and s_2, plus R_{g2} and R_{g1} are the radii of gyration for the short and overall sizes of the scattering object. The fitted curves give $s_2=0.22$, $s_1=1.4$ and $R_{g2}=121$Å, $R_{g1}=4.6$Å for 10.3 vol. % water-in-PAO nanoemulsion fluids. For 7.8 % volume fraction water-in-PAO nanoemulsion fluid, $s_2=0.18$, $s_1=0.97$ and $R_{g2}=47.4$Å, $R_{g1}=5.2$Å. The dimensionality parameters suggest that those nanodroplets have a cylinder-like shape. So the SANS data confirm that there is an inner-structure variation with increasing water loading inside water-in-PAO nanoemulsion fluids. It is also noteworthy that the $s_2=0.04$ and $s_1=0.25$ is calculated for the 4.5 vol. % water-in-PAO nanoemulsion fluid and they can be approximated to $s_2 \approx 0$ and $s_1 \approx 0$, which agrees well with the interpretation of being spherical shape based on Hard Sphere model fitting. Note that for cylindrical droplets $R_{g2}^2 = \frac{L^2}{12} + \frac{R^2}{2}$, where L is the cylinder length and R is its radius and $R_{g1}^2 = \frac{R^2}{2}$.

3.3.2. Thermal conductivity of water-in-PAO nanoemulsion fluids

Figure 13 shows the thermal conductivity enhancement in water-in-PAO nanoemulsion fluids as a function of the loading of water from 0.47 % to 8.6 vol. %, in which the thermal conductivity linearly increases with higher water volume fraction and reaches a maximum of 16 % increase at 8.6 vol. % water.
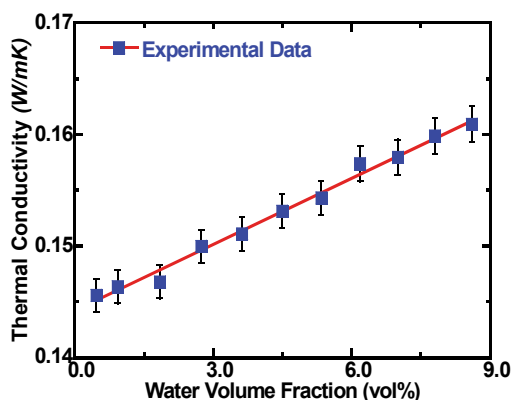
Figure 13. Thermal conductivity of water-in-PAO nanoemulsion fluids versus water volume fraction. The linear curve fit is shown for comparison.

3.3.3. Viscosity of water-in-PAO nanoemulsion fluids

The dynamic viscosity of water-in-PAO nanoemulsion fluids with different water volumetric concentrations is shown in Figure 14. All the water-in-PAO nanoemulsion fluids exhibit a shear-independent characteristic of Newtonian fluids. One unique phenomenon that can be seen in Figure 14 is that there is a maximum value in viscosity: it first increases with water concentration, reaches a maximum at 5.3 vol. %, and then decreases. This trend is different from the thermal conductivity shown in Figure 13 and the viscosity trend as observed in other nanoemulsion fluid systems. The maximum in viscosity can be attributed to the attraction force between droplets within the nanoemulsion fluids. The surfactant molecules become hydrated when more water is added inside and their counter ions are released into water which makes surfactants molecules and droplets charged oppositely so that the interdroplet attraction keeps increasing until the hydration process is complete. This may lead to a maximum viscosity in water-in-PAO nanoemulsion fluids as shown in Figure 14. It also coincides with the nonlinear inner structure change with increasing water concentration as seen in Figure 10.

3.3.4. Effective heat capacity of water-in-PAO nanoemulsion fluids

Similarly, the heat capacity of water-in-PAO nanoemulsion fluids was also investigated (shown in Figure 15). As shown in water-in-FC-72 nanoemulsion fluids, the water inside the water-in-PAO nanoemulsion fluids can increase the system's effective heat capacity through
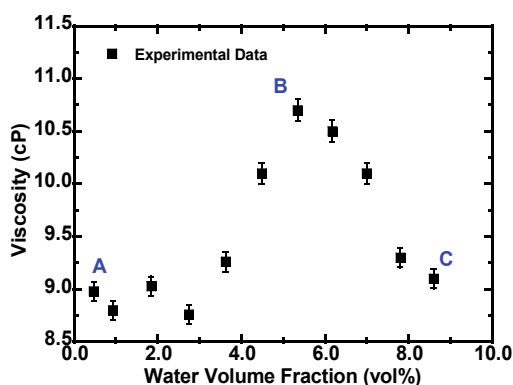
Figure 14. Dynamic viscosity of water-in-PAO nanoemulsion fluids versus volume fraction of water.

the high specific heat of water (i.e. C_{water}=4.2 J/g C, C_{PAO}=1.88 J/g C) and/or the latent heat of water (ΔH =334 J/g), depending on the operating temperature of the fluids.

DSC cyclic curves of water-in-PAO nanoemulsion fluids under different water loadings are shown in Figure 15. During the heating and cooling cycles, water nanodroplets undergo a melting–freezing transition in the nanoemulsion fluids. Interestingly, the presence of a single freezing peak in Figure 15 indicates a correspondence of the structural change with increasing water concentration (or water to surfactant molar ratio) as observed in our previous SANS measurement result: there is no obvious melting/freezing peak for water concentrations less than 4.5 vol. %, while the exothermic crystallization peak starts at around −20 °C when water concentration is higher or equal to 4.5 vol. %. When the water concentration is increased further above 8.6 vol. %, the freezing peak shifts to effect lower supercooling and peak values.
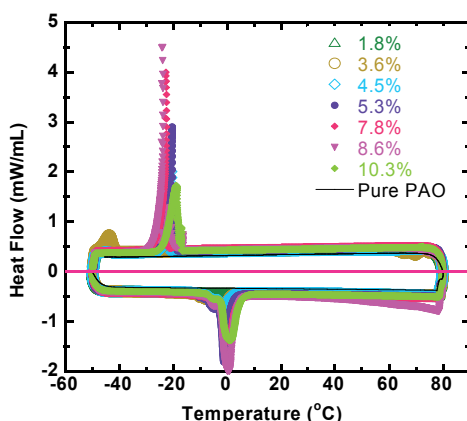
Figure 15. DSC cyclic curves of water-in-PAO nanoemulsion fluids for different water concentrations. Exothermal peaks are observed at −20 °C, corresponding to the freezing of water nanodroplets, while endothermal peaks are observed at 0 °C, corresponding to the melting of water nanodroplets.

To gain further insight into that, the specific heat of each sample is also calculated and summarized here in Table 2. The calculated H_f values of water-in-PAO nanoemulsions for different water concentrations from 5.3 to 8.6 vol. % are 17.7 and 28.724 J/g, respectively, in agreement with the measured results shown in Table 2, which are 26.72 J/g and 34.17 J/g, respectively. Based on the calculated values shown in Table 2, (1) the specific heat sharply increases from 9.8 J/g to 26.72 J/g when the water concentration is increased from 4.5 % to 5.3 vol. %; (2) the increase becomes moderate with higher water concentration; and (3) it decreases when the water concentration is higher than 8.6 vol. %. In addition to that, the freezing peak temperature is also decreased. All these occur to coincide with the structure transition with increasing water loading based on the SANS measurement.

Water % Fractions	Heat of Fusion (J/g)	Peak T (ºC)
10.3	28.97	−18.88
8.6	34.17	−23.97
7.8	31.27	−22.74
5.3	26.72	−20.32
4.5	9.808	−20.63
3.6	2.48	-45
1.8	2.18	0

Table 2. Specific heat of water-in-PAO nanoemulsion fluids

In addition to that, a total maximum heat capacity increase of 88 % is obtained in the 8.6 vol. % water/PAO nanoemulsion fluids: for a temperature increase from −20 to 0 ºC, 1 ml PAO absorbs 37.6 joules heat, and for the nanoemulsion containing 8.6 % water nanodroplets, the melting of ice nanoparticle absorbs 34 joules heat, it means that upon the melting of the ice nanoparticles in the nanoemulsion, the heat capacity of PAO has increased up by about 76 % in addition to the enhancement in heat capacity caused only by the addition of water without phase change (~12%).

4. Conclusions

The use of adding another material into thermal fluids has been emerged in recent years as a way to enhance the heat capacity and thermal conductivity of the base fluids simultaneously. A new type of nanostructured heat transfer fluids: nanoemulsion fluids are discussed in this chapter, such as ethanol-in-PAO, water-in-FC-72, and water-in-PAO nanoemulsion fluids. Many interesting properties have been reported in these nanoemulsion heat transfer fluids recently. The nanoemulsion heat transfer fluids can be formed by self-assembly and are thermodynamically stable. The self-assembled nanostructures have a significant effect on its macroscopic thermophysical properties which coincides with the structural characteristics

measured using SANS. In addition to that, the effective heat capacity of base fluid can also be greatly enhanced when those phase changeable nanodroplets undergo phase transition: the effective heat capacity of FC-72 by more than 200 % when those droplets undergo liquid–solid phase transition in water-in-FC-72 nanoemulsion fluids, and the effective heat capacity of PAO is increased by 80 % in water-in-PAO nanoemulsion fluids. The use of nanoemulsion fluids provides a means to increase the fluid conductivity and heat capacity simultaneously in the base fluids and their application in a wide variety of applications appears promising, but several critical issues remain to be solved in the future, for example, large subcooling or superheating during phase change due to lack of nucleation sites, and large viscosity increase due to the dispersed nanodroplets inside.

Acknowledgements

Author details

Bao Yang[2] and Jiajun Xu[1*]

*Address all correspondence to: jiajun.xu@udc.edu

1 Department of Mechanical Engineering, University of the District of Columbia, Washington DC, USA

2 Department of Mechanical Engineering, University of Maryland, College Park, MD, USA

References

[1] Eastman, J. A., Phillpot, S. R., Choi, S. U. S., and Keblinski, P., 2004, "Thermal transport in nanofluids," Annual Review of Materials Research, 34, pp. 219–246.

[2] Eastman, L. J., Choi, S. U. S., LI, S., and Thompson, L. J., 1997, "Enhanced thermal conductivity through development of nanofluids," Nanocrystalline and Nanocomposite Materials II.

[3] Inaba, H., 2000, "New challenge in advanced thermal energy transportation using functionally thermal fluids," International Journal of Thermal Sciences, 39(9–11), pp. 991–1003.

[4] Buongiorno, J., Venerus, D. C., Prabhat, N., McKrell, T., Townsend, J., Christianson, R., Tolmachev, Y. V., Keblinski, P., Hu, L.-W., Alvarado, J. L., Bang, I. C., Bishnoi, S. W., Bonetti, M., Botz, F., Cecere, A., Chang, Y., Chen, G., Chen, H., Chung, S. J., Chyu, M. K., Das, S. K., Di Paola, R., Ding, Y., Dubois, F., Dzido, G., Eapen, J., Escher, W., Funfschilling, D., Galand, Q., Gao, J., Gharagozloo, P. E., Goodson, K. E., Gutierrez, J. G., Hong, H., Horton, M., Hwang, K. S., Iorio, C. S., Jang, S. P., Jarzebski, A. B., Jiang, Y., Jin, L., Kabelac, S., Kamath, A., Kedzierski, M. A., Kieng, L. G., Kim, C., Kim, J.-H., Kim, S., Lee, S. H., Leong, K. C., Manna, I., Michel, B., Ni, R., Patel, H. E., Philip, J., Poulikakos, D., Reynaud, C., Savino, R., Singh, P. K., Song, P., Sundararajan, T., Timofeeva, E., Tritcak, T., Turanov, A. N., Van Vaerenbergh, S., Wen, D., Witharana, S., Yang, C., Yeh, W.-H., Zhao, X.-Z., and Zhou, S.-Q., 2009, "A benchmark study on the thermal conductivity of nanofluids," Journal of Applied Physics, 106(9).

[5] Zimparov, V., 2002, "Energy conservation through heat transfer enhancement techniques," International Journal of Energy Research, 26(7), pp. 675–696.

[6] Dewan, A., Mahanta, P., Raju, K. S., and Kumar, P. S., 2004, "Review of passive heat transfer augmentation techniques," Proceedings of the Institution of Mechanical Engineers Part A-Journal of Power and Energy, 218(A7), pp. 509–527.

[7] Boyd, R. D., 1985, "Subcooled flow boiling critical heat-flux (CHF) and its application to fusion energy components. 1. A review of fudamentals of CHF and related database," Fusion Technology, 7(1), pp. 7–30.

[8] Choi, S. U. S., Zhang, Z. G., Yu, W., Lockwood, F. E., and Grulke, E. A., 2001, "Anomalous thermal conductivity enhancement in nanotube suspensions," Applied Physics Letters, 79(14), pp. 2252–2254.

[9] Maxwell, J. C., 1904, "A treatise on electricity and magnetism," Oxford University Press, Cambridge, UK.

[10] Eastman, J. A., Choi, S. U. S., Li, S., Yu, W., and Thompson, L. J., 2001, "Anomalously increased effective thermal conductivities of ethylene glycol-based nanofluids containing copper nanoparticles," Applied Physics Letters, 78(6), pp. 718–720.

[11] Keblinski, P., Phillpot, S. R., Choi, S. U. S., and Eastman, J. A., 2002, "Mechanisms of heat flow in suspensions of nano-sized particles (nanofluids)," International Journal of Heat and Mass Transfer, 45(4), pp. 855–863.

[12] Prasher, R., Song, D., Wang, J. L., and Phelan, P., 2006, "Measurements of nanofluid viscosity and its implications for thermal applications," Applied Physics Letters, 89(13).

[13] Wang, X. Q., and Mujumdar, A. S., 2008, "A review on nanofluids - Part II: Experiments and applications," Brazilian Journal of Chemical Engineering, 25(4), pp. 631–648.

[14] Wang, X. Q., and Mujumdar, A. S., 2008, "A review on nanaofluids - Part I: Theoretical and numerical investigations," Brazilian Journal of Chemical Engineering, 25(4), pp. 613–630.

[15] Xu, J. J., Wu, C. W., and Yang, B., 2010, "Thermal- and phase-change characteristics of self-assembled ethanol/polyalphaolefin nanoemulsion fluids," Journal of Thermophysics and Heat Transfer, 24(1), pp. 208–211.

[16] Xu, J., Yang, B., and Hammouda, B., 2011, "Thermal conductivity and viscosity of self-assembled alcohol/polyalphaolefin nanoemulsion fluids," Nanoscale Research Letters, 6.

[17] Xu, J., Hammouda, B., and Yang, B., 2012, "Thermophysical properties and pool boiling characteristics of water in polyalphaolefin nanoemulsion fluids," ASME, Proceedings of ASME Micro/Nanoscale Heat & Mass Transfer International Conference 2012.

[18] Xu, J., and Yang, B., 2012, "Novel heat transfer fluids: Self-assembled nanoemulsion fluids," Nanotechnology, D. J. N. Govil, ed., Studium Press LLC.

[19] Yang, B., and Han, Z. H., 2006, "Thermal conductivity enhancement in water-in-FC72 nanoemulsion fluids," Applied Physics Letters, 88(26).

[20] Han, Z. H., Cao, F. Y., and Yang, B., 2008, "Synthesis and thermal characterization of phase-changeable indium/polyalphaolefin nanofluids," Applied Physics Letters, 92(24).

[21] Han, Z. H., and Yang, B., 2008, "Thermophysical characteristics of water-in-FC72 nanoemulsion fluids," Applied Physics Letters, 92(1).

[22] Han, Z. H., Yang, B., Qi, Y., and Cumings, J., 2011, "Synthesis of low-melting-point metallic nanoparticles with an ultrasonic nanoemulsion method," Ultrasonics, 51(4), pp. 485–488.

[23] Kumar, P., and Mittal, K. L., 1999, Handbook of microemulsion science and technology, New York: Marcel Dekker.

[24] Rosele, M. L., "Boiling of dilute emulsions," PhD Dissertation, University of Minnesota.

[25] Bulanov, N. V., Skripov, V. P., and Khmylnin, V. A., 1984, "Heat transfer to emulsion with superheating of its disperse phase," Journal of Engineering Physics, pp. 1–3.

[26] Bulanov, N. V., Skripov, V. P., and Khmylnin, V. A., 1993, "Heat transfer to tmulsion with a low-boiling disperse phase," Heat Transfer Research, pp. 786–789.

[27] Bulanov, N. V., 2001, "An analysis of the heat flux density under conditions of boiling internal phase of emulsion," High Temperature, 39(3), pp. 462–469.

[28] Bulanov, N. V., and Gasanov, B. M., 2005, "Experimental setup for studying the chain activation of low-temperature boiling sites in superheated liquid droplets," Colloid Journal, 67(5), pp. 531–536.

[29] Bulanov, N. V., Gasanov, B. M., and Turchaninova, E. A., 2006, "Results of experimental investigation of heat transfer with emulsions with low-boiling disperse phase," High Temperature, 44(2), pp. 267–282.

[30] Bulanov, N. V., and Gasanov, B. M., 2008, "Peculiarities of boiling of emulsions with a low-boiling disperse phase," International Journal of Heat and Mass Transfer, 51(7–8), pp. 1628–1632.

[31] Lunde, D. M., 2011, "Boiling dilute emulsions on a heated strip," MS thesis, University of Minnesota.

[32] Chen, S. J., Evans, D. F., and Ninham, B. W., 1984, "Properties and structure of 3-component ionic microemulsions," Journal of Physical Chemistry, 88(8), pp. 1631–1634.

[33] Ruckenstein, E., 1986, "The surface of tension, the natural radius, and the interfacial-tension in the thermodynamics of microemulsions," Journal of Colloid and Interface Science, 114(1), pp. 173–179.

[34] Siano, D. B., Bock, J., Myer, P., and Russel, W. B., 1987, "Thermodynamics and hydrodynamics of a nonionic microemulsion," Colloids and Surfaces, 26, pp. 171–190.

[35] Rosano, H. L., Cavallo, J. L., Chang, D. L., and Whittam, J. H., 1988, "Microemulsions - A commentary on their preparation," Journal of the Society of Cosmetic Chemists, 39(3), pp. 201–209.

[36] Chen, Z. Q., Chen, L. D., Hao, C., and Zhang, C. Z., 1990, "Thermodynamics of microemulsion. 1. The effect of alkyl chain-length of alkyl aromatics," Acta Chimica Sinica, 48(6), pp. 528–533.

[37] Moulik, S. P., Das, M. L., Bhattacharya, P. K., and Das, A. R., 1992, "Thermodynamics of microemulsion formation. 1. Enthalpy of solution of water in binary (triton-X 100 + butanol) and ternary (heptane + triton-X 100 + butanol) mixtures and heat-capacity of the resulting systems," Langmuir, 8(9), pp. 2135–2139.

[38] Moulik, S. P., and Ray, S., 1994, "Thermodynamics of clustering of droplets in water/AOT/heptane microemulsion," Pure and Applied Chemistry, 66(3), pp. 521–525.

[39] Ray, S., Bisal, S. R., and Moulik, S. P., 1994, "Thermodynamics of microemulsion formation. 2. Enthalpy of solution of water in binary-mixtures of aerosol-OT and heptane and heat-capacity of the resulting systems," Langmuir, 10(8), pp. 2507–2510.

[40] Strey, R., 1994, "Microemulsion and interfacial curvature," Colloid and Polymer Science, 272(8), pp. 1005–1019.

[41] Bergenholtz, J., Romagnoli, A. A., and Wagner, N. J., 1995, "Viscosity, microstructure, and interparticle potential of AOT/H$_2$O/N-decane inverse microemulsions," Langmuir, 11(5), pp. 1559–1570.

[42] Mukherjee, K., Mukherjee, D. C., and Moulik, S. P., 1997, "Thermodynamics of microemulsion formation. 3. Enthalpies of solution of water in chloroform as well as chloroform in water aided by cationic, anionic, and nonionic surfactants," Journal of Colloid and Interface Science, 187(2), pp. 327–333.

[43] Talegaonkar, S., Azeem, A., Ahmad, F. J., Khar, R. K., Pathan, S. A., and Khan, Z. I., 2008, "Microemulsions: a novel approach to enhanced drug delivery," Recent Patents on Drug Delivery & Formulation, 2(3), pp. 238–257.

[44] Wu, C., Cho, T. J., Xu, J., Lee, D., Yang, B., and Zachariah, M. R., 2010, "Effect of nanoparticle clustering on the effective thermal conductivity of concentrated silica colloids," Physical Review E, 81(1).

[45] Tyndall, J., 1868, "On the blue colour of the sky, the polarization of sky-light, and on the polarization of light by cloudy matter generally," Proceedings of the Royal Society of London, p. 223.

[46] He, G. S., Qin, H.-Y., and Zheng, Q., 2009, "Rayleigh, Mie, and Tyndall scatterings of polystyrene microspheres in water: Wavelength, size, and angle dependences," Journal of Applied Physics, 105(2).

[47] Haque, O., and Scamehorn, J. F., 1986, "Thermodynamics of microemulsion formation by mixtures of anionic and nonionic surfactants," Journal of Dispersion Science and Technology, 7(2), pp. 129–157.

[48] Mukhopadhyay, L., Mitra, N., Bhattacharya, P. K., and Moulik, S. P., 1997, "Thermodynamics of formation of biological microemulsion (with cinnamic alcohol, aerosol OT, Tween 20, and water) and kinetics of alkaline fading of crystal violet in them," Journal of Colloid and Interface Science, 186(1), pp. 1–8.

[49] De, M., Bhattacharya, S. C., Panda, A. K., and Moulik, S. P., 2009, "Interfacial behavior, structure, and thermodynamics of water in oil microemulsion formation in relation to the variation of surfactant head group and cosurfactant," Journal of Dispersion Science and Technology, 30(9), pp. 1262–1272.

[50] Moulik, S. P., and Paul, B. K., 1998, "Structure, dynamics and transport properties of microemulsions," Advances in Colloid and Interface Science, 78(2), pp. 99–195.

[51] Hammouda, B., Krueger, S., and Glinka, C. J., 1993, "Small-angle neutron-scattering at the national-institute-of-standards-and-technology," Journal of Research of the National Institute of Standards and Technology, 98(1), pp. 31–46.

[52] Chen, S. H., 1986, "Small-angle neutron-scattering studies of the structure and interaction in micellar and microemulsion systems," Annual Review of Physical Chemistry, 37, pp. 351–399.

[53] Gradzielski, M., and Langevin, D., 1996, "Small-angle neutron scattering experiments on microemulsion droplets: Relation to the bending elasticity of the amphiphilic film," Journal of Molecular Structure, 383(1–3), pp. 145–156.

[54] Hammouda, B., 2010, "SANS from polymers-review of the recent literature," Polymer Reviews, 50(1), pp. 14–39.

[55] Howe, A. M., Toprakcioglu, C., Dore, J. C., and Robinson, B. H., 1986, "Small-angle neutron-scattering studies of microemulsions stabilized by aerosel-OT. 3. The effect of addictives on phase-stability and droplet structure," Journal of the Chemical Society-Faraday Transactions I, 82, pp. 2411–2422.

[56] Marszalek, J., Pojman, J. A., and Page, K. A., 2008, "Neutron scattering study of the structural change induced by photopolymerization of AOT/D(2)O/sodecyl acrylate inverse microemulsions," Langmuir, 24(23), pp. 13694–13700.

[57] Nagao, M., Seto, H., Shibayama, M., and Yamada, N. L., 2003, "Small-angle neutron scattering study of droplet density dependence of the water-in-oil droplet structure in a ternary microemulsion," Journal of Applied Crystallography, 36, pp. 602–606.

[58] Wang, X.-Q., and Mujumdar, A. S., 2007, "Heat transfer characteristics of nanofluids: a review," International Journal of Thermal Sciences, 46(1), pp. 1–19.

[59] Wang, L. Q., and Wei, X. H., 2009, "Nanofluids: synthesis, heat conduction, and extension," Journal of Heat Transfer-Transactions of the Asme, 131(3).

[60] Ozerinc, S., Kakac, S., and Yazicioglu, A. G., 2010, "Enhanced thermal conductivity of nanofluids: a state-of-the-art review," Microfluidics and Nanofluidics, 8(2), pp. 145–170.

[61] Philip, J., and Shima, P. D., 2012, "Thermal properties of nanofluids," Advances in Colloid and Interface Science, 183, pp. 30–45.

[62] Cahill, D. G., 1990, "Thermal-conductivity measurement from 30-K to 750-K - The 3-omega method," Review of Scientific Instruments, 61(2), pp. 802–808.

[63] Yang, B., 2008, "Thermal conductivity equations based on Brownian motion in suspensions of nanoparticles (nanofluids)," Journal of Heat Transfer-Transactions of the Asme, 130(4).

[64] Touloukian, Y. S., Liley, P. E., and Saxena, S. C., 1970, "Thermal conductivity for non-metallic liquids & gases," Washiongton: IFI/PLENUM, Thermophysical Properties of Matters.

[65] 2002, "Synfluid PAO databook," Chveron Philips Chemical LP, *Synfluid PAO Databook*.

[66] 3M, "Fluorinert™ electronic liquid FC-72 product information."

[67] Evans, W., Fish, J., and Keblinski, P., 2006, "Role of Brownian motion hydrodynamics on nanofluid thermal conductivity," Applied Physics Letters, 88(9).

[68] Hammouda, B., 2010, "A new Guinier-Porod model," Journal of Applied Crystallography, 43, pp. 716–719.

[69] Mulligan, J. C., Colvin, D. P., and Bryant, Y. G., 1996, "Microencapsulated phase-change material suspensions for heat transfer in spacecraft thermal systems," Journal of Spacecraft and Rockets, 33(2), pp. 278–284.

Application of Neutron Scattering in Amino Acid Crystals – Structural and Dynamical Information

Paulo T.C. Freire, José E.M. Pereira and Heloisa N. Bordallo

Additional information is available at the end of the chapter

Abstract

In this work results of neutron powder diffraction and inelastic neutron scattering on aliphatic amino acid (L-alanine, L-valine and L-leucine) crystals are presented. The study allows inferring important informations about both the stability of the structures and the dynamics of phase transitions. In particular, it was possible to compare the behavior of different amino acids and to infer that changes in the mean-square displacements observed for two deuterated forms of L-alanine $ND_3^+ - C_2H_4 - CO_2^-$ and $NH_3^+ - C_2D_4 - CO_2^-$ are due to a structural rearrangement related to thermally activated amplitude reorientation of NH_3^+ and CO_2^-. Conformation changes in L-valine and L-leucine related to the phase transition are also discussed.

Keywords: Amino acid crystal, neutron diffraction, inelastic neutron scattering

1. Introduction

Amino acids are the basic blocks of proteins of all living beings, but are also found alone in the cytoplasm of several cells. They were produced and selected since the beginning of life in the Earth, although it is not possible to rule out an extraterrestrial origin. Due to the fact that they appear forming zwitterion structure (involving simultaneously the NH_3^+ and the CO_2^- groups) in both aqueous environment and in solid state phase, amino acids have been extensively studied in the last years. The researches deal mainly with spectroscopic and structural properties, giving special attention to the hydrogen bonds between the amino acid and the water molecules in the aqueous solution and among amino acids, when the material is found in crystalline structures [1 – 4].

From the spectroscopic point of view, amino acids have been investigated using mainly Raman spectroscopy [4 – 6], where information about optical phonons is readily obtained. Based on

such studies it has been suggested that amino acid crystals can present structural instabilities at low temperatures or high pressures. Regarding their structural properties, X-rays [7, 8] and neutron scattering diffraction data [5] have been useful in providing a picture of the origin of the stabilities of their crystal structures as well as the role played by the hydrogen bonds.

In particular, it was possible to gain information on the modifications of the hydrogen bonds studying different deuterated of amino acids samples using inelastic neutron scattering [9 – 11]. From these data the elastic intensity can be expressed as a function of temperature such as $I(T) = I(0).exp[-Q^2 u(T)^2]$, where Q is the scattering vector and $u(T)$ represents the mean-square displacement of the scattering nuclei. Additionally, if a dynamic transition occurs, one can observe a change in the slope of the observed $u(T)^2$. Furthermore, selective deuteration allows tackling changes in the mean-square displacements of particular groups, such as the torsion vibration of CH_3^+ or the torsion of NH_3^+ group. Inelastic neutron scattering combined to selective deuteration can also be used to highlight the modes of particular molecular groups by comparing the spectra of the selected deuterated groups [12].

The objective of this chapter is to present a quick review of neutron powder diffraction and inelastic neutron scattering results on various aliphatic amino acid crystals. These investigations allowed to compare the behavior of different aliphatic amino acids (alanine, valine and leucine), in particular, looking at their vibrational and dynamical properties. For L-alanine, for example, combining neutron diffraction to incoherent elastic neutron scattering measurements allowed us to infer that changes in the mean-square displacements observed for two deuterated forms of L-alanine: (i) $ND_3^+ – C_2H_4 – CO_2^-$ and (ii) $NH_3^+ – C_2D_4 – CO_2^-$ are due to a structural rearrangement related to thermally activated amplitude reorientation of NH_3^+ and CO_2^-.

2. Structural and vibrational anomalies observed in selected amino acids

Many results on the vibrational properties of amino acid crystals are known. From these studies one has constructed an interesting picture about the behavior of the crystals in a huge range of temperature and/or pressure. L-alanine, the simplest chiral amino acid, is an example where surprising aspects of the vibrational properties stand. Among these aspects it is possible to cite some: the intriguing step-wise evolution of the wavenumber of some bands [13], the unconventional increasing of the c lattice parameter when L-alanine is cooled [14], and the localization of vibrational states as revealed by the variation of intensities of the low wave-number modes at 41 and 49 cm^{-1} [15]. Simultaneously to the increasing of the c lattice parameter a progressive conformational change of the NH_3^+ zwitterion, as well as a strong dynamic Jahn-Teller-like effect due the coupling between NH_3^+ charge and the lattice were observed [13]. These results can be interpreted as consequence of the N – H stretching self-trapped states related to the N – H...O hydrogen bonds directed along the head-to-tail chains of the zwitterions. According to Ref. [16] these self-trapped states should be associated with some of the anomalies reported for L-alanine. The behavior of the intensity of one lattice mode was realized as consequence of the response of one N – H...O hydrogen bond to respond to the changes in the interaction of the nitrogen and oxygen atoms with other atoms forming different hydrogen

bonds. In fact, it is believed that one can assume that hydrogen bonds in chains of zwitterion have diverse properties from those between the chains and the variation of temperature should produce subtle rearrangement of the hydrogen bond network, explaining the existence of anomalies at low temperature [16]. Under high pressure, L-alanine also shows intriguing aspects. For instance, Raman spectroscopy studies have indicated the occurrence of a phase transition at ~ 2.3 GPa [17], which was later confirmed by X-ray diffraction measurements [18]. A new interpretation, however, has indicated that the modifications about 2 GPa might also be understood as a conformation change of the NH_3^+ group [19, 20].

The above considerations for the chiral L-alanine can be extended to encompass the racemic material. DL-alanine seems to be stable at low temperature, presenting no evidence of a solid-solid phase transition from room temperature down to 15 K [21]. However, although no modification in the spectral region of the lattice modes – normally between 30 and 200 cm^{-1} – was detected, certain changes in the internal mode region of the spectrum were noted. These changes can be understood as slight conformational modification of the molecule on cooling. In fact, the rocking vibration of CO_2^- presents an unconventional behavior, *i.e.*, variation of the wavenumber in step-like shape at specific temperatures. In relation to this, it is important to mention that the data obtained using polarized Raman shows that the main change associated with hydrogen bonds take place along the x-axis direction, instead of the bonds along the z-axis. This behavior was also simultaneously reported in the work presented in Ref. [16] for the chiral partner of alanine crystal.

Crystalline L-leucine, another aliphatic amino acid, presents an interesting behavior when submitted to temperature variation between 300 and 400 K. As shown by Raman spectroscopic measurements, the material undergoes a phase transition at ~ 353 K. One possible explanation for the occurrence of such a modification is the appearance of transverse optical (TO) modes at high temperature. Such a vibrational aspect can be translated to the structural language if one assumes that the room temperature monoclinic structure C_2 change to a monoclinic C_s structure [22]. In other words, from the point of view of the spectroscopic scrutiny the $C_2 \rightarrow C_s$ phase transition is a viable path.

Obviously, other questions are relevant as the interaction of amino acid molecules with metal ions. Ions can be present in the living beings as participating of biochemistry processes or nosy hazard agents. Additionally, from a technological point of view it is important to know the influence of metal doping on several crystals with the objective to modify some of their properties, including modification of the crystal habit, thermal conductivity, etc. Analysis of Raman spectroscopy and X-ray diffraction measurements suggested, for example, Ni ions occupy interstitial crystallographic sites in the lattice of L-histidine hydrochloride monohydrate crystal [23]. This specific position is the same occupied by Cu ions in the L-histidine.HCl.H$_2$O crystal; the stabilization of the ion – amino acid molecule could be achieved by the interaction between the metal ion and the NH_3^+ group. On cooling, due to the packing of structure, the interaction ion – amino acid is intensified. To understand the interaction of metal ion and amino acid (representing active part of proteins and peptides) is a task with relevance to biochemistry science.

From this résumé one realizes that many changes might occur when crystalline amino acids are submitted to different pressure and/or temperature conditions. Therefore, one question comes to mind: how the hydrogen bonds connecting the molecules in the solid state phase adapt themselves to the new phases in these amino acids? This question will be addressed in the next sections, where it is explained how neutron diffraction and inelastic neutron scattering experiments can bring unique information to this problem.

3. Basic theory

Postulated by Rutherford in 1920 and discovered by J. Chadwick in 1932, neutrons are non-charged subatomic particles with mass rather close to that of the proton $m_n = 1.675.10^{-27}$ kg, magnetic moment equals to - 1.913 μ_b and a nuclear spin $s = \frac{1}{2}$, which are important and unique properties for developing the theory of neutron scattering [24].

Since neutrons are non-charged particles, their interactions with matter, both nuclear and magnetic, are short range; therefore neutrons can penetrate deeply into matter. This enables us to study the structure and dynamics of materials under very precise environmental conditions. Neutrons can be described using either classical mechanics, with momentum $\vec{p} = m\vec{v}$, where m is the neutron mass and $\vec{v}$ is its velocity, or quantum mechanics, with momentum $\vec{p} = \hbar\vec{k}$, with $|\vec{k}| = \frac{2\pi}{\lambda}$ defining the wave vector of the neutron and λ its associated wavelength.

This also implies that neutron scattering processes are based on the analysis of momentum and energy transfer, which may occur due to the interactions between neutrons and matter. The momentum transfer vector or the scattering vector, $\vec{Q}$, is defined as the vector difference between the incoming and scattered wave vectors as in Eq. (1).

$$\vec{Q} = \vec{k}_i - \vec{k}_f , \tag{1}$$

while the variation in the neutron momentum is given by Eq. (2):

$$\hbar\vec{Q} = \hbar(\vec{k}_i - \vec{k}_f), \tag{2}$$

The corresponding neutron energy E can be described as described by Eq. (3):

$$E = \frac{p^2}{2m} = \frac{1}{2}mv^2 = \frac{\hbar^2}{2m\lambda} = \frac{\hbar^2 k^2}{2m} , \tag{3}$$

where $h = 2\pi\hbar = 6.626.10^{-34}$J.s is the Planck's constant. Thus, variation of the energy ($\hbar\omega$) measured in a neutron scattering experiment is given by Eq. (4):

$$\hbar\omega = E_i - E_f = \frac{\hbar^2}{2m}\left(k_i^2 - k_f^2\right). \tag{4}$$

During the scattering process, elastic scattering occurs when the variation of energy between neutron and the sample is zero. On the other hand, when this variation is different from zero, the scattering processes is called inelastic.

In a typical neutron experiment the collected information is related to the partial differential cross-section, $d^2\sigma/(dEd\Omega)$, given by Eq. (5), according to Ref. [25]:

$$\frac{d^2\sigma}{d\Omega dE_f} = \frac{k_f}{k_i}\frac{1}{\hbar}\left[b_{coh}^2 S_{coh}\left(\vec{Q},\omega\right) + b_{inc}^2 S_{inc}\left(\vec{Q},\omega\right)\right], \tag{5}$$

where $S_{coh}(\vec{Q}, \omega)$ and $S_{inc}(\vec{Q}, \omega)$ are the so-called coherent and incoherent scattering functions. These functions are Fourier transformations of the van Hove correlation functions $G(\vec{r}, t)$, which can be described as the probability for an atom at the origin at time 0, to also be found within the unit volume at a position $\vec{r}$ at a time t.

The probability of interactions between the neutrons and the atoms is a characteristic of each isotope and described by two terms: coherent and incoherent cross sections (σ_{coh} and σ_{inc}), as shown in Table 1. The cross section is related to the coherent (b_{coh}) and incoherent (b_{inc}) scattering length by the following relation: $\sigma = 4\pi b^2$. The high σ_{inc} value of ^{1}H in comparison to the other elements allows the assignment of the vibrations related to hydrogen atoms. On the other, the high value of the coherent cross section of ^{2}D when compared to ^{1}H allows to locate the hydrogen atom by using deuteration.

	^{1}H	^{2}D	C	O	N	Cl
σ_{coh}	1.76	5.59	5.55	4.23	11.0	11.5
σ_{inc}	80.27	2.05	<0.01	<0.01	0.50	5.30

Table 1. Coherent (σ_{coh}) and incoherent (σ_{inc}) cross-sections in 10^{-24} cm^2 for selected elements and isotopes [26].

For crystalline matrices, the coherent scattering function in Eq. (5) is written as given in Eq. (6):

$$S_{coh} = \left|F(\vec{Q})\right|^2 \delta(\omega)\sum_{\frac{\vec{G}}{2\pi}}\delta\left(\vec{Q}-\vec{G}\right)$$

$$+\sum_{s,\vec{q}}\left|F\left(s,\vec{q}\right)\right|^2\frac{\left\langle n(\omega)\left|+\frac{1}{2}\pm\frac{1}{2}\right.\right\rangle}{\omega}\delta(\omega\mp\omega_{s,\vec{q}})\sum_{\frac{\vec{G}}{2\pi}}\delta\left(\vec{Q}+\vec{q}-\vec{G}\right), \tag{6}$$

where the first term represents Bragg scattering and in a diffraction experiment the Bragg's Law is satisfied:

$$n\lambda = 2d\sin\theta, \tag{7}$$

here n is a positive integer and λ is the wavelength of incident wave and the angle θ is defined as the angle between the incoming ray and the diffraction atomic plane.

The second term in Eq. (6) describes collective atomic motions (phonons), where $\vec{q}$ is the wave vector of the collective atomic motion and s an index that specifies the various modes of such collective motions.

Contributions from single particle motion are described by $S_{inc}(\vec{Q}, \omega)$ as given by Eq. (8):

$$S_{inc}\left(\vec{Q},\omega\right) = S_{inc}^{trans}\left(\vec{Q},\omega\right) \otimes S_{inc}^{rot}\left(\vec{Q},\omega\right) \otimes S_{inc}^{vib}\left(\vec{Q},\omega\right), \tag{8}$$

In Eq. (8) the terms describe contributions from the translational, rotational and vibrational modes, respectively.

4. Experimental details

In order to obtain the results presented in this chapter, a series of facilities were utilized. Neutron powder diffraction (NPD) experiments were carried out using the powder diffractometers E9 located at the Helmholtz-Zentrum Berlin für Materialien und Energie (Berlin, Germany) and D2b at the Institut Laue-Langevin (Grenoble, France). Such equipments allowed the determination and refinement of crystal structures with very high resolution, furnishing lattice constants and internal atomic coordinates with great precision. Through the experiments with temperature variation the data were analyzed using a crystallographic model from Ref. [27] Due to the thermal diffuse scattering contribution, attention was paid to the modeling of the background.

Incoherent elastic neutron scattering measurements were carried out using the time-of-flight spectrometer NEAT at the Helmholtz-Zentrum Berlin für Materialien und Energie as well as the backscattering instrument IN10 located at the Institut Laue-Langevin.

The analysis of the evolution of the elastic line centered around $E = 0$, (energy resolution, ΔE = 100 μeV (NEAT) or 1 μeV (IN10)) as a function of temperature gives information about the mean square displacement of the atoms around their equilibrium positions or, in very broad terms, describes the crystal flexibility. On the other hand, the inelastic part of the spectra gives information on the lattice phonons as well as on the inter-molecular vibrations of the samples. The obtained information is complementary to infrared (IR) and Raman scattering (RS).

5. Looking inside amino acid crystals

In relation to amino acid crystals there is a pivotal point to be considered when using neutron spectroscopy or neutron diffraction: the hydrogen bonds that connect the various molecules together in the crystal structure. In this chapter results on crystals of the amino acids L-alanine, L-valine and L-leucine are discussed.

The first discussion will furnish a picture on the simplest chiral amino acid, L-alanine. Selective deuteration of L-alanine were analyzed: (i) C_2H_4-(ND_3^+)-CO_2^-, Ala-ND3; (ii) C_2D_4-(NH_3^+)-CO_2^-, Ala-CD4; (iii) C_2D_4-(ND_3^+)-CO_2^-, Ala-D7. L-alanine crystallizes in an orthorhombic structure with four molecules per unit cell in a $P2_12_12_1$ space group. The molecules are distributed spatially as head-to-tail chains along the crystallographic c-axis, presenting a complex three dimensional network of hydrogen bonds. Here we recall that the c-axis a stepwise change of the size parameter on cooling. Combining inelastic neutron scattering (INS) and neutron powder diffraction (NPD) is possible to study the relationship between the local dynamics of NH_3, CO_2 and CH_3 and to gain insights about the behavior of hydrogen bonds.

Figure 1 presents the inelastic neutron scattering spectra of (a) Ala-ND3 and (b) Ala-CD4 for several temperatures in the energy range from 0 to 70 meV. Data were obtained using the NEAT spectrometer. It is possible to observe several normal modes: lattice modes below 20 meV and other modes such as torsion of CO_2 group, $\tau(CO_2^-)$, torsion of NH_3, $\tau(NH_3^+)$, and torsion of CH_3, $\tau(CH_3)$, as specified in the figure. It is interesting to observe the peak located ~ 60 meV that is associated with $\tau(NH_3^+)$. The width of this peak can be understood as consequence of the anharmonicity of the hydrogen bonds because all three protons participate of N–H...O hydrogen bonds. The influence of anharmonicity is not restrict to the torsion of the ammonia group; as it can be noted in Figure 1 the large peaks associated with the lattice modes that involves bending and stretching of hydrogen bonds can be ascribed to the same effect. Additionally, if one plots the energy of $\tau(CO_2^-)$ mode in Ala-ND3 (not shown in Figure 1) as a function of temperature, one notes a discontinuity between 150 and 200 K. Such a discontinuity coincides with a discontinuity of the wavenumber of a band associated with $\tau(CO_2^-)$ in the Raman spectrum at temperatures in the same interval.

Figure 2 presents the neutron diffraction patterns of Ala-CD4 for two different temperatures. The measurements were obtained with a neutron wavelength of 2.8060 Å. Impressively, at T = 100 K, it is observed a Bragg peak at $\sim 2\theta = 78°$ that does not belong to the $P2_12_12_1$ orthorhombic structure. In the attempt to index this peak authors were guided to assume a primitive orthorhombic cell with the a-axis with double size [11]. It is remembered that the non-deuterated L-alanine presents any strong modification in its lattice parameter, although the crystal itself shows a series of anomalies at low temperatures. As a consequence, the result presented in Figure 2 suggests that the partial deuteration of L-alanine induces a solid-solid phase transition. Interestingly such a phase transition can be seen as an enhancement of an anomaly observed in the non-deuterated partner at T ~ 260 K [13]. The doubling of the a-lattice parameter involves changes in the two hydrogen bonds represented in Figure 3 and a rearrangement of the whole molecule. Between 270 and 250 K, a decreasing in the D(2)...O(2)
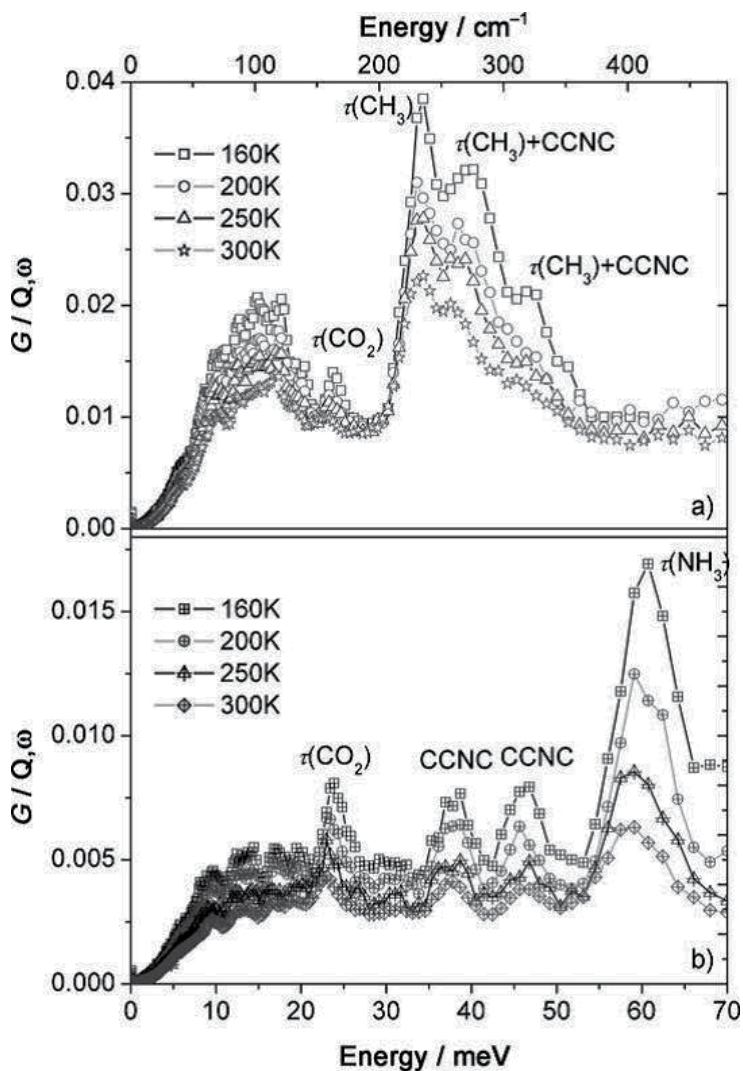
Figure 1. Inelastic neutron scattering spectra at various temperatures for (a) Ala-ND3 and (b) Ala-CD4. The assignment of the main modes is given [11].

bond is observed and an impressive anomaly between 250 and 100 K. On the other hand, the D(1)...O(1) bond becomes longer when temperature is lower than 100 K.

Figure 4 presents $<u_H(T)^2>$ of C_2H_4-(ND_3^+)-CO_2^- and C_2D_4-(NH_3^+)-CO_2^-, where $u_H(T)$ represents the mean-square displacement of the scattering nuclei. Here, as specified previously, $I(T) = I(0).exp[-Q^2 u(T)^2]$ is the elastic intensity expressed as a function of temperature (the temperature dependence is embedded in u_H). In fact, once the elastic intensity has been experimentally determined, one obtain $u(T)^2$. As it is expected, due the large incoherent cross section of the hydrogen, $u(T)$ is supposed originated only the motion of H atoms. Another aspect to be
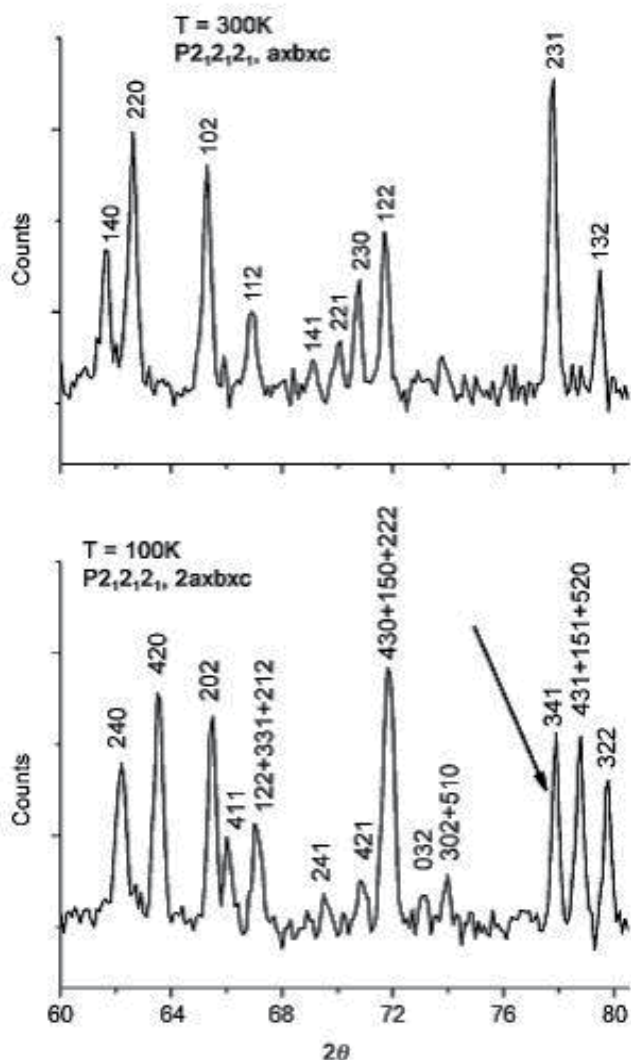
Figure 2. Neutron diffraction patterns of C_2D_4-(NH_3^+)-CO_2^- at T=300 K and T=100 K measured with the E9 diffractometer at Hahn-Meitner-Institut. The arrow indicates the peak that could not be indexed with the original $P2_12_12_1$ structure [11].

considered is the following: change in the slope of $u(T)^2$ indicates a dynamical transition in the material. From the Figure 4 one observe that at 160 K and at 220 K there are clear changes in the slop, that can be interpreted as a phase transition or, at least, to a structural rearrangement. Such rearrangement should be probably related to thermally activated large-amplitude reorientations of both CH_3 and NH_3 smithereens of the L-alanine molecule.

The previous paragraphs showed that in the study of partially deuterated L-alanine crystal, the H(1)...O(1) hydrogen bond length increases below 100 K on decreasing temperature and
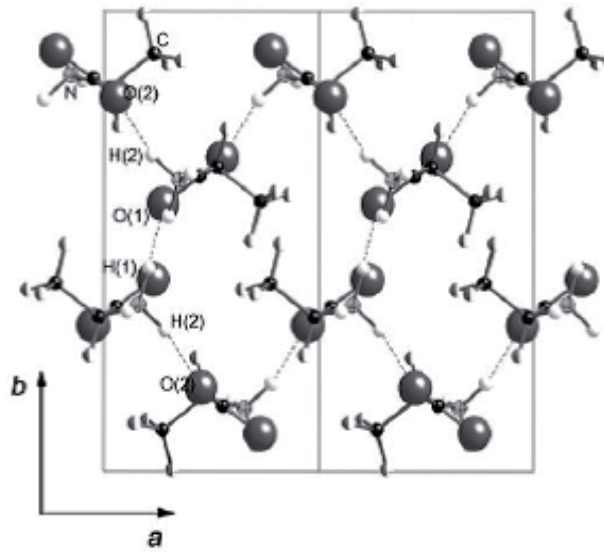
Figure 3. Representation of the crystal structure of L-alanine showing the *ab*-plane. The two hydrogen bonds modifies at low temperature are shown [11].
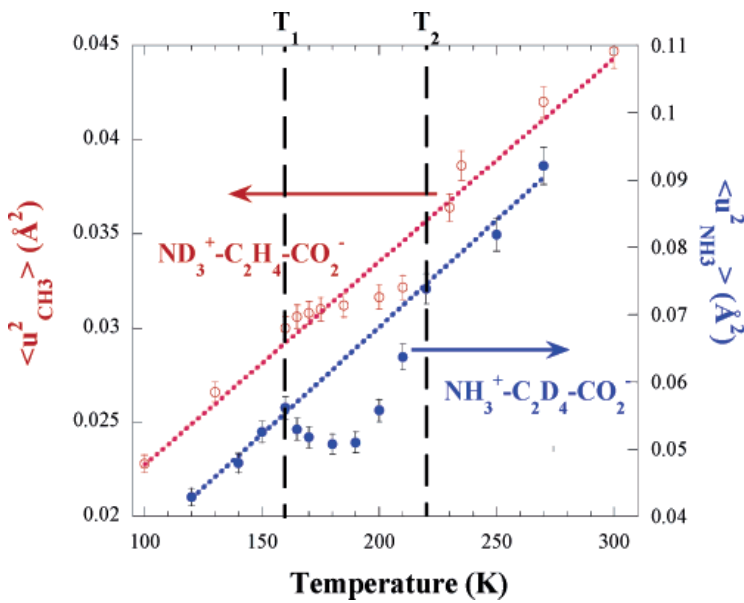
Figure 4. Mean-square dependence from the normalized elastic intensity as a function of temperature. The left scale and open circles represent data for C_2H_4-(ND_3^+)-CO_2^- and the right scale and full circles represent data for C_2D_4-(NH_3^+)-CO_2^- [10].

the H(2)...O(2) length presents an anomaly between 100 and 250 K. What about the behavior of fully deuterated L-alanine under the scrutiny of INS and NPD techniques? Roughly

speaking, deuteration, or isotopic substitution, D → H, produces strong modification in the length of the hydrogen bond. This change generally affects the tunneling rates and the motional properties of the molecules, an effect known as Ubbelohde effect; it is observed in crystals with complex network of hydrogen bonds and even in isolated pair of this type of bond.

Figure 5 presents the temperature dependence of several parameters related to the hydrogen bonds for the fully deuterated L-alanine crystal, C_2D_4-(ND_3^+)-CO_2^-, Ala-D7. Several anomalies are described in the next paragraphs.

From the measurement it is possible to realize that the N-D(3) distance remains almost constant between 10 and 270 K. On the other hand, the N-D(1) distance remains constant only between 10 and 130 K, and diminishes for temperatures higher than 130 K (Figure 5a). Also interesting is the dramatic increase of the D(3)...O(2) hydrogen bond responsible for connecting the molecules into columns (see Figure 5b). This last point is in complete accordance with the fact that torsion of NH_3 group presents important anharmonicity, as depicted during the discussion of Figure 1. So, one can understand the anharmonicity of $\tau(NH_3^+)$ as consequence of the modification of one specific hydrogen bond during the temperature variation [10]. Looking at the average C–D lengths one notes anomalies at low temperatures as presented in Figure 5c. From the Figure 5d one also notes an anomaly in the C–C–C bond angle that extends from about 160 K up to 225 K. In this point is important to emphasize that Raman spectroscopy studies showed splitting of bands associated with lattice modes at T ~ 170 K. This means evidence of a phase transition. Additionally, it was observed anomalies in the Debye-Waller factor, confirming the phase transition at about 170 K in the fully deuterated L-alanine [10].

L-valine was the second aliphatic amino acid crystal studied through neutron techniques. Investigations so performed revealed aspects related to hydrogen bonds, ultimately, respon-sible for the structural stability of the material. L-valine crystallizes in a monoclinic structure with $P2_1$ space group and four molecules per unit cell. From these molecules, two assumes *gauche I* conformation and two others *trans* conformation. Previous work using Raman spectroscopy suggested L-valine should undergo a solid-solid phase transition because impressive modifications of the bands associated with lattice modes were observed at low temperatures [28].

Figure 6 presents the dynamical susceptibility ($\chi''(E)$) of both L-valine hydrogenated [$(CH_3)_2CHCH(NH_2)CO_2H$] and deuterated [$(CD_3)_2CDCD(NH_2)CO_2H$] (synthesized by Dr. Ehrenstorfer GmbH from Augsburg, Germany). The comparison of the INS spectra of L-valine and deuterated L-valine (L-valine-d_8) shows differences that can be understood as follows. At first, an intense band at 480 cm^{-1} in the spectrum of L-valine-d_8 points to the accuracy of the assignment of the vibrations involving the N–H...O hydrogen bonds. Also, a decrease of the signal for energy lower than 450 cm^{-1} indicates they are associated with the CH_3 and CO_2 groups and the N–C–C units [9]. It is impressive in the room temperature INS spectrum of L-valine the presence of a mode at ~ 120 cm^{-1}. It is remembered that such a band not visible at T= 300 K appeared in the Raman spectra of L-valine for temperatures lower than 120 K. In other words, this band could be associated with a mode not active in the Raman spectrum of the monoclinic room temperature structure, being active only in the infrared. During the phase transition the mode should become Raman active and the phase transition should be realized as consequence
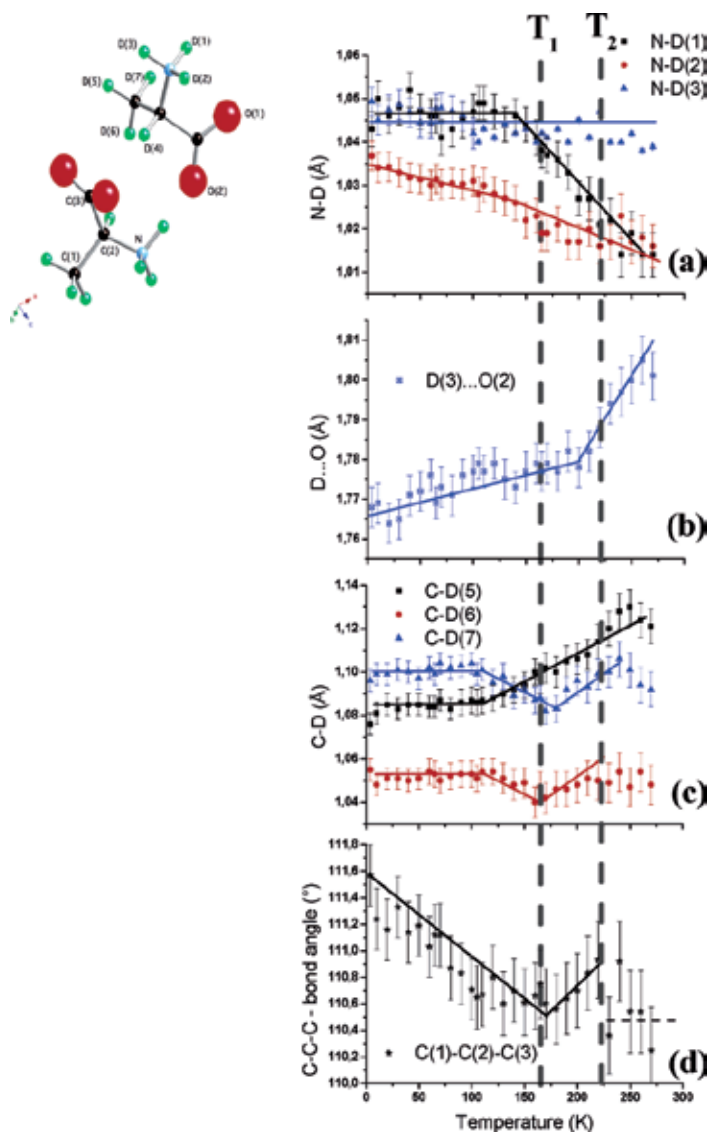
Figure 5. Temperature dependence of (a) N–D, (b) D...O, (c) average C–D length, (d) avergage C–C–C bond angles for fully deuterated L-alanine. The molecule is represented in the top left side of the figure an dashed lines are guides to the eyes [10].

of the activation of an infrared mode. An additional aspect of the study is to show (Figure 6b) the splitting of the band at ~ 15 meV at low temperature when compared with the spectrum recorded at 300 K, reinforcing the idea of a phase transition, as supported by the Raman spectroscopic study [28].

Up to now the present authors have seen several aspects of the bonds on L-alanine and an explanation for the phase transition undergone by L-valine using neutrons. It can be noted
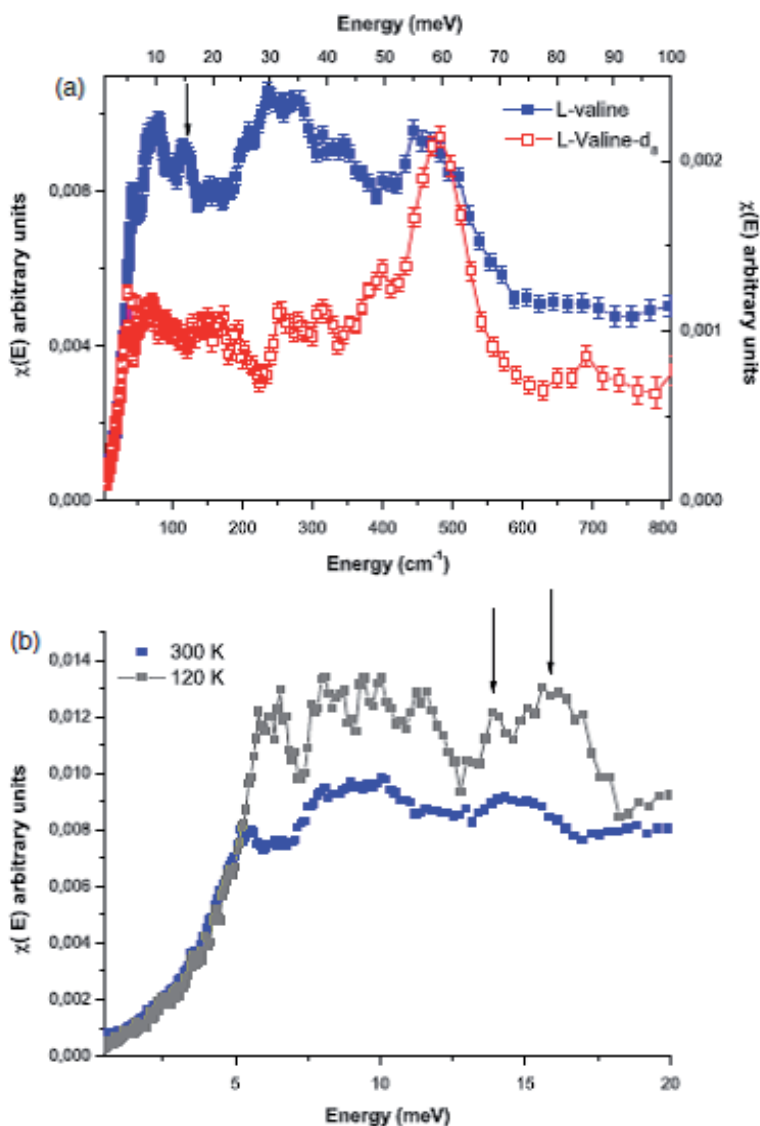
Figure 6. (a) Dynamical susceptibility [χ′′(E)] for both L-valine (full squares) and L-valine-d$_8$ (open squares) using a 5.1 Å incident wavelength at the NEAT spectrometer. (b) χ′′(E) of L-valine for two temperatures, 300 K and 120 K. The arrow in part (a) corresponds to the mode at 120 cm^{-1}, observed in the low temperature range by Raman spectroscopy [12].

that subtle conformational change can lead to impressive modifications in the structural and vibrational properties of these two members of the amino acid family. Now, the discussion deals about another aliphatic amino acid. L-leucine, NH_3-CH-CO_2-CH_2-CH-$(CH_3)_2$, crystallizes in a monoclinic structure *P2$_1$* with four molecules per unit cell. The carboxyl and amino groups are hydrogen bonded in a double layer, forming the crystal structure. The van der Waals interaction plays its role by connecting neighboring layers [1]. Due the existence of an addi-

tional CH_2 group in its chain, L-leucine is slightly more hydrophobic than L-valine. A previous research demonstrated the occurrence of a phase transition in L-leucine at ~ 353 K possibly maintaining the crystal with a monoclinic structure [22].

Figure 7 presents the dynamical susceptibility function χ'' obtained from calculations based on the inelastic data from NEAT. It is perceived that below 280 K the mode at 30 meV (approximately at 240 cm^{-1}) presents a red shift down to 190 K and below this, presents a blue shift; also, the intensity increases on cooling. Interesting enough is the occurrence of a redistribution of intensity of the bands between 300 and 375 K that can be correlated with the phase transition observed at 353 K. The phase transition can also be glimpsed by the intensities of most modes located below 30 meV, associated with lattice modes, that show pronounced changes in the interval 300 – 375 K.
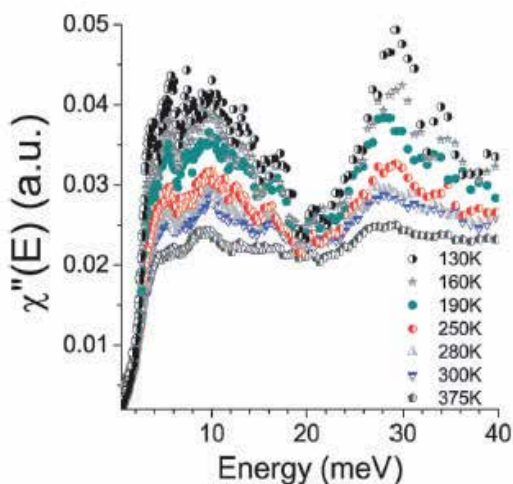
Figure 7. (a) Dynamical susceptibility [$\chi''(E)$] for L-leucine in the temperature range from 130 and 375 K measured in the energy interval from 1 to 30 meV. The mode at ~ 30 meV is associated with an out-of-plane vibration of CH_2 [29].

Supposing $S(Q,\omega)$ the scattering function, with Q being the magnitude of the scattering wave vector and ω being the energy transfer, it is possible to decompose it in three different components: $S_E(Q, \omega = 0)$, the elastic; $S_E(Q, \omega \sim 0)$, quasi-elastic; $S_E(Q, \omega > 0)$, inelastic. The study of the elastic scattering decay can furnish information about transitions because it appears as changes in the temperature dependence of the elastic intensity. Figure 8a shows the elastically scattered intensity as a function of temperature for L-leucine. The main contribution to S_E comes from the hydrogen atoms. Within the time scale of ~ 10 ps originated from the resolution of the equipment one can argue that the transition at ~ 150 K is a consequence of CH_3 groups. Such an anomaly confirms differential scanning calorimetry (DSC), as well as X-ray diffraction measurements [29].

In addition, one notes the broadening of the quasi-elastic response apparently disappears in the temperature range 220 – 250 K and the peak height decreases. It was possible to derive a
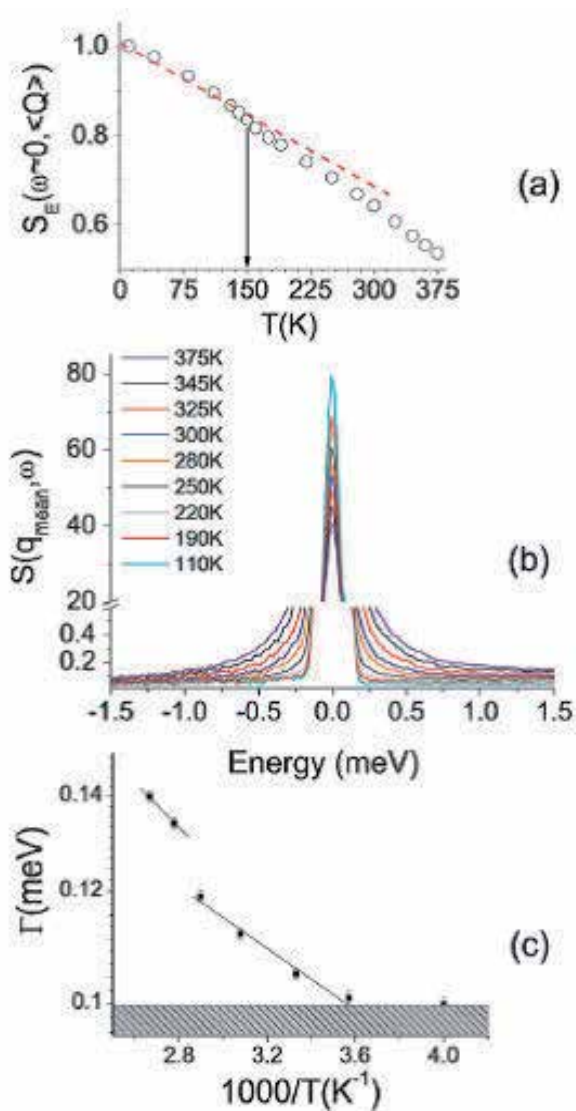
Figure 8. (a) Elastically scattered intensity as a function of temperature for L-leucine. An anomaly in the temperature evolution is marked by an arrow. (b) Dynamic structure factors obtained for AE = 98 μeV for several temperatures averaged over the whole range of Q. (c) Lorentzian half width at half maximum (HWHM), G, obtained using an Arrenhius-like relation [29].

qualitative description by fitting the quasi-elastic S_{QE}, using a Dirac function and a Lorentzian linewidth, which could describe, respectively, the elastic and quasi-elastic signals. In this approach it is possible to correlate the quasi-elastic broadening (Γ) with the activation energy, E_{act}, by the relation $\Gamma = \Gamma_0 . \exp[-E_{act}/kT]$. The most important point derived from this relation is presented in Figure 8c, where a discontinuity, associated with the high temperature phase transition is observed between 345 and 360 K.

6. Conclusions

Neutron diffraction and inelastic neutron scattering are powerful techniques to investigate several materials, among them, amino acid crystals, as it was shown in this chapter. From these studies it was presented the possibilty to correlate small variations of the network of hydrogen bonds to conformation changes in the amino acid molecules.

L-leucine, that presents only one polymorph at room temperature, was shown to undergo phase transitions at low and high temperatures. The new phases were analyzed and insights about the conformation of the molecules were attained.

In the case of L-valine it was possible through comparison between Raman spectroscopy and inelastic neutron scattering to identify infrared active modes responsible for the phase transition undergone by the crystal at approximately 120 K.

Finally, a series of information was obtained for the simplest proteic amino acid crystal, L-alanine. In the case of the fully deuterated sample, L-alanine-d_7, our results showed a clear evidence of a structural phase transition at ~ 170 K. Such fact can be related to the Ubbelohde effect, or in other words different dimensions of the hydrogen bonds stabilize differently the deuterated and the non-deuterated crystals. Consequently, although the deuterated sister presents a phase transition, the non-deuterated structure, even if a series of structural and vibrational anomalies are observed, is stable at low temperatures. Our investigations point to the fact that the Ubbelohde effect can be significant, even if only small changes of hydrogen bond dimensions occur.

Acknowledgements

Author details

Paulo T.C. Freire[1], José E.M. Pereira[2] and Heloisa N. Bordallo[2]

*Address all correspondence to: tarso@fisica.ufc.br

1 Departamento de Física – Universidade Federal do Ceará, Fortaleza, Brazil

2 Niels Bohr Institute – University of Copenhagen, Copenhagen, Denmark

References

[1] Fleck M, Petrosyan AM, Salts of amino acids: Crystallization, structure and properties. Heidelberg: Springer; 2011. 574 p. DOI: 10.1007/978-3-319-06299-0_1.

[2] Görbitz CH. Crystal structures of amino acids: from bond lengths in glycine to metal complexes and high-pressure polymorphs. Crystallography Reviews. 2015; 21: 160–212, DOI: 10.1080/0889311X.2014.964229.

[3] Boldyreva E, Cristalline Amino Acids: A Link between Chemistry, Materials Science and Biology, In: Boyens JCA, Ogilvie JF, editors. Models, Mysteries, and Magic of Molecules. Netherlands: Springer; 2007. p. 167-192. DOI: 10.1007/978-1-4020-5941-4.

[4] Freire PTC, JA Lima Jr, BTO Abagaro, GS Pinheiro, JAF Silva, JM. Filho, FEA Melo. High Pressure Raman spectra of amino acid crystals. In: Dominique de Caro, editor. Vibrational Spectroscopy. Rijeka: InTech; 2012. p. 37 – 58. DOI: 10.5772/1345. ch2

[5] Bordallo HN, Kolesov BA, Boldyreva EV, Juranyi F. Different Dynamics of Chiral and Racemic (L- and DL-) Serine Crystals: Evidenced by Incoherent Inelastic Neutron and Raman Scattering, Journal of the American Chemistry Society. 2007; 129: 10984–10985. DOI: 10.1021/ja073351n.

[6] Freire PTC, Pressure-Induced Phase Transitions in Crystalline Amino Acids, In: Boldyreva E, Dera P, editors, High Pressure Crystallography – From Fundamental Phenomena to Technological Applications. New York: Springer; 2010. p. 559-572. DOI: 10.1007/978-90-481-9258-8.

[7] Moggach SA, Allan DR, Clark SJ, Gutmann MJ, Parsons S, Pulham CR, Sawyer L. High-pressure polymorphism in L-cysteine: the crystal structure of L-cysteine-III and L-cysteine-IV. Acta Crystallographica B. 2006; 62: 296 – 309. DOI: 10.1107/S0108768105038802.

[8] Kistenmacher TJ, Rand GA, Marsh RE. Refinements of the crystal structures of DL-serine and anhydrous L-serine, Acta Crysttalographica B. 1974; 30: 2573 – 2578. DOI: 10.1107/S0567740874007618.

[9] Pawlukojc A, Borrowicz L, Natkaniec I, Leciejewicz J. The IINS spectroscopy of amino acids: L- and DL-valine. Spectrochimica Acta A. 1995. 51: 303-308. DOI: 10.1016/0584-8539(94)00812-P.

[10] Souza JM, Freire PTC, Bordallo HN, Argyriou DN. Structural isotopic effects in the smallest chiral amino acid: observation of a structural phase transition in fully deuterated alanine. Journal of Physical Chemistry B. 2007; 111: 5034 – 5039. DOI: 10.1021/jp070366z.

[11] Souza JM, Freire PTC, Argyriou DN, Stride JA, Barthès M, Kalceff W, Bordallo HN. Raman and neutron scattering study of partially deuterated L-alanine: evidence of a

solid-solid phase transition. ChemPhysChem. 2009; 10 3337- 3343. DOI: 10.1002/cphc.200900482.

[12] Silva JH, Lima Jr, JA, Freire PTC, Lemos V, Mendes Filho J, Melo FEA, Pizani PS, Fischer J, Klemke B, Kemner E, Bordallo HN. Raman spectroscopy and inelastic neutron scattering study of crystalline L-valine., Journal of Physics: Condensed Matter. 2009; 21: 415404. DOI: 10.1088/0953-8984/21/41/415404.

[13] Barthes M, Bordallo HN, Dénoyer F, Lorenzo J-E, Zaccaro J, Robert A, Zontone F. Micro-transitions or breathers in L-alanine? The European Physical Journal B. 2004; 37: 375-382. DOI: 10.1140/epjb/e2004-00069-1.

[14] Destro R, Marsh RE, Bianchi R. A low-temperature (23K) study of L-alanine. The Journal of Physical Chemistry. 1988; 92: 966-973 DOI: 10.1021/j100315a022.

[15] Migliori A, Maxton PM, Clogston AM, Zirngiebl E, Lowe M. Anomalous temperature dependence in the Raman spectra of l-alanine: Evidence for dynamic localization. Physical Review B. 1988; 38: 13464-13467. DOI: 10.1103/PhysRevB.38.13464.

[16] Kolesov BA, Boldyreva EV. Micro-conformational transition in L-alanine single crystals revisited by low wavenumber Raman spectroscopy. Journal of Raman Spectroscopy. 2010; 42: 696-705. DOI: 10.1002/JRS.2768.

[17] Teixeira AMR, Freire PTC, Moreno AJD, Sasaki JM, Ayala AP, Mendes Filho J, Melo FEA. High-pressure Raman study of l-alanine crystal. Solid State Communications. 2000; 116: 405-409. DOI: 10.1016/S0038-1098(00)00342-2.

[18] Olsen JS, Gerward L, Freire PTC, Mendes Filho J, Melo FEA, Souza Filho AG. Pressure-induced phase transitions in L-alanine crystals. Journal of Physics and Chemistry of Solids. 2008; 69: 1641-1645. DOI: 10.1016/j.jpcs.2007.12.005.

[19] Funnel NP, Dawson A, Francis D, Lennie DR, Marshall WG, Moggach SA, Warren JE, Parsons S. The effect of pressure on the crystal structure of l-alanine. CrystEngComm. 2010; 12: 2573-2583. DOI: 10.1039/C001296C.

[20] Tumanov NA, Boldyreva EV, Kolesov BA, Kurnosov AV, Quesada Cabrera R. Pressure-induced phase transitions in L-alanine, revisited. Acta Crystallographica Section B. 2010; 66: 358-371. DOI: 10.1107/s010876811001983X.

[21] Lima Jr. JÁ, Melo FEA, Mendes Filho J, De Sousa G.P, Lima RJC, Façanha Filho PF, Bordallo HN. Low-temperature Raman spectra of racemate DL-Alanine crystals. Journal of Raman Spectroscopy. 2010; 41: 808-813. DOI: 10.1002/jrs.2507.

[22] Façanha Filho PF, Freire PTC, Lima KCV, Mendes Filho J, Melo FEA, Pizani PS. High temperature Raman spectra of L-leucine crystals. Brazilian Journal of Physics. 2008; 38: 131-137. DOI: 10.1590/S0103-97332008000100024.

[23] Remédios CMR, Paraguassu W, Lima Jr. JÁ, Freire PTC, Mendes Filho J, Melo FEA, Menezes AS, dos Santos AO, Cardoso LP, Miranda MAR. Effect of Ni(II) doping on

the structure of L-histidine hydrochloride monohydrate, crystals, Journal of Physics: Condensed Matter. 2008; 20: 275209. DOI: 10.1088/0953-8984/20/27/275209.

[24] Lovesey SW. Neutron Scattering Theory. Oxford: Oxford Science Publications; 1986. 317 p. DOI: 10.1088/0953-8984/5/34/016.

[25] Squires GL. Introduction to the Theory of Thermal Neutron Scattering. New York: Cambridge University Press; 1978. DOI: 10.1080/00107514.2012.745613.

[26] Dianoux AJ, Lander G, editors (2003). Neutron data booklet. 2nd. Edition, ISBN: 0-9704143-7-4.

[27] Lehnman MS, Koetzle TF, Hamilton WC. Precision neutron diffraction structure determination of protein and nucleic acid components. I. Crystal and molecular structure of the amino acid L-alanine. Journal of the American Chemistry Society. 1972; 94: 2657 – 2660. DOI: 10.1021/ja00763a700.

[28] Lima Jr. JA, Freire PTC, Lima RJC, Moreno AJD, Mendes Filho J, Melo FEA. Raman scattering of L-valine crystals. Journal of Raman Spectroscopy. 2005; 36: 1076-1081. DOI: 10.1002/jrs.1410.

[29] Façanha Filho PF, Jiao X, Freire PTC, Lima Jr. JA, Dos Santos AO, Henry PF, Yokai-chiya F, Kremner E, Bordallo HN. Structure-property relations in crystalline L-leucine obtained from calorimetry, X-rays, neutron and Raman scattering. Physical Chemistry Chemical Physics. 2011; 13: 6576-6583. DOI: 10.1039/C0CP02278K.

Neutron Reflectometry for Studying Proteins/Peptides in Biomimetic Membranes

Joyee Chun In Yeung, Tsung-Wu Lin and Hsin-Hui Shen

Additional information is available at the end of the chapter

Abstract

The development of biomimetic surfaces for protein and peptide adsorptions is continuously expanding. Their biological functions can be influenced by the properties of the underlying artificial environment but the detailed mechanism is still not clear. In the past 30 years, neutron reflectometry has been widely applied to characterise the molecular structure of proteins or multi-protein complexes and their interactions with fluid artificial membrane that mimics the cellular environment. The specific interactions, bindings or structural changes between proteins and membranes play a crucial role in cellular responses and have promising potential in diagnostics and other biosensor applications. This chapter presents the progression of surface design for protein adsorption/interactions on membranes in detail, ranging from a simple phospholipid monolayer setup to more complicated artificial lipid bilayer systems. Furthermore, a new development of designed surfaces for studying the integral membrane protein system is also discussed in this chapter. A brief overview of various membrane mimetic surfaces is first outlined, followed by presenting specific examples of protein-membrane interactions studied by neutron reflectometry. The author demonstrates how to use neutron reflectometry as an advanced technique to provide step-by-step structural details for biomolecular applications in a well-controlled manner.

Keywords: Neutron reflectometry, biomimetic surfaces, artificial membrane, proteins, peptides

1. Introduction

Proteins are vital molecules that are responsible for many critical biological processes such as photosynthesis, respiration, cellular signal transduction, molecular transportation and enzymatic catalysis [1]. Most of these biochemical processes involve the interactions with proteins that are embedded in or associated with lipid molecules [2]. The protein-membrane

interactions are dynamic, complicated and mainly driven by hydrophobic and electrostatic interactions, but the detailed mechanism is still not clear [3]. Understanding and further modulating the interactions between proteins and membranes are essential for many biological and biotechnological applications. Many *in vitro* studies have been conducted to reveal and monitor the molecular interactions between proteins and lipids [3, 4]. The proteins are adsorbed or immobilised on a biomimetic surface that reconstitutes the physiological environment, i.e., the use of artificial membrane models to mimic the biological membrane [5]. Neutron reflectometry is a powerful and non-destructive technique that has been widely employed for studying biomolecular interactions. It has unique properties to provide quantitative structural and compositional details of the model interfaces without physical damage to the sample, which is impossible to achieve using other techniques [6, 7].

Neutron reflectometry is a powerful tool to probe the interfacial chemical structures at the microscopic level. The setup for neutron reflectometry measurements requires a parallel neutron beam that is incident onto the sample deposited onto an optically flat surface, where the neutron beams reflect and exit from the opposite end [6]. The neutron reflectivity, R, refers to the ratio of the incoming and exiting neutron beams and it is measured as a function of momentum transfer Q, which is defined as $Q = 4\pi \, sin\theta / \lambda$, where θ is the angle of incident and λ is the neutron wavelength [6, 8, 9]. $R(Q)$ is approximately given by $R(Q) = \frac{16\pi^2}{Q^2} | \rho(Q) |^2$, where $R(Q)$ is the one-dimensional Fourier transform of $\rho(z)$, the scattering length density (SLD) distribution normal to the surface. SLD is the sum of the coherent neutron scattering lengths of all atoms in the sample layer divided by the volume of the layer. Therefore, the intensity of the reflected beams is highly dependent on the thickness, densities and interface roughness of the samples [4, 6]. If there are mixed layers containing two components, A and B and water (w), the scattering length density will be $\rho = \phi_A \rho_A + \phi_B \rho_B + \phi_w \rho_w$, where ϕ is the volume fraction of each layer and ρ can be different contrasts from the same layer/substance, called contrast variations. The use of contrast variations in neutron reflectometry experiments allows resolving molecular species in response to stimuli; hence, it is possible to obtain detailed structure information with very high resolution [9]. There are two different approaches for contrast variations: magnetic contrast and isotopic contrast. Polarised neutron can generate a magnetic contrast that is able to produce simultaneously two datasets from exactly the same layer without changing the chemical environment [10, 11]. On the other hand, the isotopic approach is often used in the characterisation of multilayer, biological films [7]. By changing different buffer compositions (D_2O, H_2O and D_2O/H_2O mixtures) or using selective deuteration to replace hydrogen in desire locations, the contrast of scattering density between the hydrogen and deuterium reveals the relative locations in multi-component systems [12, 13]. By monitoring the isotopic labels, the distributions of different components in an *in-situ* environment can be identified; hence the accurate compositional depth profiles and thickness of the biological film can be determined [4, 14]. Typically, this method is applied to investigate the structural orientation and conformation changes of proteins adsorbed on membranes in a non-crystalline aqueous environment [12, 13]. The structural information of proteins/or peptides and membranes can be determined at Angstrom nanometre scale.

Researchers have developed different artificial membrane models to reconstitute the essential features of the biological membranes, providing an appropriate system to investigate the

structure-function relationships of proteins in membrane-mediated processes such as protein- or peptide-membrane interactions [15, 16]. This review discusses and examines several protein adsorption studies on different biomimetic membrane models used in neutron reflectometry. The biomimetic membrane models used are phospholipid monolayer at air/water interface (Section 2), phospholipid monolayer on solid supports (Section 3) and fluid lipid bilayers on a solid support (Section 4). The preparation of each membrane model is briefly described and characterised by neutron reflectometry, with particular attention on their biological applications in protein/or peptide adsorption. Furthermore, there are reviews that describe a direct immobilisation of membrane proteins on gold-modified surface (Section 5), as an alternative method for protein adsorption studies. This method is suitable for the use of various immobilising surfaces and addresses the problem of maintaining the proper orientation of the immobilised proteins, hence should have a wide range of *in vitro* applications. The summary of the key and significant findings is stated.

2. Biomolecules interact with phospholipid monolayer at air/water interface

Phospholipid monolayer at the air/water interface has been used as the simplest biomimetic membrane model [17]. A lipid monolayer can be formed by depositing the lipid solution on the surface of water within a Langmuir-Blodgett trough. The amphiphilic properties of the lipid molecules allow the hydrophilic headgroups to interact with the water and leaving the hydrophobic alkyl chains exposed to the air, forming a planar, two-dimensional lipid phase. The resulting homogeneous lipid monolayer is called a Langmuir monolayer with high reproducibility [17, 18] (Figure 1). The lipid packing density of the phospholipid monolayer formed using the Langmuir trough can be precisely monitored by controlling the applied surface pressure (π) as a function of the molecular area (A) at a constant temperature. At a low surface pressure, the disordered phospholipid molecules exist in the gas phase. When a lateral surface force is applied, the phospholipid molecules are compressed into the liquid-expanded phase, followed by the coexistence of the liquid-expanded and the liquid-condensed phases. Further increase in the surface pressure allows the phospholipid molecules to orient in an orderly manner and presents as the solid state. Once the applied pressure reaches a certain limit, the phospholipid monolayer collapses [17, 19]. The organisation and dynamics of the phospholipid monolayer at the air/water interface have received immense interests in their biological applications. This model setup allows us to tailor the lipid packing density, which has a direct influence on the protein or peptide interactions with membranes [18]. The ability to monitor the lipid packing density throughout the experiment is beneficial and unique about this biomimetic membrane, which is not easy to control in many artificial membrane models [18].

The physical properties of phospholipid monolayer at the air/water interface influenced protein adsorption, as demonstrated in Maierhofer and co-workers' neutron reflectometry study [20]. The zwitterionic phospholipid monolayer used in the study consisted of 1,2-dipalmitoyl-*sn*-glycero-3-phosphocholine (DPPC) mixed with various molar ratios of 1,2-dimyristoyl-*sn*-glycero-3-phospho-(1'-rac-glycerol) (DMPG), to evaluate the surface charges
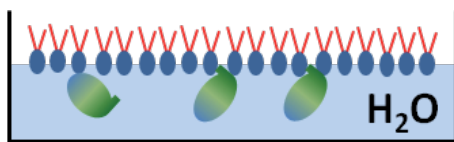
Figure 1. Diagram of phospholipid monolayer deposited on air/water interface prepared in a Langmuir trough. The phospholipid hydrophilic head group interacts with the aqueous solution, leaving the phospholipid hydrophobic tails exposed to the air. Protein adsorption occurs from the aqueous phase to the phospholipid monolayer.

of phospholipid monolayer in affecting cytochrome c adsorption. Higher protein adsorption was observed on the DPPC monolayer mixed with a 30 molar percent of DMPG, for which the DPPC/DMPG monolayer, existed in liquid-condensed phase. However, similar amount of cytochrome c was adsorbed on the equal molar mixture of DPPC and DMPG monolayer, known as an ideal lipid mixing [20]. The result strongly suggested that the electrostatic interactions between cytochrome c and the DPPC/DMPG monolayers were driven by the domain formation during phase transition of the non-ideal lipid mixing of the phospholipid monolayer that is predominantly at the liquid-condensed phase rather than the liquid-expanded phase [20].

Miano et al. [21] observed a constant thickness of 16 Å when DPPC monolayer was deposited on the air/water interface by applying various surface pressure using Langmuir-Blodgett trough. The molecular density (area per molecule) varied from 40 to 70 Å^2 accompanying in the change of surface pressure [21]. The neutron reflectometry study from Miano et al. also showed that the amount of protein associated with membranes decreased when the lipid monolayer surface pressure increased. Another study investigated the interactions of lacto-ferrin, a typical tear protein, on the DPPC monolayer deposited at the air/water interface, as a model of preocular tear film outer interface. The amount of lactoferrin coadsorbed onto the DPPC monolayer decreased as the surface pressure on the DPPC monolayer increased [21]. The coadsorbed lactoferrin penetrated into the phospholipid monolayer and characterised into two layers: 20% of the protein phase was located at a top dense sublayer (15 Å) and 10% of the protein phase was adsorbed to the bottom sublayer (60 Å) [21]. The structural distribution of the coadsorbed lactoferrin layers provided a mechanistic detail of how the tear proteins interact with the lipid film, as an *in vitro* preocular model for evaporative tear loss [21].

Recently, the use of Langmuir trough in combination with neutron reflectometry also illustrated how packing density could be altered and resulted in different conformations of the proteins [18, 22]. Pirrone et al. [18] monitored the membrane association process of human immunodeficiency virus-1 Negative Regulatory Factor (HIV-1 Nef) protein on a phospholipid monolayer formed on air/water interface [18]. The conformation of HIV-1 Nef proteins was found to be sensitive and dependent on lipid packing density. At a high lipid packing density (35 mN/m), the HIV-1 Nef protein maintained in a compact conformation and did not insert into the phospholipid monolayer. In a low lipid packing density (20 mM/m), both n-terminal region and c-terminal unstructured loop of the HIV-1 Nef proteins underwent conformation changes [18, 22]. The repositioning of HIV-1 Nef proteins caused the hydrophobic residues on

the N-terminal inserted into the membrane and the proteins were oriented away from the phospholipid monolayer to a position 70 Å away [18, 22].

3. Biomolecules interact with phospholipid monolayer on solid supports

The amphiphilic nature of lipid molecules allows a spontaneous formation of Langmuir-Blodgett lipid film on a solid support, including glass, silica, micas and metal substrates [17]. However, the hydrophobic tail of lipid molecules does not encourage the formation of lipid monolayer on hydrophilic substrates [23, 24]. The technical challenge is overcome by chemically grafting the solid support with a polymer or surfactant, for example, octadecyltrichlorosilane. The surface hydroxyl groups of octadecyltrichlorosilane form covalent siloxy bonds with the substrate, resulting in a self-assembled layer and leaving the hydrophobic layer for subsequent phospholipid adsorption. The strong hydrophobic interactions between the lipid molecules and the robust hydrophobic part of surfactant allow for the phospholipids to be deposited using a Langmuir-Blodgett technique and hence promotes the formation of homogeneous monolayer (Figure 2) [23, 24].
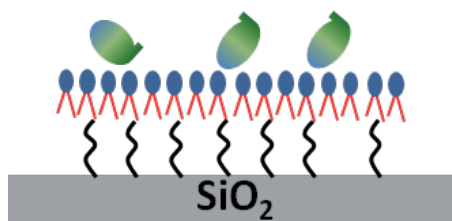
Figure 2. Phospholipid monolayer deposited on chemically grafted solid support, the hydrophobic interactions forms the phospholipid monolayer onto the self-assembled hydrophobic octadecyltrichlorosilane-modified surface.

The surface coverage of octadecyltrichlorosilane formed on the solid support was found to be 68%, with the thickness of 24.0 Å to 33.5 Å [24, 25]. Subsequently, phospholipid monolayers were deposited on the octadecyltrichlorosilane-modified solid support and their structural information was extracted from neutron reflectometry (Figure 2). Kuhl et al. [23] claimed that the structure of phospholipid monolayers was not affected by the quality of octadecyltrichlorosilane deposited underneath. The octadecyltrichlorosilane-lipid layer was further studied in detail by Hollinshead et al. [24]. They observed that the phospholipid molecules penetrated into the octadecyltrichlorosilane layer and reported as a four-layer model. The first layer was the solid support (22.6 Å); the second layer (17.9 Å) and the third layer (12.6 Å) consisted of a combination of octadecyltrichlorosilane and phospholipid hydrocarbon chains and the top layer (9.4 Å) contained the phospholipid headgroup molecules only [24]. On the other hand, Kuhl et al. also demonstrated that the phospholipid monolayer, 1,2-distearoyl-sn-glycero-3-phosphoethanolamine (DSPE), could be functionalised with polymer such as polyethylene glycol (PEG). The DSPE-PEG monolayer gave the thickness of 52 Å on quartz surface and 48

Å on silicon surface. Thickness fluctuations of the PEG layer were adjusted by varying the concentration of polyethylene glycol in the phospholipid monolayer [23].

Lu et al. [26] reported the formation of phospholipid monolayer, phosphorylcholine (PC), on octadecyltrichlorosilane had a thickness of 18 Å [26]. The use of phospholipid monolayer mimics one leaflet of a biological membrane, and therefore it is ideal to investigate the interactions of peripheral membrane proteins [18]. The membrane interactions between lysozyme and albumin have been extensively studied and well-characterised [26, 27]. These proteins were selected as the model proteins for undertaking the neutron reflectometry experiments to reveal their interfacial structural conformations when adsorbed onto the phospholipid monolayer. The adsorption of lysozyme and albumins on the phosphorylcholine monolayer formed a thick and diffuse layer with the thickness of 60 Å and 80 Å, suggesting a loose protein layer deposited on phosphorylcholine monolayer [26, 27].

The other application of phospholipid monolayer on a solid support is to investigate the sensitivity of biodiagnostic assays [26] showing non-specific interaction of protein molecules. To retain the protein bioactivity, the phospholipid monolayer can be functionalised with a ligand such as biotin that is widely used to control protein orientation during adsorption [28]. Biotin bound to the headgroup of the phospholipid molecules and formed a biotin-lipid layer, followed by the binding of tetrameric protein, streptavidin, on the biotin-lipid layer. Neutron reflectometry results from Schmidt et al. [28] showed that only 5% of the DPPC molecules were carrying a biotin moiety. The layer thickness of DPPC monolayer, biotin moiety and the streptavidin proteins were 24 Å, 10 Å and 41 Å, respectively [28], that can be well defined by neutron reflectometry.

4. Biomolecules associated with fluid lipid bilayers on a solid support

The use of fluid lipid bilayer membrane as a model platform to study the influence of the bilayer microenvironment in protein-membrane interactions has been rapidly developed [15, 16]. Various lipid bilayer models exist, including (a) single supported lipid bilayers, (b) tethered lipid bilayer membranes, (c) polymer-cushioned bilayer membranes and (d) floating supported bilayers as described in Figure 3 [29].
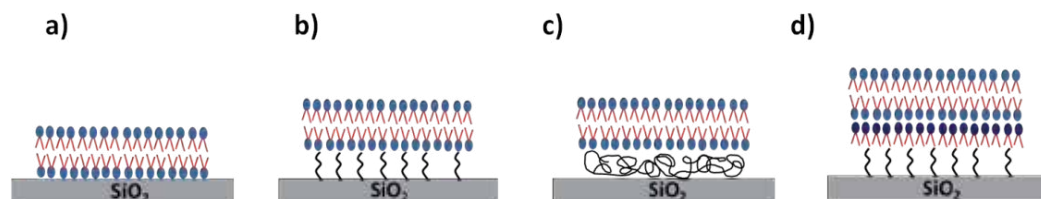
Figure 3. Different types of supported lipid bilayers on a solid support: (a) single supported lipid bilayers, (b) tethered lipid bilayer membranes, (c) polymer-cushioned bilayer membranes and (d) floating supported bilayers.

4.1. Single supported lipid bilayers

Single supported lipid bilayers (SLBs) are commonly employed as the simplest lipid bilayer model in which the lipid bilayers are directly deposited on a hydrophilic surface (Figure 3a) [29]. SLBs are the most popular artificial membrane model because of their long-term stability, ease of formation and manipulation and wide applicability in studying membrane-related features and applications [29]. The following three methods are often used individually or in combination to the formation of SLBs: lipid vesicle fusion, lipid-detergent method and Langmuir-Blodgett and Langmuir-Schaefer deposition [29].

4.1.1. Lipid vesicle fusion

Lipid vesicle fusion is a spontaneous reaction, where the lipid vesicles adsorb, rupture and form a lipid bilayer which covers greater than 80% of a solid hydrophilic support [30]. This process is dependent on the surface properties (charge, structure and roughness), lipid nature (composition, charge, size and physical state) as well as the nature of the solvent (pH and ionic strength) [29, 31, 32]. The lipid vesicle fusion technique was used for studying the formation of SLBs made of different types of unsaturated phospholipids, including 1-palmitoyl-2-oleoyl-sn-glycero-3-phosphocholine (POPC), 1-palmitoyl-2-oleoyl-sn-glycero-3-[phospho-rac-(1-glycerol)] (POPG), 1-palmitoyl-2-oleoyl-sn-glycero-3-[phospho-l-serine] (POPS), 1,2-dioleoyl-*sn*-glycero-3-phosphocholine (DOPC) and 1,2-dioleoyl-*sn*-glycero-3-phospho-l-serine (DOPS) [33–35]. The experiments were set above the phospholipid phase transition temperature, thus the lipid bilayers existed in the fluid phase. The formation of SLBs is symmetric between the two lipid layers, and the membrane structure can be modelled from the neutron reflectometry data [33–35]. The thickness of each layer varied depending on the types of phospholipids used to form SLBs. The lipid bilayer had an overall thickness ranging between $38 \pm 3\text{Å}$ and $56 \pm 3\text{Å}$, which were separated into three discrete layers: head group one (in contact with bulk solvent), acyl tails and head group two (in contact with the solid support). The modelling data also yielded information on other structural parameters including area per lipid molecule, volume fraction and surface excess of the three discrete layers (head-tail-head) [33–35].

The integrity of SLBs formed by lipid vesicle fusion technique has been fully characterised using neutron reflectometry, and it has been shown as a promising application to study membrane-mediated processes. Fernandez et al. [36] studied the interactions of antimicrobial peptide, maculatin 1.1, on both eukaryotic- and prokaryotic-mimic membranes using neutron reflectometry. The cationic maculatin 1.1 showed a minimal effect to the eukaryotic-mimic membrane; whereas, a profound effect was found when interacting with the anionic head group on the prokaryotic-mimic membrane. A decrease in anionic head group thickness was observed, but the thickness of acyl tails region remained the same, suggesting a reordering of bilayer occurred to associate with transmembrane pore formation [36]. Hellstrand et al. [34] also used neutron reflectometry to determine the position of α-synuclein, an amyloid protein associated with Parkinson's disease, within and outside of the membrane bilayer. The α-synuclein was found to embed in the bilayer outer head group via electrostatic interactions but did not penetrate into the hydrophobic acyl chain region. The study then compared the adsorption of α-synuclein on different biological relevant membranes which were composed

of pure POPC, the mixtures of POPC/POPS or cardiolipin. The effect of membrane fluidity (acyl chain saturation), head group separation and the electrostatic shielding of the phospholipids strongly influenced the association of α-synuclein onto the membranes [34]. An analogue study was carried out on prion protein, which is widely recognised as the causative agent for Parkinson's disease when the protein is misfolded [33]. The interactions of N-terminal cleavage fragments (N1 and N2) of prion protein on negatively charged POPG-contained SLBs were probed using neutron reflectometry. The results implied that both N1 and N2 were inserted into phospholipid head groups; however, the interactions were stronger for N1 fragment because of the additional metal ion binding site located at a polybasic region. The insertion of N1 fragment induced an increase in lipid order in the absence of phase transition, as evidenced by lengthening of lipid acyl tails and decreasing in lipid area. It is possible that prion protein N-terminal fragment plays a functional role on membrane interactions [33]. Recently, Lu et al. [35] employed neutron reflectometry to define the molecular determinants of cellular protein layers adsorbed on mimetic apoptotic membranes. The interactions between annexin V and membranes contained different amount of phosphatidylserine (PS) phospholipids were examined, which is a crucial process to detect early/mid-stage cell membrane apoptosis *in vivo* and *in vitro*. The membrane properties that were affected by PS contents strongly affected annexin V binding, showing an increase in annexin V binding with an increase in PS content in the membrane and that there was a maximum binding at 20% of PS in the membrane. A decrease in the thickness of the adsorbed annexin V layer was observed with a 33% of PS content in membrane, suggesting the annexin V might alter its conformational change at high PS content [35].

4.1.2. Lipid-detergent method

Lipid-detergent method is an alternative method for depositing SLBs on solid support. Tiberg et al. [37, 38] have successfully demonstrated the formation of SLB with the aid of detergent incorporated into the lipid forming micelles. The presence of detergents allows saturated fatty acids such as DPPC that has high hydrophobicity, to form stable micelles in aqueous solution [39]. In this method, the detergent is first incorporated into the lipid solution in excess amount, this helps to emulsify the lipid molecules and raise to the critical micelle concentration. Once lipid molecules concentration reached the critical micelle concentration, they aggregated into stable lipid micelles, which were introduced and adsorbed onto a hydrophilic silica surface [37–40]. The resulted SLB was identical to those formed using the vesicle fusion method once the detergent was completely removed [29, 38, 40, 41]. The cholesterol incorporated DPPC membranes were also used to study the effect of added components on the resulting SLBs. The neutron reflectometry results showed that the cholesterol was located below the lipid head group region and subsequently led to an increase in membrane thickness [38].

In addition to the membrane structural information, neutron reflectometry was also used to study protein interactions with membranes [29, 42]. Vacklin et al. [42] investigated the physical interactions between phospholipase A_2 (PLA$_2$) upon regulating its enzymatic hydrolysis on supported lipid bilayer. They were able to monitor the membrane bilayer changing its morphology when exposed to PLA$_2$ and the reaction was irreversible. By using phospholipids

with a different degree of saturation, the rate of PLA$_2$ hydrolysis decreased as lipid saturation increased. This gave the smallest penetration depth on the unsaturated phospholipid, 1,2-dioleoyl-sn-glycero-3-phosphocholine (DOPC); and the greatest penetration depth on the saturated phospholipid, DPPC [42]. Shen et al. [43] studied the interactions of lipopeptide surfactin on supported DPPC bilayers, observing that the membrane stability was highly dependent on the critical micelle concentration of surfactin. The membrane was stable at a low surfactin concentration (below the critical micelle concentration). Neutron reflectometry can further identify the accumulation of surfactin on membranes showing that the surfactin penetrated into the outer leaflet of the membrane bilayer with pore formations on the membrane. When the surfactin concentration reached or exceeded the critical micelle concentration, the DPPC SLB was solubilised and progressively removed from the surface [43].

4.1.3. Langmuir-Blodgett and Langmuir-Schaefer deposition techniques

Langmuir-Blodgett and *Langmuir-Schaefer* deposition techniques are the most versatile methods for the preparation of thin and highly organised molecular films [44]. The amphiphilic lipid molecules have the self-assembled properties, which allow the lipid molecules to arrange in a monolayer film at an air/liquid interface on a solid support. The vertical lipid deposition usually forms a homogeneous layer with a controllable thickness of the deposited film, also called Langmuir-Blodgett film [45]. The solid support is placed vertically into the lipid solution. The resulted monolayer (first layer) has the lipid head groups interacting with the solid support and the acyl tail regions pointing towards the gas phase on a hydrophilic solid support, whereas on a hydrophobic solid support, the acyl tail regions interact with the solid surface, leaving the lipid head groups point outwards. Another similar method, *Langmuir-Schaefer* deposition in which the solid support is oriented horizontally is commonly used for lipid deposition [45]. Combining both vertical and horizontal lipid deposition techniques, the formation of SLB can be easily achieved using the Langmuir-Blodgett method for depositing the first lipid layer, and the *Langmuir-Schaefer* method for the deposition of the second lipid layer [45].

Recently, Clifton et al. [46] demonstrated how the Langmuir-Blodgett and Langmuir-Schaefer methods can be used to create a asymmetric SLB as a mimic of the complex Gram-negative bacterial outer membrane. The inner membrane leaflet of the outer membrane is mainly composed of phosphatidylcholine, which was deposited on hydrophilic surface using the Langmuir-Blodgett method. The outer membrane leaflet of outer membrane was deposited via Langmuir-Schaefer method, which contained either Lipid A or *Escherichia coli* rough lipopolysaccharides [46]. In the combination of both Langmuir-Blodgett and Langmuir-Schaefer techniques, the asymmetric SLBs were detected with greater than 90% surface coverage on solid support. The asymmetric SLBs also maintained high stability over time; this enabled us to clearly resolve the structure of the asymmetrical bilayer leaflets [46]. The development of functionalised biomimetic membrane using Langmuir-Blodgett and Langmuir-Schaefer methods is of great interest in nanobiotechnology for years [45]. However, the applications of neutron reflectometry to study biological phenomenon on Langmuir-Blodgett and Langmuir-Schaefer method–formed SLBs are not available.

4.2. Tethered lipid bilayer membrane

Tethered lipid bilayer membrane (t-BLM) is the lipid bilayer deposited on molecular anchors that act as spacers between the membrane and the solid support [47]. The use of self-assembled molecules as a surface coating technique has been developed since the early 1990s [47]. Molecules or ligands that form spontaneously via chemisorption from a solution or gas onto a solid support can result in a self-assembled monolayer [47]. Short oligomers or alkanethiols are often used as the applications of self-assembled monolayer that forms covalent bonds to the solid support such as gold and mercury, and the terminal functional groups create new surface properties on the solid support [15, 47, 48]. The deposition of lipid vesicles onto self-assembled monolayer allows the formation of tethered lipid bilayer membrane in which the lower bilayer leaflet interacts with the terminal functional group on self-assembled monolayer and the upper leaflet of phospholipids forms a functional lipid layer (Figure 3b) [15]. Tailoring the surface properties of the solid support improves the long-term stability for t-BLM, and hence widening the potential applications.

A neutron reflectometry study from Junghans et al. [49] used the selection of spacer group in affecting the formation of tethered lipid bilayer membrane. The types and the length of the spacers influenced the molecular geometry of the lipid molecules and hence affecting the structural and electrical properties on the membranes [49]. The use of long alkyl chain spacers increased water incorporation within the spacer units, which gave rise to a less dense packing order, an increase in both bilayer defect rate and roughness of the bilayer interfaces [49]. Alternatively, shorter spacer units had the highest surface coverage and also little water incorporation, resulting in an increase in membrane resistances [49]. With the controlled length of spacer, an optimum membrane architecture can be created, which allows for creating the physiological environment in which the protein-membrane interactions can be studied and further leading to possible biological applications.

Recently, the applications of tethered lipid bilayer membrane and neutron reflectometry were employed to investigate the orientations and conformations of membrane-bound protein, glucocerebrosidase (GCase), in an aqueous environment [50]. GCase was partially inserted into the tethered lipid bilayer membranes with its active site exposed to the membrane-water interface [50]. The use of selective deuteration techniques and the reflection of neutrons simultaneously extended the applications for protein complex characterisation. The results obtained from neutron reflectometry showed a large conformational change in GCase when interacted with α-synuclein (α-syn) [50]. Previous research has suggested that the formation of α-syn/GCase complex inhibited the enzymatic reaction of GCase, which might lead to the development of Parkinson disease and related disorders [51].

4.3. Polymer cushioned membranes

Polymer cushioned membranes are lipid bilayers deposited on a soft polymeric layer that coated on a solid support (Figure 3c) [16]. The use of polymeric layer mimics the cytoskeleton or extracellular matrix in plasma membrane, which is important in reconstituting the morphology of membrane domains as well as maintaining the nature and mobility of the trans-membrane proteins [16, 29]. The polymeric layer must have the following properties: the

hydrophilic polymer is able to form a thin, uniform layer for the deposition of lipid bilayer. And secondly, the polymeric layer has a well-defined elastic modulus that is highly reproducible and chemically inert to the membranes or to the solid support [16]. The thickness, density and water content of the polymer cushioned layer as well as the membrane bilayer can be determined by neutron reflectometry. The deformability of polymer cushioned membranes provides a more natural cell-like environment for membrane-associated process [52]. The experimental setup of neutron reflectometry allows the lipid bilayer to maintain at a physiological condition where the membrane exists in the fluid state. This provides a great potential to study and the membrane-mediated interactions and monitor the experimental conditions *in situ* [53].

The use of beta-amyloid peptides as the model for Alzheimer's disease has been widely studied and recognised [54]. Dante et al. [53] used neutron reflectometry to study the role of beta-amyloid peptides on polymer cushioned membranes. The data from neutron reflectometry evidenced a change in the lateral diffusion of the lipid bilayer when exposed to beta-amyloid peptides. It, therefore, suggested that the beta-amyloid peptides penetrated into the lipid bilayer and softened the lipid membrane bilayers [53]. These results strongly indicated that the change in lipid membranes' structural and mechanical properties could influence and alter membrane-based signal transduction. Monitoring the interactions of beta-amyloid peptides on membrane with neutron reflectometry provided insights into the onset of Alzheimer's disease [53].

4.4. Floating supported bilayers

Floating supported bilayers were first described by Fragneto et al. [55] as a new artificial membrane system formed on a solid support. In this SLB model, the lipid bilayer was formed in two steps: a Langmuir-Blodgett technique and a Langmuir-Schaefer technique. Firstly, a Langmuir-Blodgett technique was used to deposit a monolayer of lipid onto the solid support that was placed vertically (lipid monolayer with dark blue headgroup on Figure 3d). A lipid bilayer (lipids with light blue headgroup) was then horizontally introduced onto the lipid monolayer using a Langmuir-Schaefer technique (i.e., horizontal deposition). Therefore, the second bilayer interacted with the lipid monolayer, hence named floating lipid bilayer (lipid bilayer with light blue headgroup on Figure 3d) [55].

Talbot and co-workers [41] used neutron reflectivity technique to compare the formation of SLBs using various methods as described previously, this was further extended to investigate the interactions between a cationic gene delivery vectors (lipoplexes) with different SLB model membranes such as direct membrane deposition and polymer cushioned membranes. The data showed that the cationic lipoplexes could easily destroy the floating supported bilayers on silicon dioxide surface as well as those SLB formed on polymer-cushioned silicon surface. The surface of the solid support might exert some influence to the destruction of floating supported bilayers. However, a chemically grafted membrane layer, octadecyltrichlorosilane (OTS)-hybrid floating supported bilayer, is a perfect model bilayer to investigate the interactions between lipoplex and membranes. This membrane model had proven high stability to the exposure of solvents and lipoplexes over a considerable duration of time, suggesting the OTS-

floating supported bilayers were not destroyed by the lipoplexes. Their work has established a new floating supported bilayers model that has minimum interference from the solid support, and hence it is suitable for studying the lipoplex-membrane interactions and correlates the transfection efficiency of this gene-delivery vector [41].

The usefulness of floating supported bilayers as a physiological mimic to the bacterial outer membrane helps to encounter technical challenge to recreate and study the interactions of antimicrobial proteins *in vitro*. Clifton et al. [56] described the formation of asymmetric floating supported bilayers fabricated by sequential Langmuir-Blodgett deposition of 1-oleoyl-2-(16-thiopalmitoyl)-sn-glycero-3-phosphocholine (thiolPC) and Langmuir-Schaefer deposition of floating supported bilayers consisted of lipopolysaccharides to mimic the bacterial outer membrane. The thiolPC layer and the floating supported bilayers are separated by a small water gap; hence the DPPC and lipopolysaccharides bilayers are floating on the solid support [56]. This floating-supported bilayer system has been fully studied and characterised using neutron reflectometry with high stability and reproducibility. The use of floating supported bilayers makes it possible to maintain the dynamicity, fluidity and translation freedom of the membranes; therefore, the membrane properties are not altered and behave similarly in their physiological environment [56–58]. Further studies show that lactoferrin, a cationic antimicrobial protein, directly interacts with lipopolysaccharides on the outer membrane via electronic interactions. The results from neutron reflectometry revealed a dramatic reduction in the floating supported bilayer coverage in the presence of lactoferrin, providing a structural picture of lactoferrin disrupting the outer membrane [56]. Another cationic enzyme, lysozyme was found to bind to the outer membrane electrostatically without changing the floating supported bilayer coverage, and a small increase in membrane bilayer roughness was also detected. These two studies both reported a change in floating supported bilayers properties upon interactions with the antimicrobial proteins; however, the neutron reflectometry data implied that the lysozyme disrupted the outer membrane in a different mechanism than lactoferrin [56].

5. Membrane proteins on gold-modified surface

Membrane proteins are well-known to be difficult to handle and study outside their natural lipid environment because they are flexible, unstable and relatively hydrophobic [1]. To overcome the problems, membrane proteins are extracted from membranes in the existence of detergents, which helps to stabilise membrane proteins during extraction, solubilisation, purification and crystallisation [1, 59]. To examine the structure-function relationships of membrane proteins, reconstitution of the artificial membrane environment is also essential in maintaining native protein configurations for biological functions [60]. Unfortunately, the detergents, which stabilise the membrane proteins, can easily disrupt the lipid bilayers (as described in Section 4) by penetrating the membranes and then form lipid micelles. Researchers are motivated to develop new approaches to encounter the technical difficulties in reconstituting the native environment for studying membrane proteins *in vitro* [61].

As with any structural or functional investigations with membrane proteins, the use of direct protein immobilisation on a solid support has been used intensively in the protein array and biosensors industry [62, 63]. Often the challenge for this method is that the immobilised proteins adapt into random orientations, causing a change in protein conformations and consequently reducing the bioactivity. Therefore, conformationally oriented immobilisation strategy should be considered to enhance the stability of the immobilised proteins. Site-directed mutagenesis, a protein-engineering method, is particularly useful to improve the quality of protein immobilisation on a solid support. The selected amino acid sequences of protein are precisely mutated and the modified amino acids are used for surface immobilisation [62, 63]. Two different approaches, cysteine and histidine residues mutations, have been developed as illustrated in **Figure 4** [63–66]. The designed mutations (either cysteine or histidine) allow the membrane proteins to immobilise with a particular orientation in which their native conformations and activities are retained upon adsorption [14, 27, 67, 68]. Successfully, control protein orientation on a modified surface is a key to investigate the interactions and stereochemistry of multi-protein system [67].
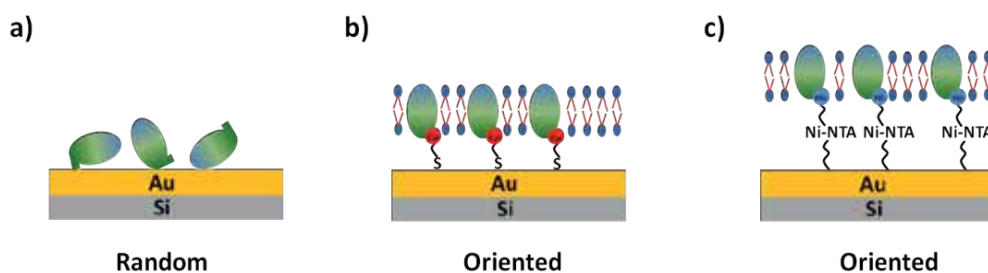
Figure 4. Protein immobilisation on gold (Au) or gold-modified surfaces: (a) direct immobilisation allows proteins oriented randomly, however, proteins orientation can be controlled by (b) thiol chemistry on cysteine residues (red) or (c) histidine (blue) interactions with nickel-nitrilotriacetic acid (Ni-NTA)-modified gold surfaces.

5.1. Substituted cysteine in protein forms a gold-thiolate covalent bond

The cysteine-containing proteins can be directly immobilised on gold surfaces using thiol chemistry [69], i.e., the sulphur atom on the cysteine residue forms a strong gold-thiolate covalent bond with the gold surfaces [12]. The spontaneous deposition promotes the formation of a dense self-assembled monolayer on gold. The application of cysteine-thiol immobilisation is commonly associated with biosensors and arrays applications. Brun et al. [12] used bacterial outer membrane proteins as a model for protein assay, which has potential applications as scaffolds for tissue engineering, proteomics and diagnostics. The outer membrane protein A (OmpA) is a monomeric membrane protein that involves in the survival mechanism in *Escherichia coli* (*E. coli*) when exposed to environmental stresses. The beta-barrel transmembrane structure of OmpA spans though the bacterial outer membranes and plays a vital role in membrane stability [70]. In Brun and co-workers' studies, OmpA was engineered by inserting a cysteine residue into the periplasmic turn, such that the OmpA was immobilised

on gold surfaces in a specific orientation via the covalent gold-thiolate bond. The immobilised OmpA was circularly permutated in order to expose the c and n termini for the interactions with *Staphylococcus aureus* protein A (SpA), a pathogen bound to bacterium cell wall. The SpA bound to OmpA using a mutated B domain (named as Z domain) created an OmpAZ protein scaffold on the gold surface [70]. Neutron reflectometry was used to detect the addition of Immunoglobulin G (IgG) on the OmpAZ protein scaffold, and the thickness of each protein layers was determined in high resolution. This provided information on the orientation of IgG on the OmpAZ protein scaffold [70]. Furthermore, Brun and co-workers enhanced the detection of IgG by introducing a flexible linker as a functional motif to link two Z domains together on OmpA (ZZOmpA). The capacity of IgG binding to ZZOmpA was greatly enhanced and hence potentially increased the signal and sensitivity for protein array applications [71, 72]. The antibody protein array (IgG-ZZOmpA) has been further used to detect antigen influenza nucleoprotein (NP), that is highly conserved and the basis of diagnostic tests for influenza. The NP binding capacity as well as the structural orientation of the bound antibody-antigen layer, ZZOmpA-NP layer, were fully characterised [65]. Brun et al. [65] have demonstrated the potential of using neutron reflectometry as an *in situ* physical characterisation of the protein assay assembly process. The cysteine-orientated immobilisation technique enables the proteins to be used to maintain in their native structure in order to be fully functional as a protein scaffold for further applications such as antibody and antigen detections.

5.2. Histidine-tagged membrane protein binds to nickel-nitrilotriacetic acid

Another protein immobilisation strategy is based on the covalent interactions between histidine (His) residues and nickel-nitrilotriacetic acid (Ni-NTA) modified surfaces. The His residues are genetically engineered on either the N or the C terminus of recombinant proteins [63]. The nickel-nitrilotriacetic acid (Ni-NTA) functionalised gold surface has a high affinity to capture His-tagged proteins, and hence all bound proteins are conferred in a particular orientation [67]. The His-Ni-NTA affinity technique enables the proteins immobilise on a solid surface without altering their function, which has been a challenge in the development of protein assay for decades [63, 67]. The use of recombinant affinity tags has addressed the issues of protein orientation and surface density upon immobilisation on solid surface [67, 73].

Shen et al. [63] have reconstituted an artificial environment for the translocation and assembly module (Tam) nanomachine that catalyses the insertion and assembly of nascent membrane proteins into the outer membranes of bacteria. The TAM nanomachine is composed of two proteins: a beta-barrel contained TamA locates at the outer bacterial membrane and a beta-helical TamB spans in the inner bacterial membrane. The two protein subunits, TamA and TamB, are linked together by a three polypeptide-transport-associated (POTRA) domains in TamA that is located in the periplasm region. The precise movement and activity of the TAM nanomachines were studied using neutron reflectometry to provide an accurate measurement on the molecular movement of the Tam protein complexes [63]. Firstly, a hexa-histidine tag was specifically engineered into an extracellular loop of TamA to immobilise onto the Ni-NTA functionalised gold surface, followed by the addition of lipids for membrane reconstitution. The thickness of the membrane embedded beta-barrel, the three POTRA domains as well as

the hexahistidine extramembrane layers were separately determined in the reconstituted membrane environment. The architecture of the TAM complex (TamA and TamB) was also studied using neutron reflectometry; no structural movement was obtained upon interactions of TamB to the POTRA domains of TamA [63]. This study focuses on the interactions between a substrate protein, Ag43, and the TAM complex on a supported membrane. The presence of Ag43 triggered the POTRA domain of TamA to alter its conformational changes, projected away from the membrane. The movement of TamA created spatial constraint on the outer membrane and influenced TamB deposition within the Tam complex. Monitoring the TAM complex assembly pathways using neutron reflectometry allows further understanding on the operations of diverse cellular processes for virulence of bacterial pathogens [63].

6. Concluding remarks

Understanding the protein-membrane interactions is critical to expanding the applications in drug delivery, biological engineering and, especially, biosensors and microarrays [4]. In this chapter, examples of protein adsorption on various artificial membrane models are reviewed and discussed. Along with the technical advances of neutron reflectometry, information on molecular binding and environment and orientation of the lipids and biomolecules is investigated in great detail. The use of various artificial membrane models offers a methodological design suited to study protein/peptide-membrane interactions in different biological systems. The phospholipid monolayer models are particularly useful for biological applications exploring the influence of fluidity or surface properties [74]. The phospholipid monolayer consists of one leaflet of lipid, which represents only a half bilayer. The structural simplicity and versatility allow for monitoring accurately the lipid packing density [74]. Traditionally, the phospholipid monolayer is deposited at an air/water interface using the Langmuir-Blodgett method; the surface coverage of lipid monolayer at air/water interface can be easily controlled, enabling examination of the influence of phospholipid membrane properties on protein- and peptide-membrane interactions [18]. Alternatively, lipid can be deposited and functionalised using a polymer or surfactant at a solid/liquid interface [17]. The increasing availability of different artificial membrane models extends and improves the ability to mimic the biological equivalent.

Protein adsorption studies on various fluid phospholipid bilayers have been developed: (a) single supported lipid bilayers, (b) tethered lipid bilayer membranes, (c) polymer-cushioned bilayer membranes and (d) floating supported bilayers [29]. The ease of preparation and high stability of the support lipid bilayer make it the most popular artificial membrane model [29]. Tethered lipid bilayer membranes are complex interfacial structures where the phospholipid bilayers are deposited on molecular anchors that are chemically linked between the membrane and the solid support [47]. These tethered lipid bilayer membranes provide a thicker intermediate water layer that mimics the natural cell–like environment for membrane-associated process [74]. Fluid lipid membranes can be deposited on a soft, polymeric layer, named polymer cushioned membranes [16]. The incorporation of molecular anchors and polymers between membranes and solid surface improves the long-term stability of the phospholipids

and provides a better biomimetic condition for the applications of membrane proteins [53]. Recently, floating supported bilayers are used as an advance membrane model to mimic the phase behaviour of lipids and the fluidity of bilayers in nature. The floating supported bilayers are created using a series of both Langmuir-Blodgett and Langmuir-Schaefer methods onto a solid support, and this is the most suitable system to replicate the asymmetry of bacterial outer membranes [55]. However, artificial membranes may not always be the most suitable system to investigate and examine the structural and functional aspects of membrane proteins because (a) lipid bilayers can be destroyed by the membrane protein solution that contains surfactant and (b) it is difficult to control the protein orientation on a solid support [60]. Thus, membrane proteins can be modified or mutated at desired locations to control the protein orientation when immobilised on gold-modified surfaces. Cysteine or histidine residues are the common approaches for the binding of protein onto thiol-modified or nickel-nitrilotriacetic acid-modified gold surfaces [63–66]. These conformationally oriented immobilisation strategies allow the membrane proteins to retain their native conformations and activities upon adsorption and also it creates a stable lipid layer surrounding the membrane protein. This review illustrates and highlights examples of the role of neutron reflectometry for studying proteins and peptides in biomimetic membranes. Many important advantages and unique features of neutron reflectometry offer numerous opportunities for innovative applications and technical development for *in vitro* study of biomolecules. Only a small number of neutron reflectometry applications in protein adsorption are demonstrated, the potential for studying protein-membrane interactions in multi-components should not be underestimated in the future [15].

Author details

Joyee Chun In Yeung[1], Tsung-Wu Lin[2] and Hsin-Hui Shen[1*]

*Address all correspondence to: hsin-hui.shen@monash.edu

1 Infection and Immunity Program, Biomedicine Discovery Institute and Department of Microbiology, Monash University, Melbourne, Australia

2 Department of Chemistry, Tunghai University, Taichung City, Taiwan

References

[1] Carpenter EP, Beis K, Cameron AD, Iwata S. Overcoming the challenges of membrane protein crystallography. Current Opinion in Structural Biology. 2008;18(5): 581-586.

[2] Tanaka M. Supported membranes – Structure and interactions. In: Comprehensive Biophysics: Elsevier. 2012. pp 261-272. ISBN:9780080957180

[3]   Yu Q, Chen H. Interaction of switchable biomaterials surfaces with proteins. In: Switchable and Responsive Surfaces and Materials for Biomedical Applications. Woodhead Publishing, 2015.

[4]   Lu JR. Neutron reflection. In: Surfaces and Interfaces for Biomaterials. Woodhead Publishing, 2005.

[5]   Sackmann E. Supported membranes: Scientific and practical applications. Science. 1996;271(5245):43-48.

[6]   Torikai N, Yamada NL, Noro A, Harada M, Kawaguchi D, Takano A, et al. Neutron reflectometry on interfacial structures of the thin films of polymer and lipid. Polymer Journal. 2007;39(12):1238-1246.

[7]   Krueger S. Neutron reflection from interfaces with biological and biomimetic materials. Current Opinion in Colloid & Interface Science. 2001;6:111-117.

[8]   Thomas RK. Neutron reflection from liquid interfaces. Annual Review of Physical Chemistry. 2004;55:391-426. DOI:10.1146/annurev.physchem.54.011002.103830

[9]   Agency IAE, editor. Neutron reflectometry: A probe for materials surfaces. Proceedings of a Technical Meeting. International Atomic Energy Agency. Vienna: International Atomic Energy Agency, 2004.

[10]   Schreyer A, Majkrzak CF, Berk NF, Grüll H, Han CC. Using polarized neutrons to determine the phase of reflection from thin film structures. Journal of Physics and Chemistry of Solids. 1999;60(8-9):1045-1051. DOI:http://dx.doi.org/10.1016/S0022-3697(99)00045-1

[11]   Holt SA, Le Brun AP, Majkrzak CF, McGillivray DJ, Heinrich F, Losche M, et al. An ion-channel-containing model membrane: Structural determination by magnetic contrast neutron reflectometry. Soft Matter. 2009;5(13):2576-2586. DOI:10.1039/B822411K

[12]   Brun APL, Holt SA, Shah DS, Majkrzak CF, Lakey JH. Monitoring the assembly of antibody-binding membrane protein arrays using polarised neutron reflection. European Biophysics Journal. 2008;37:639-645. DOI:10.1007/s00249-008-0291-2

[13]   Heinrich F. Deuteration in Biological Neutron Reflectometry. In: Methods in Enzymology. Elsevier. 2016. pp. 211-230. DOI:10.1016/bs.mie.2015.05.019

[14]   Krueger S, Meuse CW, Majkrzak CF, Dura JA, Berk NF, Tarek M, et al. Investigation of hybrid bilayer membranes with neutron reflectometry: Probing the interactions of Melittin. Langmuir. 2001;17:511-521. DOI:10.1021/la001134t

[15]   Jackman JA, Knoll W, Cho NJ. Biotechnology applications of tethered lipid bilayer membranes. Materials. 2012;5:2637-2657. DOI:doi:10.3390/ma5122637

[16]   McCabe IP, Forstner MB. Polymer supported lipid bilayers. Open Journal of Biophysics. 2013;3:59-69. DOI:10.4236/ojbiphy.2013.31A008

[17] Li JB, He Q, Yan Xh. Biomimetic Membranes. In: *Molecular Assembly of Biomimetic Systems*. Wiley, 2011; pp. 7-39. ISBN:978-3-527-32542-9

[18] Pirrone GF, Vernon BC, Michael S. Kent, Engen JR. Hydrogen exchange mass spectrometry of proteins at Langmuir monolayers. Analytical Chemistry. 2015;87:7022-7029. DOI:10.1021/acs.analchem.5b01724

[19] Pichot R, Watson RL, Norton IT. Phospholipids at the interface: Current trends and challenges. International Journal of Molecular Sciences. 2013;14:11767-11794. DOI: 10.3390/ijms140611767

[20] Maierhofer AP, Bucknall DG, Bayerl TM. Modulation of cytochrome c coupling to anionic lipid monolayers by a change of the phase state: A combined neutron and infrared reflection study. Biophysical Journal. 2000;79:1428-1437. DOI:10.1016/S0006-3495(00)76394-6

[21] Miano F, Zhao X, Lu JR, Penfold J. Coadsorption of human milk lactoferrin into the dipalmitoylglycerolphosphatidylcholine phospholipid monolayer spread at the air/water interface. Biophysical Journal. 2007;92:1254-1262. DOI:10.1529/biophysj.105.078592

[22] Pirrone GF, Emert-Sedlak LA, Wales TE, Smithgall TE, Kent MS, Engen JR. Membrane-associated conformation of HIV-1 Nef investigated with hydrogen exchange mass spectrometry at a Langmuir monolayer. Analytical Chemistry. 2015;87:7030-7035. DOI:10.1021/acs.analchem.5b01725

[23] Kuhl TL, Majewski J, Wong JY, Steinberg S, Leckband DE, Israelachvili JN, et al. A neutron reflectivity study of polymer-modified phospholipid monolayers at the solid-solution interface: Polyethylene glycol-lipids on silane-modified substrates. Biophysical Journal. 1998;75:2352-2362. DOI:10.1016/S0006-3495(98)77679-9

[24] Hollinshead CM, Hanna M, Barlow DJ, Biasi VD, Bucknall DG, Camilleri P, et al. Neutron reflection from a dimyristoylphosphatidylcholine monolayer adsorbed on a hydrophobised silicon support. Biochimica et Biophysica Acta. 2001;1511:49-59. DOI: 10.1016/S0005-2736(00)00380-1

[25] Penfold J, Richardson RM, Zarbakhsh A, Webster JRP, Bucknall DG, Rennie AR, et al. Recent advances in the study of chemical surfaces and interfaces by specular neutron reflection. Journal of the Chemical Society, Faraday Transactions. 1997;93(22):3899-3917. DOI:10.1039/A702836I

[26] Lu JR, Murphy EF, Su TJ. Reduced protein adsorption on the surface of a chemically grafted phospholipid monolayer. Langmuir. 2001;17:3382-3389. DOI:10.1021/la0017429

[27] Lu JR, Zhao X, Yaseen M. Protein adsorption studied by neutron reflection. Current Opinion in Colloid & Interface Science. 2007;12:9-16. DOI:10.1016/j.cocis.2007.02.001

[28] Schmidt A, Spinke J, Bayerl T, Sackmann E, Knoll W. Streptavidin binding to biotiny-lated lipid layers on solid supports. A neutron reflection and surface plasmon optical study. Biophysical Journal. 1992;63:1185-1192. DOI:10.1016/S0006-3495(92)81715-0

[29] Wacklin HP. Neutron reflection from supported lipid membranes. Current Opinion in Colloid & Interface Science. 2010;15:445-454. DOI:10.1016/j.cocis.2010.05.008

[30] Choi D, Moon JH, Kim H, Sung BJ, Kim MW, Tae GY, et al. Insertion mechanism of cell-penetrating peptides into supported phospholipid membranes revealed by X-ray and neutron reflection. Soft Matter. 2012;8:8294-8297. DOI:10.1039/C2SM25913C

[31] Cho NJ, Frank CW, Kasemo B, Höök F. Quartz crystal microbalance with dissipation monitoring of supported lipid bilayers on various substrates. Nature Protocols. 2010;5:1096-1106. DOI:10.1038/nprot.2010.65

[32] Richter RP, Lai KHJ, Brisson AR. Supported lipid membranes. Materialstoday. 2003;November:32-37. DOI:10.1016/S1369-7021(03)01129-5

[33] Brun APL, Haigh CL, Drew SC, James M, Boland MP, Collins SJ. Neutron reflectometry studies define prion protein N-terminal peptide membrane binding. Biophysical Journal. 2014;107:2312-2324. DOI:10.1016/j.bpj.2014.09.027

[34] Hellstrand E, Grey M, Ainalem M-L, Ankner J, Forsyth VT, Fragneto G, et al. Adsorption of α-synuclein to supported lipid bilayers: Positioning and role of electrostatics. ACS Chemical Neuroscience. 2013;4:1339-1351. DOI:10.1021/cn400066t

[35] Lu J, Brun APL, Chow SH, Shiota T, Wang B, Lin TW, et al. Defining the structural characteristics of annexin V binding to a mimetic apoptotic membrane. European Biophysics Journal. 2015;44:697-708. DOI:10.1007/s00249-015-1068-z

[36] Fernandez DI, Brun APL, Lee T-H, Bansal P, Aguilar M-I, James M, et al. Structural effects of the antimicrobial peptide maculatin 1.1 on supported lipid bilayers. European Biophysics Journal. 2013;42:47-59. DOI:10.1007/s00249-012-0796-6

[37] Tiberg F, Harwigsson I, Malmsten M. Formation of model lipid bilayers at the silica-water interface by co-adsorption with non-ionic dodecyl maltoside surfactant. European Biophysics Journal. 2000;29:196-203. DOI:0.1016/j.bbamem.2004.11.001

[38] Vacklin HP, Tiberg F, Fragneto G, Thomas TK. Composition of supported model membranes determined by neutron reflection. Langmuir. 2005;21(7):2827-2837.

[39] Stillwell W. *Membrane Polar Lipids*. Elsevier B.V. 2013. ISBN:978-0-444-52153-8

[40] Hamai CK, Higuchi M, Iwai H, Miyahara Y. Detergent-mediated formation of polymer-supported phospholipid bilayers. Langmuir. 2010;26(18):14600-14605. DOI:10.1021/la102151p

[41] Talbot JP, Barlow DJ, Lawrence MJ, Timmins PA, Fragneto G. Interaction of cationic lipoplexes with floating bilayers at the solid-liquid interface. Langmuir. 2009;25:4168-4180. DOI:10.1021/la802844f

[42] Vacklin HP, Tiberg F, Fragneto G, Thomas RK. Phospholipase A_2 hydrolysis of supported phospholipid bilayers: A neutron reflectivity and ellipsometry study. Biochemistry. 2005;44:2811-2821. DOI:10.1021/la047389e

[43] Shen H-H, Thomas RK, Penfold J, Fragneto G. Destruction and solubilization of supported phospholipid bilayers on silica by the biosurfactant surfactin. Langmuir. 2010;26(10):7334-7342. DOI:10.1021/la904212x

[44] Corkery RW. Langmuir–Blodgett (L–B) multilayer films. Langmuir. 1997;13(14): 3591-3594. DOI:10.1021/la9701743

[45] Girard-Egrot AP, Blum LJ. Langmuir-Blodgett technique for synthesis of biomimetic lipid membranes. In: Nanobiotechnology of Biomimetic Membranes. Fundamental Biomedical Technologies. 2007, pp. 23-74.

[46] Clifton LA, Skoda MWA, Daulton EL, Hughes AV, Brun APL, Lakey JH, et al. Asymmetric phospholipid: Lipopolysaccharide bilayers: A Gram-negative bacterial outer membrane mimic. Journal of Royal Society Interface. 2013;10(89). DOI:10.1098/rsif. 2013.0810

[47] Love JC, Estroff LA, Kriebel JK, Nuzzo RG, Whitesides GM. Self-assembled monolayers of thiolates on metals as a form of nanotechnology. Chemical Reviews. 2005;105:1103-1169. DOI:10.1021/cr0300789

[48] Knobler CM, Schwartz DK. Langmuir and self-assembled monolayers. Current Opinion in Colloid & Interface Science. 1999;4(1):46-51. DOI:10.1016/ S1359-0294(99)00002-3

[49] Junghans A, Koper I. Structural analysis of tethered bilayer lipid membranes. Langmuir. 2010;26(13):11035-11040. DOI:10.1021/la100342k

[50] Yap TL, Jiang Z, Heinrich F, Gruschus JM, Pfefferkorn CM, Barros M, et al. Structural features of membrane-bound glucocerebrosidase and α-synuclein probed by neutron reflectometry and fluorescence spectroscopy. Journal of Biological Chemistry. 2015;290(2):744-754. DOI:10.1074/jbc.M114.610584

[51] Douglas MR, Lewthwaite AJ, Nicholl DJ. Genetics of Parkinson's disease and parkinsonism. Expert Review of Neurotherapeutics. 2007;7(6):657-666. DOI: 10.1586/14737175.7.6.657

[52] Hertrich S, Stetter F, Rühm A, Hugel T, Nickel B. Highly hydrated deformable polyethylene glycol-tethered lipid bilayers. Langmuir. 2014;30:9442-9447. DOI:10.1021/ la4045804

[53] Dante S, Hau T, Steitz R, Canale C, Dencher NA. Nanoscale structural and mechanical effects of beta-amyloid (1–42) on polymer cushioned membranes: A combined study by neutron reflectometry and AFM force spectroscopy. Biochimica et Biophysica Acta. 2011;1808:1646-1655. DOI:10.1016/j.bbamem.2011.07.024.

[54] Murphy MP, III HL. Alzheimer's disease and the β-amyloid peptide. Journal of Alzheimer's Disease. 2010;19(1). DOI:10.3233/JAD-2010-1221.

[55] Fragneto G, Charitat T, Graner F, Mecke K, Perino-Gallice L, Bellet-Amalric E. A fluid floating bilayer. Europhysics Letters. 2001;53(1):100-106. DOI:10.1209/epl/i2001-00129-8

[56] Clifton LA, Holt SA, Hughes AV, Daulton EL, Arunmanee W, Heinrich F, et al. An accurate in vitro model of the E. coli envelope. Angewandte Communications. 2015;54:11952-11955. DOI:10.1002/anie.201504287

[57] Hughes AV, Holt SA, Daulton E, Soliakov A, Charlton TR, Roser SJ, et al. High coverage fluid-phase floating lipid bilayers supported by v-thiolipid self-assembled monolayers. Journal of Royal Society Interface. 2014;11. DOI:10.1098/rsif.2014.0447

[58] Hughes AV, Howse JR, Dabkowska A, Jones RAL, Lawrence MJ, Roser SJ. Floating lipid bilayers deposited on chemically gradted phosphatidycholine surfaces. Langmuir. 2008;24(5):1989-1999. DOI:10.1021/la702050b

[59] Seddon AM, Curnow P, Booth PJ. Membrane proteins, lipids and detergents: not just a soap opera. Biochimica et Biophysica Acta: Biomembranes. 2004;1666(1-2):105-117. DOI:10.1016/j.bbamem.2004.04.011

[60] Wiśniewska-Becker A, Gruszecki W. Biomembrane models. In: Drug-Biomembrane Interaction Studies-The Application of Calorimetric Techniques. Woodhead. 2013. pp 47-95. ISBN:9781907568053

[61] Maire Ml, Champeil P, MÖller JV. Interaction of membrane proteins and lipids with solubilizing detergents. Biochimica et Biophysica Acta. 2000;1508:86-111

[62] Kim D, Herr AE. Protein immobilization techniques for microfluidic assays. Biomicrofluidics. 2013;7(4). DOI:10.1063/1.4816934

[63] Shen H-H, Leyton DL, Shiota T, Belousoff MJ, Noinaj N, Lu J, et al. Reconstitution of a nanomachine driving the assembly of proteins into bacterial outer membranes. Nature Communications. 2014;5. DOI:10.1038/ncomms6078

[64] Rudra JS, Collier JH. Self-Assembling Biomaterials. In: Comprehensive Biomaterials. Elsevier, 2011. pp. 77-94. ISBN:9780080552941

[65] Brun APL, Soliakov A, Shah DSH, Holt SA, McGill A, Lakey JH. Engineered self-assembling monolayers for label free detection of influenza nucleoprotein. Biomedical Microdevices. 2015;17(3). DOI:10.1007/s10544-015-9951-z

[66] Turkova J. Oriented immobilization of biologically active proteins as a tool for revealing protein interactions and function. Journal of Chromatography B. 1999;722:11-31. DOI:10.1016/S0378-4347(98)00434-4

[67] Ley C, Holtmann D, Mangold K-M, Schrader J. Immobilization of histidine-tagged proteins on electrodes. Colloids and Surfaces B: Biointerfaces. 2011;88:539-551. DOI: 10.1016/j.colsurfb.2011.07.044

[68] Unsworth LD, Tun Z, Sheardown H, Brash JL. In situ neutron reflectometry investigation of gold-chemisorbed PEO layers of varying chain density: Relationship of layer structure to protein resistance. Journal of Colloid and Interface Science. 2006;296(2):520-526. DOI:10.1016/j.jcis.2005.09.056

[69] Tao F, Bernasek SL. Self-assembled monolayers. In: *Comprehensive Nanoscience and Technology*. Elsevier, 2011. pp. 127-152. ISBN:978-0-12-374390-9

[70] Wang Y. The function of OmpA in Escherichia coli. Biochemical and Biophysical Research Communications. 2002;292(2):396-401. DOI:10.1006/bbrc.2002.6657

[71] Brun APL, Shah DSH, Athey D, Holt SA, Lakey JH. Self-assembly of protein monolayers engineered for improved monoclonal immunoglobulin G binding. International Journal of Molecular Science. 2011;12:5157-5167. DOI:10.3390/ijms12085157

[72] Brun APL, Holt SA, Shah DSH, Majkrzak CF, Lakey JH. The structure orientation of antibody layers bound to engineered biosensor surfaces. Biomaterials. 2011;32:3303-3311. DOI:10.1016/j.biomaterials.2011.01.026

[73] Oshige M, Yumoto K, Miyata H, Takahashi S, Nakada M, Ito K, et al. Immobilization of His-tagged proteins on various solid surfaces using NTA-modified chitosan. Open Journal of Polymer Chemistry. 2013;3:6-10. DOI:10.4236/ojpchem.2013.31002

[74] Czolkos I, Jesorka A, Orwar O. Molecular phospholipid films on solid supports. Soft Matter. 2011;7:4562-4576. DOI:10.1039/C0SM01212B

Edited by Waldemar Alfredo Monteiro

This book brings suitable data concerning theory and experiments of neutron interactions with different materials. Since the neutron discovery by Chadwick in 1932, researchers of the entire world begin to make studies about it. It is well known that neutron have no charge, and their electric dipole moment is either zero or too small to measure, but theories and experiments show that neutron has spin (presence of magnetic moment), and polarization neutron scattering is plausible. The reader can obtain remarks about inelastic scattering cross sections for neutron; polarized neutron reflectivity; scattering methods; neutron reflectometry tool to probe the chemical structures; neutron scattering for amino acid crystals; and small-angle neutron scattering nanoemulsion heat transfer fluids in this book.

IntechOpen